Title	Advanced One-Step Solution Approach for Molybdenum Oxide Nanostructure Synthesis and Electrical Device Fabrication
Author(s)	Cong, Shuren
Citation	大阪大学, 2017, 博士論文
Version Type	VoR
URL	https://doi.org/10.18910/61770
rights	
Note	

Doctoral Dissertation

Advanced One-Step Solution Approach for Molybdenum Oxide Nanostructure Synthesis and Electrical Device Fabrication

Shuren Cong

December 2016

Department of Adaptive Machine Systems

Graduate School of Engineering,

Osaka University

Ph. D. Dissertation

Advanced One-Step Solution Approach for Molybdenum Oxide Nanostructure Synthesis and Device Fabrication

Shuren Cong

Department of Adaptive Machine Systems
Graduate School of Engineering
Osaka University

December 2016

Approved by

Professor Katsuaki Suganuma

Professor Sekino Tohru

Associate Professor Shijo Nagao

Abstract

As one of the most promising candidates for next generation electronic sensor material, molybdenum oxide, are attracting more and more attentions because of its special crystal and electronic structure. The thermodynamically orthorhombic phase α-MoO_3 employs an unique layer structure in the [010] direction, which will result in anisotropic growth at certain growth condition to form the low-dimension nanostructures with large specific surface area. Nanomorphologies can provide plentifully interfacial action states for the chemical reaction between the gas/liquid and molybdenum oxide, which are very promising for fabricating the gas sensors. Furthermore, the work function and conductivity of the molybdenum oxide (MoO_x) can be artificially modified through tuning the composition of oxygen in the oxide because the Mo cation can exhibit polyvalence in the oxide. The band engineering of the MoO_x makes it show great potential as the hole transport layer (HTL) in the organic solar cells, which requires the well-aligned energy level of HTL with the highest occupied molecular orbital (HOMO) of the organic active layer.

My achievements are listed as follows:

(1) I firstly successfully fabricated the α-MoO_3 single crystal nanorod arrays in random direction on the substrate through a simple and short time solution annealing process. The nanorod arrays were characterized as ultrafine (about 10 nm) and single α-phase. The length, number, coverage area the nanorods can be effectively controlled by optimizing the synthesis parameters, such as molar ratio of the starting material, solvents in the precursors, annealing temperature and time. A possible mechanism was presented to explain the growth process.

(2) The prepared α-MoO_3 nanorod arrays were firstly found very sensitive to the VOCs even with trace concentrations. Gas sensors based on the α-MoO_3 nanorod arrays showed the prompt response and obvious discrimination to ethanol, methanol, isopropanol, and acetone vapors at 300 ^{o}C via the modulation of the resistance of the gas sensors. The sensitivity, response time, and recovery time of the sensors strongly depend on the specific morphologies of the α-MoO_3 nanorods, such as length, number, and coverage of the nanorods. The reaction mechanism indicates that the nanorods are more readily to adsorb and react with the target molecules than the bulk MoO_3.

(3) The simple and short-time solution annealing process was modified to form HTLs for organic solar cells by adding hydrogen peroxide and adjusting the molar ratio of the starting materials in the precursors and annealing temperature. The MoO_x thin layer showed the high conductivity and high work function. The organic solar cell based on the solution processed MoO_3 HTLs achieved the comparative high performance with the reference device made from the evaporated molybdenum oxide or the PEDOT:PSS HTLs.

In conclusion, this research provides a simple and new solution annealing process for the synthesis of the nano-scale functional materials with controllable morphology by optimizing the chemical parameters and annealing conditions. The method can be extended to fabricate other similar nano-materials with fast, large-scale and low-cost process. Moreover, the fabricated molybdenum oxide can be applied as gas sensor, solar cell, which widely enlarged the application of indirect wide band-gap semiconductor material in various electronic devices.

Table of Contents

Chapter 1

Introduction

Abstract

Molybdenum oxide possesses the polyvalence and polymorphs properties, which make it a candidate for various devices. Scientist focus of their interests on fabricating molybdenum oxide based devices with a low-cost solution process. In order to develop the simple solution process to fabricate α-MoO_3 nanorod arrays, the reported crystal structures, nanostructures, synthesis methods of MoO_3 were studied. In order to fabricate a gas sensor based on α-MoO_3 nanorod arrays, the reported manufacturing method, gas sensing properties and reaction mechanisms to VOCs of MoO_3 were investigated. In order to fabricate a MoO_x based hole transport layer (HTL) with a simple solution process for organic solar cells, the traditional HTL materials, electronic properties, working mechanism of MoO_3 HTL were investigated. Based on aforementioned research the objectives of this work were presented.

1.1 Crystal structures and physical chemical properties of molybdenum oxide

Transition metal oxides with diverse crystal structures and superior functional properties have been the focus of much attention in recent years by virtue of their scientific and technological applications [1-3]. Molybdenum oxide, as one of the most important transition metal oxides, has found its applications in various filed, such as chromogenic/electrochromic display devices [4, 5], display devices [6, 7], smart window technology [8, 9], sensors, and lithium ion battery electrodes [10-12].

1.1.1 Crystal structures of molybdenum oxide

Molybdenum (Mo) is a group VI transition metal lying below chromium and above tungsten in the periodic table with 6 outermost electrons. Mo can exhibit diversity of oxidation state (from 0 to +6), and coordination numbers (from 4 to 6) in oxide. MoO_3 is mostly concerned within these oxidation states due to its extremely interesting structural, chemical, electrical, and optical properties.

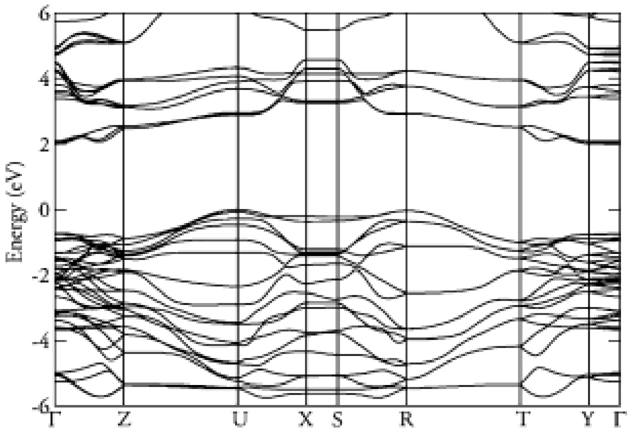

Figure 1.1 Electronic band structure along the high-symmetry points for MoO_3, the highest occupied state is set to 0 eV [14].

MoO_3 is a distinct insoluble (water) yellow powder, with a density of 4.7 g/cm^3 at room temperature. Typically, MoO_3 is n-type semiconductor, since the oxygen is readily to be lost in MoO_3. As a d^0 semiconductor, MoO_3 behaves indirect wide band gap of 3.1-3.8 eV and high work function of 6.8-6.9 eV [13]. The band structure of MoO_3 was shown in the Figure 1.1.

Pure MoO_3 has three polymorphs with different physical and chemical properties. The orthorhombic phase (α-MoO_3, space group Pbnm (No.62), unit cell parameters: a=3.9620 Å, b =13.86 Å, and c = 3.70 Å, JCPD file: 05-0508) [14] is thermodynamically stable phase, whose crystal structure is shown in Figure 1.2. α-MoO_3 consists of a series of special double-layers that are oriented perpendicular to the [010] direction [14-17]. In each double-layer, MoO_6 octahedra form edge-sharing zig-zag rows along the [001] direction and corner sharing rows along the [100] direction. Each double-layer consists of two sublayers of distorted MoO_6 octahedra to give three crystallographically inequivalent oxygen sites and interacts with the adjacent bilayer in the [010] direction through a weak van der Waals interaction. The internal interactions between atoms within the double-layers are dominated by strong ionic and covalent bonding. The stratified structure facilitates the injection of different donor ions into the free spaces of the bilayers, and thus creating its favorable electrical properties [18-21]. Moreover, the nature of the Mo–O bond changes considerably with the equilibrium bond distance, and varies from strongly covalent for the shortest bond to predominantly ionic for the longest bonds in the MoO_6 octahedron [14, 22]. The special layer structure of MoO_3 show great potential for the growth of anisotropic crystal with large specific surface area. Nanostructures of MoO_3, such as nanosphares, nanorods, nanotubes, nanoplates, and nano composite materials, have become to be the scientists' interests for their special chemical and physical properties [23-26].

The monoclinic phase (β-MoO_3, space group $P2_1/c$ (No. 14), unit cell parameters: a=7.1228 Å, b=5.3660 Å, c=5.5665 Å, β=92.01°, JCPD file: 047-1081) [27], whose crystal structure is shown in Figure 1.2. The first β-MoO_3 was synthesized by gently heating spray-dried molybdic acid, which had been produced by passing sodium. The structure of β-MoO_3 was closely related to that of a monoclinic form of WO_3, with Mo atoms octahedrally coordinated to oxygen and all octahedra corner-linked to form an open framework [28]. The β-phase is metastable monoclinic and can be converted to the thermodynamically stable α-phase at about 400 – 500 °C.

A very salient structural feature for h-MoO_3 is the presence of a tunnel (~ 3.0 Å in diameter) running along the c direction probably with some cations or water molecules inside, which is enclosed by twelve MoO_6 octahedra linked by sharing corners along the a and b directions as well as edges along the c direction. Most reported h-MoO_3 takes the structure described in JCPDS 21-0569 (primitive: P or space group: $P6_3/m$ (No. 176), unit cell parameters: a=10.53 Å and c=14.87 Å) [29]. Although reference [27], [29] indicate β-phase and h-phase also show good catalyst properties, the instabilities of the β-, h- MoO_3 restricted their applications.

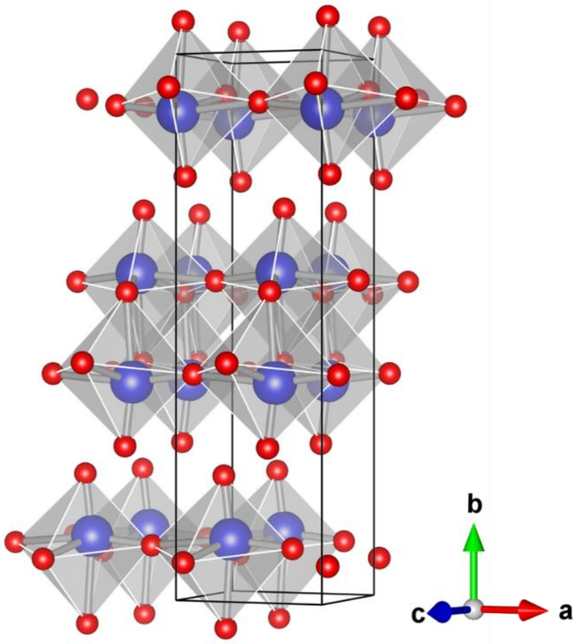

Figure 1. 2 Crystal structure of α-MoO_3 with orthorhombic phase.

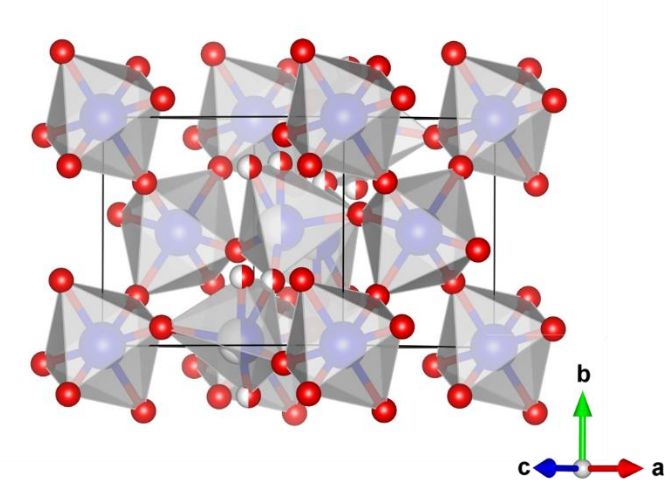

Figure 1. 3 Crystal structure of β-MoO_3 with monoclinic phase.

1.1.2 Chemical and physical properties of molybdenum oxide

MoO_3 can be easily reduced to the lower oxidation state. For instance, it can be reduced to another metastable binary oxide, namely, MoO_2. crystal of MoO_2 employs a monoclinic structure (space group $P2_1/c$) with unit cell parameter of a=5.6109 Å, b=4.8562 Å, and c=5.6285 Å and a monoclinic angle of 120.95^o (JCPDS file: 78-1069), just like the rutile, but the unit cell contains four MoO_2 [30, 31] Below oxygen to metal ratios of 2.90, seven stable and/or metastable sub-oxides have been identified between the compositions of MoO_3 and MoO_2: $Mo_{18}O_{52}$, Mo_9O_{26}, Mo_8O_{23}, Mo_5O_{14}, $Mo_{17}O_{47}$, η-Mo_4O_{11} and γ-Mo_4O_{11} [29, 32-34]. The plenty of valence states of Mo in oxide indicates that the physical properties, i.e. Femi energy, density of states and band gap, of Mo based oxide can be artificially controlled from insulator to metal by tailoring the composition of O atom in the oxide [35, 36].

The polyvalence properties of the Mo and interesting polymorphs of the Mo based oxide make the Mo based oxide show great potential in various devices. For example, nanostructure of MoO_3 is used as a cathode material in the development of high-energy density solid-state micro-batteries. It is reported, when the double layer of MoO_3 are intercalated by electron-donating cations, it becomes good conductors, which, therefore, makes them are ideal as the electrodes for electrochemical cells [20, 32].

MoO_3 is readily to be reduced to the lower oxidation state which is the critical properties for the gas sensors materials [20, 26]. When being exposed to the target gas, MoO_3 is considered as the catalytic for the oxidation of gas on the oxide surface. MoO_3 leaves the oxygen vacancies at the surface of it, which result in the resistance change at the surface of MoO_3 [25, 37, 38].

As nonstoichiometric form of MoO_3, MoO_{3-x} films exhibit the well aligned energy level with the active organic material and metal electrodes, which make it suitable for fabricating the hole transport layer of the organic solar cells. The electrical properties of MoO_{3-x} films can be artificially tuned by the oxygen vacancies as high work function and low series resistance in organic solar cells [36, 39].

1.2 Synthesis process of molybdenum oxides nanostructure

Nanotechnology is expected to have an impact on all industries including semiconductors and biotechnology, which provide the motivation to further insight into nanoscale phenomena and novel structures [40-42]. In recent decades, development of nanoscale materials with different morphologies have become a key area in basic scientific researches due to their unique properties compared with respective bulk materials [43-45]. However, developing simple and economic methods for preparing novel functional nano-structures is still a major challenge in the nanoscience and nanotechnology field.

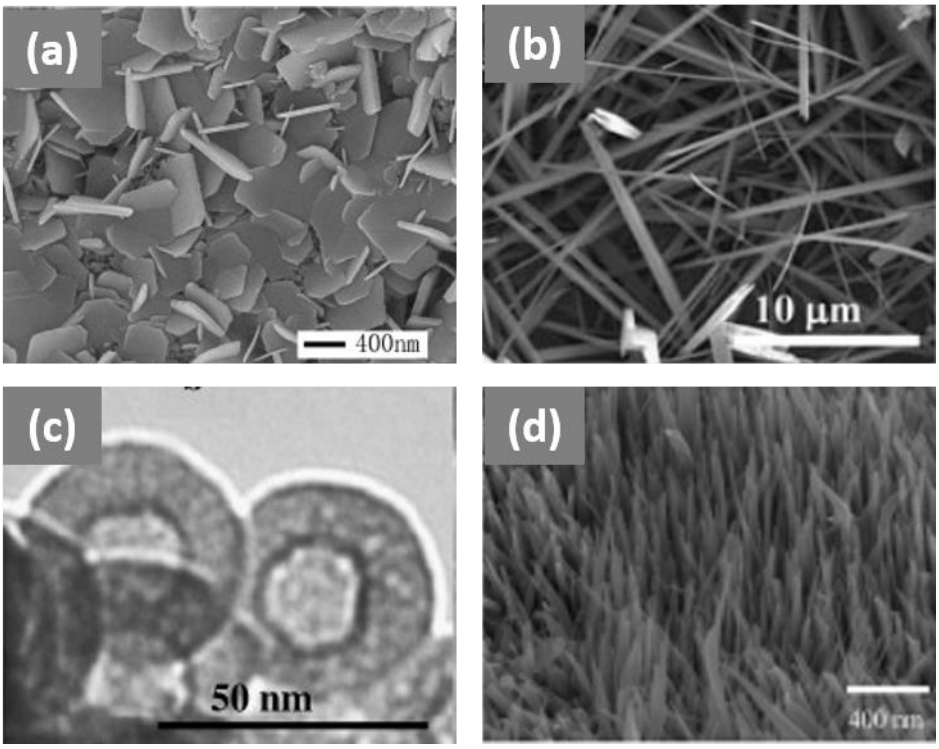

Figure 1. 4 As reported typical nanostructures of MoO_3, (a) nanoplates [46] (b) nanosheets [15] (c) nanospheres [47] (d) nanowire arrays [48].

Until now, many methods have been proposed to prepare MoO_3 and its derivatives. Nanostructural MoO_3 have been successfully synthesized by a variety of physical or/and chemical manufacturing methods for the purpose of reducing the size of the particles or increasing the surface area for different applications. Balendhran et al. [16] have classified these methods into three major categories: vapor (chemical vapor deposition (CVD) et al.), liquid (sol-gel process, hydrothermal process et al.) and solid phase deposition techniques (electrodeposited, thermal evaporation, R.F. sputtering method et al.). Here, the typical nanostructures and synthesis methods of MoO_3 were reviewed.

A variety of nanostructures of α-MoO_3 have been reported for their special morphologies, as shown in Figure 1.4. Nanoplates, nanosheet, nanosphares, hollow nanospheres, and single-walled α-MoO_3 nanotubes morphologies were synthesized with a diameter from n × 10^0 nm to n × 10^2 nm, solution/evoration process [15, 46, 47, 49, 50].

Recently, considerable efforts are paid to synthesize the nanorod structures of α-MoO_3 to achieve the much higher specific surface area, so as to achieve the promising performance of the devices. Qian et al. synthesized the hexagonal MoO_3 nanorods with a diameter of the 40 nm using the hydrothermal method, which showed the higher performance for the lithium-ion batteries than the microrods with diameters of 2-3 μm [51]. Lou et al, developed a faster (about 2 h) synthesis process [52] to grow α-MoO_3 nanorods with a width of about 100 nm by using the hydrothermal methods, which is 20 times faster than their former reported work [53]. They achieved the discharge capacity of 300 mAhg-1from their α-MoO_3 nanorods. Xue et al. synthesized the core-shell α-Fe_2O_3@α-MoO_3 Nanorods composites by using a two-step hydrothermal method to synthesize MoO_3 nanorods, which showed reversible capacity of 1481 $mAhg^{-1}$ [54]. Xue et al. also prepared the SnO_2/α-MoO_3 heterostructure-nanobelts by hydrothermal method, which show the 67.76 sensitivity to 500 ppm ethanol at 300 ^{o}C [55]. α-MoO_3 nanorods were also synthesized by using CVD [56], and evaporation method [57].

Most recently, MoO_3 based nanorod/nanowire arrays have been attracting great interests due to their well-aligned growth directions, easily being permeated into their inner by the adsorbate. Mo oxide-based naorod/wire arrays were generally fabricated through the evaporation [6, 58], or the two steps methods: sputtering the seed layer onto the substrate then using the hydrothermal methods to grow the longer nanorod arrays [48]. These MoO_3 based nanorod/nanowire arrays have shown great potential in emission, lithium ion batteries applications for their distinct electronic property and catalytic reaction abilities of solid/liquid interfaces [6, 48, 58]. However, the catalytic reaction abilities of solid/gas interfaces of MoO_3 nanorod/nanowire arrays, i.e. gas sensor application, are rarely researched. The traditional synthesis process of MoO_3 nanorod/nanowire arrays employed either complicated vacuum or two-step high pressure process, which severely restricted application or deeper research in gas sensor

[6, 48, 58]. To contrast, solution processes are very desirable for synthesizing thin films or nanoparticles. However, to now the solution process for synthesizing MoO_3 nanorod/nanowire arrays has been rarely reported. In this work, thus the challenge was made for the solution process to synthesize MoO_3 nanorod/nanowire arrays of controlled morphology and to investigate their gas sensing properties.

1.3 Gas sensing properties of nanostructured molybdenum oxides

1.3.1 Fundamentals of metal oxide gas sensor

The research of sensors has permeated by many professional science and engineering organizations. Sensor science generates thousands of new publications each year [59]. A gas sensor is a device that transforms target gas information, ranging from the concentration of a specific sample component to total composition analysis, into an analytically useful signal. Most of the metal oxide gas sensors are resistance control type. The surface state of the metal oxide are very sensitive to special gas substance. The change of the surface state cause the variation of the resistance of the gas sensors, from which the type and concentration of the target gas can be obtained [60-62].

Since the first gas sensing properties were reported in the 1950's, various semiconducting metal oxides were developed as industrial process control or security devices for monitoring of explosive or toxic gases [38, 63]. The electronic transport properties of metal oxides in the gas sensing devices strongly depend on the chemistry property of the gases and the presence/absence of defects on the surface of the metal oxide. The exact fundamental mechanisms that cause a gas response are still controversial, but essentially trapping of electrons at adsorbed molecules and band bending induced by these charged molecules are responsible for a change in conductivity [64-66]. Here, the basic working principles of solid-gas interactions of the oxide and the gases were concluded.

Generally, there are three possible solid-gas interaction mechanisms between a solid surface and gas molecules [37].

(1) Physical adsorption (physisorption), which relies on weak, long-range van der Waals dipole/dipole interactions as illustrated in Figure 1.5(a). Physisorbed molecules are never dissociated and the physisorption enthalpy is typically about 0.2 eV/molecule.

(2) Chemical adsorption (chemisorption), which is the formation of chemical bonds between gas molecules and solid surfaces, being accompanied with charges transfer as illustrated in Figure 1.5(b). Usually, the dissociated and chemisorption enthalpy of chemisorbed gas molecules are larger than in physisorption with the values of about 2 eV/molecule.

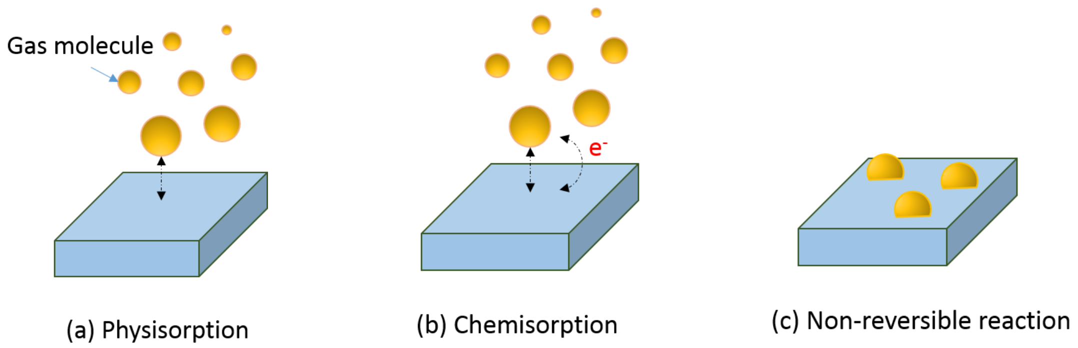

(a) Physisorption (b) Chemisorption (c) Non-reversible reaction

Figure 1.5 Interactions between solids and gas molecules, (a) physisorption, (b) chemisoption, (b) non-reversible reaction.

(3) Non-reversible reactions with the solid surface typically lead to the formation of new compounds, which will result in the difficulties of desorption of the gas and is undesired for gas sensor operation as illustrated in Figure 1.5(c).

The electrical and gas sensing properties of the metal oxide strongly depend on the morphology and thus the used fabrication process. Typical conduction mechanisms are grain-boundary-controlled or neck-grain-boundary-controlled in porous thick film devices and surface-controlled in compact thin film devices [67]. Depending on the crystallite grain size and the Debye length of the material the gas sensitive layers will be partly or completely depleted/accumulated due to oxygen ionosorption at the surface [68].

It was claimed that the oxygen molecules will be decomposed as molecular (O_2^-), atomic (O^- and O^{2-}) ions, when the oxygen were chemically adsorbed onto the surface of the metal oxide sensor at working conditions. The negative charges trapped in these oxygen species causes an upward band bending and thus a reduced conductivity compared to the flat band situation [69].

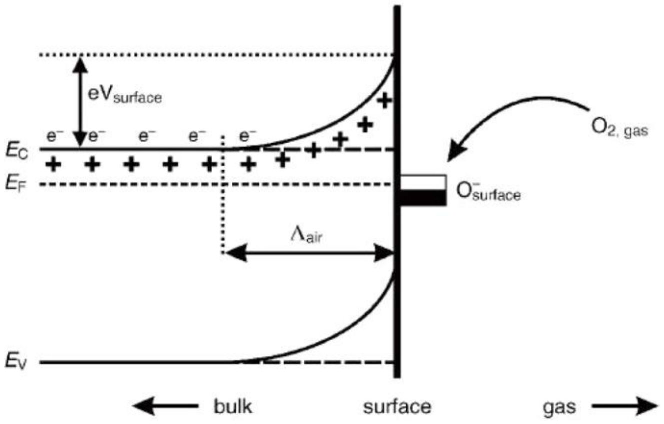

Figure 1.6 Schematic diagram of band bending after chemisorptions of charged species (here the ionosorption of oxygen) E_C, E_V, and E_F denote the energy of the conduction band, valence band, and the Fermi level, respectively, while Λ_{air} denotes the thickness of the space-charge layer, and $eV_{surface}$ denotes the potential barrier. The conducting electrons are represented by e^- and + represents the donor site [69].

As shown in Figure 1.6, when O_2 molecules are adsorbed on the surface of metal oxides, they would extract and trap the electrons at the surface in the form of ions, i.e. O^- and O^{2-} [70]. This process will lead to an electron-depleted region at the surface of the crystalline grain. The electron-depleted region is so called space-charge layer, whose thickness is the length of band bending region. The space-charge layer exhibits the high resistance. On the contrary, when the reductive gases flowing onto the surface of the metal oxide, the reactions of these oxygen species with gas can set the extracted electrons free, then reverse the band bending, resulting in an increased conductivity.

Within the adsorbed oxygen species, O^- is found to be dominant at the operating temperature of 300 - 450 °C, which is the work temperature for most metal oxide gas sensors. Figure 1.6, 1.7 schematically shows the structural and band model of conductive mechanism upon exposure to reference gas with or without CO (for example) When gas sensors exposure to the reference gas, i.e. CO, CO is oxidized by O^- and released electrons to the bulk materials. Together with the decrease of the number of surface O^-, the thickness of space-charge layer decreases. Then the schottky barrier between two grains is lowered. The electrons would be easy to conduct in sensing layers through different grains. The width of the space charge region can be estimated using the Debye length [71]

$$L_D = \sqrt{\frac{kT\epsilon_r\epsilon_0}{q^2N}} \tag{1.1}$$

The Debye length is influenced by temperature *T*, relative permittivity ϵ_r and density of majority carriers *N*. Thus it is a parameter determined by material properties and by sensor operation conditions [71, 72].

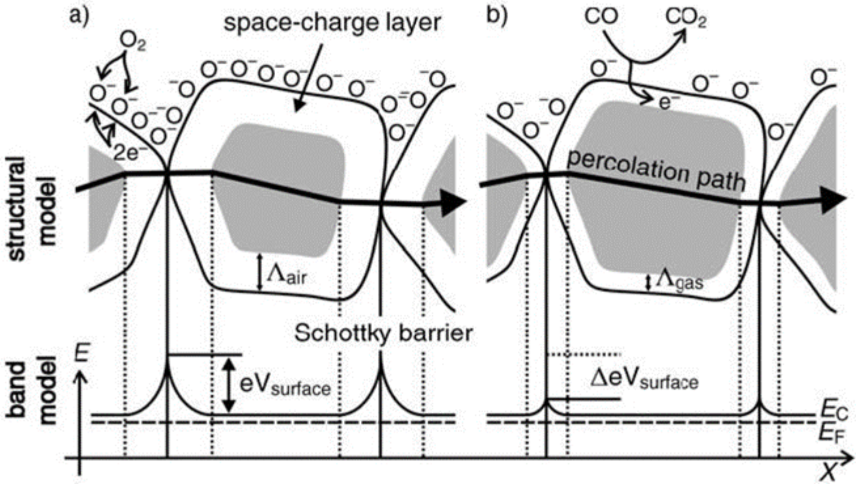

Figure 1.7 Structural and band models of conductive mechanism upon exposure to target gas. (a) with or (b) without CO [69].

Based on the theory of grain-boundary transportation, MoO_3 exhibits a special adsorb mechanism for gas species, such as H_2 or hydroxyl based alcoholic material. Different from other typical metal oxide semiconductors (SnO_2 or ZnO), the gas detection process of α-MoO_3 mainly dominated by surface lattice oxygen rather than chemisorbed oxygen. Alsaifa et al.[73-75] insist that hydrogen ions etc. can be intercalated into van der Waals's gaps of α-MoO_3, accompanied with the lower oxidation state. When the VOCs, e.g., EtOH, were adsorbed onto the surface of the MoO_3, the -OH bond of the adsorbed EtOH dissociated heterolytically to yield ethoxide groups and hydrogen as follows [76]

$$C_2H_5OH_{(ads)} \rightarrow C_2H_5O^-_{(ads)} + H^+_{(ads)} \quad (1.2)$$

Subsequently, the H^+ ions will spill over the (010) plane of MoO_3 [77-79], and then interact with the lattice corner-sharing oxygen atoms, forming theoretical -OH_2 groups and H_xMoO_3 structures. At elevated operating temperatures, H_2O molecules are eventually formed, through leaving oxygen vacancies, i.e., MoO_{3-x}. Each of the possible reactions was described by the following equations.

$$MoO_3 + xH^+ + xe^- \rightarrow H_xMoO_3 \quad (1.3)$$

$$2H_xMoO_3 \rightarrow xH_2O + 2MoO_{3-x/2} \quad (1.4)$$

Besides the H^+ ion intercalation, the ethoxide groups $C_2H_5O^-$ will form an ionic bond with the unsaturated metal site. The adsorbed hydroxyl groups then undergo dehydrogenation with subsequent proton donation to the cation, due to the reducible cationic nature of Mo, as illustrated in Equations (1.5) and (1.6)

$$C_2H_5OH^-_{(ads)} + H^+(ads) + \text{-O-Mo-O-Mo} \rightarrow \text{-OH(ads)} + C_2H_5\text{O-Mo-O-Mo} \quad (1.5)$$

$$C_2H_5\text{O-Mo-O-Mo} \rightarrow CH_3CHO + \text{Mo-O-Mo-H} \quad (1.6)$$

The acetaldehyde will undergo subsequent oxidation to form H_2O and CO_2. The adsorbed hydroxyl groups are assumed to be desorbed as H_2O, leaving the surface with oxygen vacancy.

1.3.2 MoO_3 based gas sensing properties from perspective of nanotechnology

Researchers are taking their efforts to increase specific surface area of active materials to increase the performance of gas sensing properties. Increasing the specific surface area can effectively increase active sites at the surface of materials, for the catalytic reaction between target gas and adsorbed oxygen on the surface of sensor. Since reducing grain size can greatly increase surface area, the synthesis of low dimensional nanostructured metal oxides have attracted much attention [80, 81].

Depending on a type of materials, morphology, size and fabrication process, the performance of a sensor towards a specific gas shows a varying degree of sensing ability [82]. α-MoO_3 is an n type semiconductor metal oxide which indicated that the resistance will decrease/increase when α-MoO_3 is exposed to reductive gas/oxidized gas. Recently, gas sensing properties of nanostructured α-MoO_3 are focused much attentions due to their available special morphologies for the adsorption/diffusion of gas molecules.

Typical gas sensing properties of nanostructures of MoO_3 were summerized in the Table 1.1. It can be found that MoO_3 is very sensitive to various gas species, depending on their special nanostructures and synthesis process. For example, nanostructured MoO_3 can be very sensitive to nitrogen dioxide (NO_2) [70, 91, 94-96], nitrogen monoxide (NO) [97-100], carbon monoxide (CO) [101-103], trimethylamine (C_3H_9N) [104-108], ethanol(C_2H_6O) [89, 109-115], methane (CH_4) [116, 117], methanol (CH_3OH) [18, 118-120], ammonia (NH_3) [121-127]and hydrogen (H_2) [90, 128]. Most of these nanostructures were working at 200 – 400 ^{o}C.

Table 1.1 Review of gas sensing properties of nanostructures of MoO_3

Structure	Size	Method	Gas	Concentration (ppm)	Sensitivity	Work temperature	Ref.
2D-nanosheets	220-256 nm	Ultrasonic	Ethanol	100	32	300 °C	[83]
Hollow Nanostructures	0.2-2.5 µm	Hydrothermal	Ethanol	300	500	200 °C	[84]
Nanoparticles	100 nm	Hydrothermal	H_2S	20	450	350 °C	[85]
Nanobelts	100 nm	Hydrothermal	Xylene	100	7	200 °C	[86]
Thin film		Sol-gel	O_2	1000	40	370 °C	[87]
Lamellar	2 µm	Evaporation	NO_2	10	1.1	225 °C	[88]
Thin film		Sputtering	NO_2	3	2	300 °C	[70]
Microrods	5 µm	Hydrothermal	Ethanol	500	8	332 °C	[89]
Nanoplate	1 um	Evaporation	H_2	10000	1.1	265 °C	[90]
Nanorods	200 µm	Ultrasonic	NO_2	10	46	300 °C	[91]
Nanoplate	1 um	CVD	Formalehyde	1000	1.03	30 °C	[92]
Nanorods	100 nm	Sputtering	Ethanol	1000	110	300 °C	[93]

Recently, environmental pollution due to volatile organic compounds (VOCs) has become one of the critical problems in recent years because it causes not only global warming and climate change but also has adverse effects on human health. VOCs are hazardous because exposure to them can cause conjunctival irritation, nose and throat discomforts, headache, allergic skin reaction, dyspnoea, decreased serum cholinesterase levels, nausea, emesis, epistaxis, fatigue, and dizziness. Therefore, the development of VOC gas sensors for air quality monitoring is necessary to help people to avoid over-exposure to such dangerous agents and to reduce the levels of environmental pollutants [129, 130]. As one kind of VOCs, ethanol is often used in a laboratory of a factory. Therefore, to detect the concentration of ethanol is very important for both the process control and safety.

From table 1.1, it can be found that several groups are researching on the gas sensing properties of MoO_3 to VOCs vapors. For example, Li-Li Xing et al. synthesized the MoO_3 nanobelts through the hydrothermal route, with a width of 140 – 200 nm, showed a sensitivity of 31 to ethanol at 300 ^oC [55]. Navas Illyaskutty et al. synthesized MoO_3 thin film, through the RF sputtering method, showed a sensitivity of 38 to ethanol [112]. Li-Li Sui et. al synthesized flower-like microstructure MoO_3, which showed a sensitivity of 6 to 500 ppm ethanol vapor at 250 ^oC, by the hydrothermal route [131]. Wen Zeng et al. synthesized the net-like MoO_3 porous architectures, showed a sensitivity of 17 to 500 ppm ethanol vapor at 350 ^oC by the hydrothermal route [132]. These reports revealed MoO_3 displays appealing sensing performance to VOCs vapors. However, these methods employed complicated manufacturing processes. For instance sputtering process needs the complicated vacuum system [112]. Hydrothermal process requires the high-pressure and long-time synthesis procedures [132]. Moreover, the as-synthesized MoO_3 are required to be transferred to substrates with electrodes, which further increased the fabrication costs.

Thus, developing much simpler, lower cost route for further enhancing performance of a MoO_3 based gas sensor is an urgent issue. Moreover, as mentioned at chapter 1.2, nanorod arrays morphology is very promising for the penetration of gases in their structure. Nevertheless, the gas sensing properties of charming MoO_3 nanorod arrays haven't been researched. In this work, the author aimed to synthesize MoO_3

nanorod arrays with a much simple solution process and researched the gas sensing property of the nanorod arrays sensors.

1.3.3 Characterization of the gas sensors

Sensitivity, response and recovery time are three of the important performance parameters for gas sensors. For a n-type gas sensor, when being exposed to air, the sensor will show higher resistance due to the aforementioned charge depletion layer. When the sensor is exposed to the target gas, it will show a reduced resistance due to the decrease of the charge depletion layer. The sensitivity of is defined as the ratio of the device's resistance, when sensors are exposed to the ambient air and to target species, as shown in equition (1.7).

$$S = \frac{R_a}{R_g} \tag{1.7}$$

where R represents the resistance of the metal oxide, the subscript 'g' represents target gas, and 'a' represents ambient air. Sensitivity indicate the reaction ability of a sensor with target gas. Response/recovery time is defined as the time period needed for the device to undergo resistance changing from 10%/90% to 90%/10% of the value in equilibrium upon exposure to an oxidizing/reducing analyte [115]. Response/recovery time reveals the adsorption/desorption ability of a sensor to a target gas. A better gas sensor should exhibit both high sensitivity and quicker response/recovery time.

1.4 Molybdenum oxide base hole transport layer for organic solar cell

1.4.1 Review of organic solar cell

With the rapid growth of industry and population, more and more energy are required to sustain the corresponding economy growth year by year. It is estimated that in 2050 year, the total energy needed in the world will reach to 28 Terawatt about twice of in 2009. However the tradition fossil fuel energy is undesired to provide so much energy. Because fossil fuel is limited with the total reserves and too much CO_2 releasing into the atmosphere, scientists are investigating the alternative energies to substitute fossil fuel. Thus, clean and renewable energy such as solar (both photovoltaics and solar thermal), wind, hydro, geothermal, tidal, and biofuels are attracting more and more attention. Within these renewable energies, solar energy is one of the most plentiful energies due to sun radiation to the earth can reach to 23000 TW/year. Therefore, considerable effort has been paid to study how to increase the performance of solar cells to make use of effective energy [133].

After Bell Laboratories developed the first inorganic solar cell in 1954, the most representative photovoltaic conversion efficiency (PCE) of Si-based solar cell have reached to its theoretical limitations of about 25 %. The most advanced (and expensive) GaAs cells have gotten the PCE above 40 % [134, 135]. Recently, Organic solar cells (OSCs) are attracting widely interests in producing clean and renewable energy by virtue of their low cost, light weight, colorful, portable and ease of large-area fabrication. The first photoconductivity in the organic compound was observed in anthracene in 1906 [136]. After the photovoltaic effect was observed in an organic material in the 1960s [137], substantial progress has been achieved in increasing the power conversion efficiency (PCE) of single-junction OSCs, with values approaching to 10-12 % [39, 138].

The difference between the organic semiconductor and inorganic solid-state semiconductors lies in the generally poor charge-carrier mobility in organics ($10^{-5} – 10^{0}$ cm^2/Vs, while mobility of Si can reach to the extent of 10^4 cm^2/Vs [139, 140]), which has a large effect on the design and efficiency of organic semiconductor devices. However, organic semiconductors have relatively strong absorption coefficients of $\geq 10^5$ cm^{-1}, which will give high absorption in even <100 nm thin devices. Another important difference to crystalline inorganic semiconductors is the relatively small diffusion length of primary photoexcitations in amorphous and disordered organic materials. Most of the organic semiconductors for the organic solar cells are p-type conductors and have an optical band gap around 2 eV, which is higher than that of silicon of 1.12 eV. Moreover, chemical synthesis methods, which show the perspective of low cost, large-scale, and flexible organic solar cells, drives the research both in academia and in industry [141-143].

Here, the mechanism of solar cell is presented. When light enters the cell through the transparent anode, the light is absorbed in the bulk heterojunction layer to generate the excitons. In order to make excitons to form charge carriers at the heterojunction interface, the offset of the energy bands of the two materials must be greater than the binding energy of the excitons [144-146]. Therefore, an efficient OSCs device employed a layer structure, schematic of which were shown in Figure 1.8.

At the middle of the cell is the conjugated polymer:fullerene (Usually $C_{60/70}$ and $C_{60/70}$ derivatives) composites based active layer, which response for generating the excitons when being exposed by photons, due to the photoinduced electron transfer from optically excited conjugated polymers to the $C_{60/70}$ molecule. The charge transfer in organic solar cell was schematically shown in Figure 1.9.

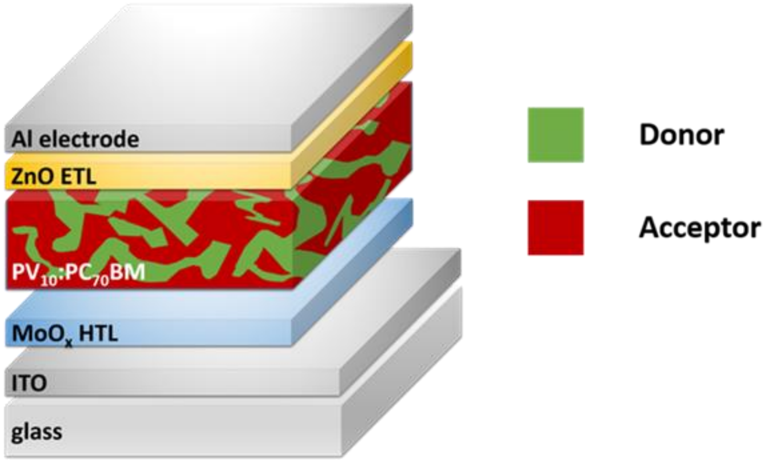

Figure 1.8 Schematic of the layer structured organic solar cell. [141]

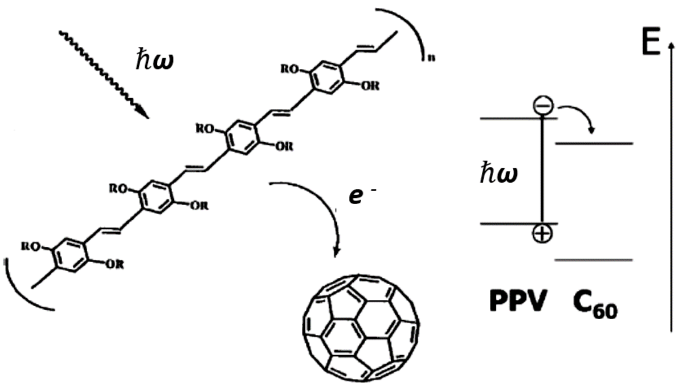

Figure 1.9 Illustration of photoinduced charge transfer (left) with a sketch of energy level scheme (right). After excitation in PPV polymer, electron is transferred to a C_{60} due to its higher electron affinity [141].

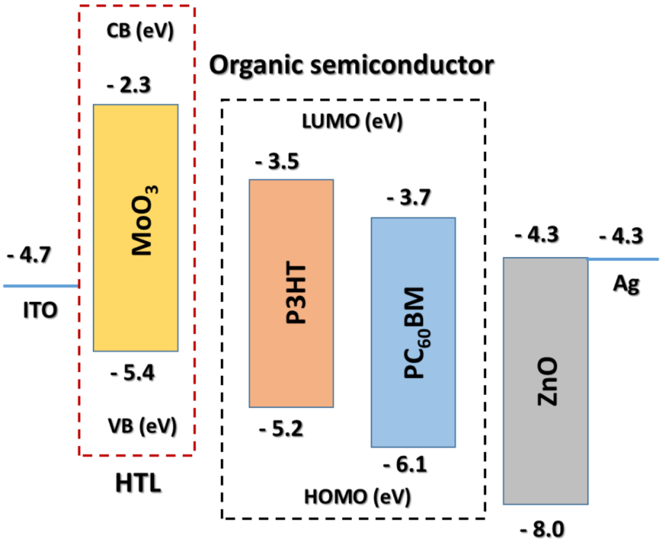

Figure 1.10 Illustration of energy level of hole transport layer in organic solar cell

The excitons diffuse in the bulk heterojunction until they either recombine or reach a donor-acceptor interface, where they were separated into electrons and holes. Therefore it is important to choose the desirably interfacial materials such that the charge carriers have an energetically favorable path to electrodes, while still retaining some voltage at output. Finally, electrons and holes will then move to anode and cathode, through a donor and acceptor material phase [147].

As shown in Figure 1.8, between the electrodes and the active layer interfaces, there are two ultra-thin electron (only several nanometer in thickness) and hole transport layers (ETLs and HTLs). The ETLs / HTLs were developed to efficiently extract the excited electron and hole-electron pairs from photo active bulk heterojunction layer to transport to the respective electrodes, due to their well aligned energy level with the LUMO (lowest unoccupied molecular orbital) / HOMO (highest occupied molecular orbital) of the active layer [148, 149]. Energy level of hole transport layer in organic solar cell was shown in Figure 1.10.

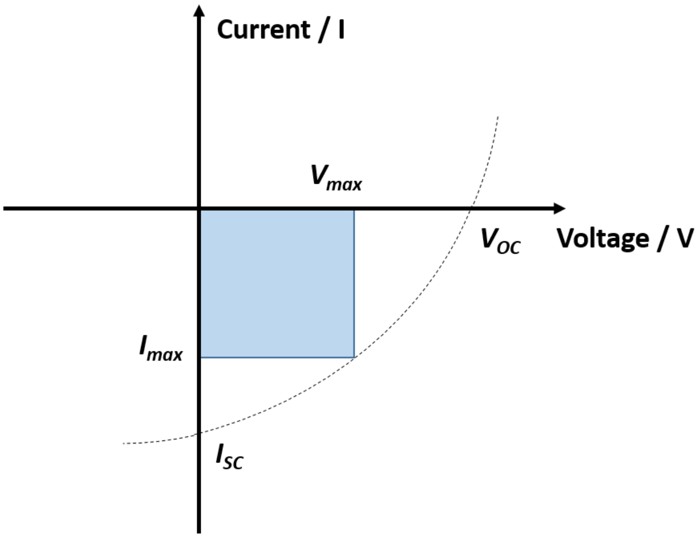

Figure 1.11 Typical I-V curves of the solar cells [150].

1.4.2 Characterization of organic solar cell

Usually, solar cell is characterized with the curve of its current and voltage (I-V curve) as schematically shown in Figure 1.11. Some important parameters of solar cell performance can be extracted from Figure 1.11.

- Open circuit voltage (V_{oc}): Open circuit voltage is the voltage the cell produces when it is sourcing no current and represents the maximum voltage of the cell (i.e. I = 0).
- Short circuit current (I_{sc}): The short circuit current is the current the cell can produce when the two electrodes are shorted together (i.e. V = 0)
- Fill factor (FF): Fill factor is the ratio of the actual maximum power to the ideal maximum power; the actual maximum power is the product of voltage and current of the point show in Figure 1.11, the ideal maximum power is the product of V_{oc} and I_{sc}, as shown in the equition

$$FF = \frac{P_{MAX}}{P_T} = \frac{V_{MP} I_{MP}}{V_{OC} I_{SC}} \tag{1.8}$$

- Power conversion efficiency (PCE): divide the maximum power output by the power of the incident light:

$$PCE = \frac{P_{MAX}}{P_{IN}} \tag{1.9}$$

- Series resistance (R_s): reciprocal of tangent of the I-V curves at V_{oc}.
- Shunt resistance: tangent of the I-V curves at I_{sc}.

The series resistance (R_s) and shunt resistance, can also be found by modeling a solar cell as a current source in parallel with a diode with two resistive elements as Figure 1.12.

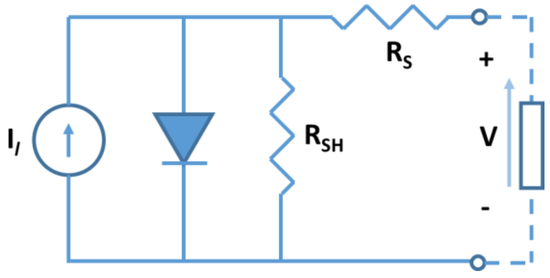

. **Figure 1.12** Circuit equivalent of the organic solar cells [150]

The effects of these two non-idealities are shown in Figure 1.12. So the current delivered to the load becomes that of the current source (from the photovoltaic effect) minus the losses from the diode and the resisters,

$$I = I_l - I_0 \left\{ exp\left[\frac{q(V+IR_S)}{nkT}\right] - 1 \right\} - \frac{V+IR_S}{R_{SH}} \tag{1.10}$$

where I_0 is the reverse bias saturation current, q is the charge of the electron, n is the ideality factor of the diode, k is Boltzmann's constant, and T is temperature.

1.4.3 HTL for the organic solar cells

As aforementioned, an efficient OSC device structure contains electron and hole transport layers (ETL and HTL, respectively) between electrodes. In this structure, the active layer interfaces efficiently extract excited electron–hole pairs from the photoactive bulk heterojunction layer and transport them to the respective electrodes. Therefore, investigating the optimum OSC interfacial layers with improved energy level alignment and simple, effective processing methods is desirable to produce OSCs with suitable performance at lower cost [151, 152].

Traditionally, poly(3,4-ethylenedioxythiohene):poly(styrenesulfonate) (PEDOT:PSS) is used as the HTL in OSCs because of its easy processability, smooth surface, high transparency, good conductivity, excellent mechanical flexibility, and the match of its work function (5.1 eV) with the highest occupied molecular orbital level of many donor-type organic semiconductors[153]. However, the hydrophilic and acidic nature (pH ≈ 1) of PEDOT:PSS will introduce water into devices and degrade metal or indium tin oxide electrodes, which dramatically deteriorate the performance of OSCs under ambient conditions. Therefore, to develop a suitable substitute of PEDOT:PSS is an urgent issue [154].

The charge-injection properties of the HTL in a device depends on its electronic structure, i.e. whether the oxide is p- or n-type, wide or narrow band gap, or a metallic conductor. Potential alternatives to PEDOT:PSS are transition metal oxides with high work function (Φ_m), such as MoO_3 (Φ_m = 5.5 eV), V_2O_5 (Φm = 4.7 eV), NiO (Φ_m = 5.0 eV), and WO_3 (Φ_m = 4.8 eV) [155]. Schematic energy-level diagrams of various transition metal oxides and several common organic semiconductors are shown in schematic energy-level diagrams, Figure 1.13. [156, 157]. Devices with these metal oxide HTLs display comparable or improved efficiency and stability compared with those of the equivalent ones with PEDOT:PSS[154, 158]. MoO_3 is one of the most desirable metal oxides for use in HTLs because of its wide band gap (3.0 – 3.8 eV) and high transparency (> 80 %) in the visible and near-infrared regions [159-161]. Crystalline MoO_3 exhibits diverse arrangements of Mo and O atoms within its lattice, resulting in α-, β-, and h-phases. Mo-based oxides with different molybdenum:oxygen stoichiometry also display a variety of Femi levels, densities of states, band structures, and conductivities. The diversity of crystal structure and polyvalence of MoO_3 make it suitable for use as various effective extraction of holes in OSCs [162]. For example, Yang et al. [163] found that OSCs with a MoO_3 HTL showed a fill factor of 61.9 %, which was higher than that of the counterpart with evaporated V_2O_5 (59.1 %).

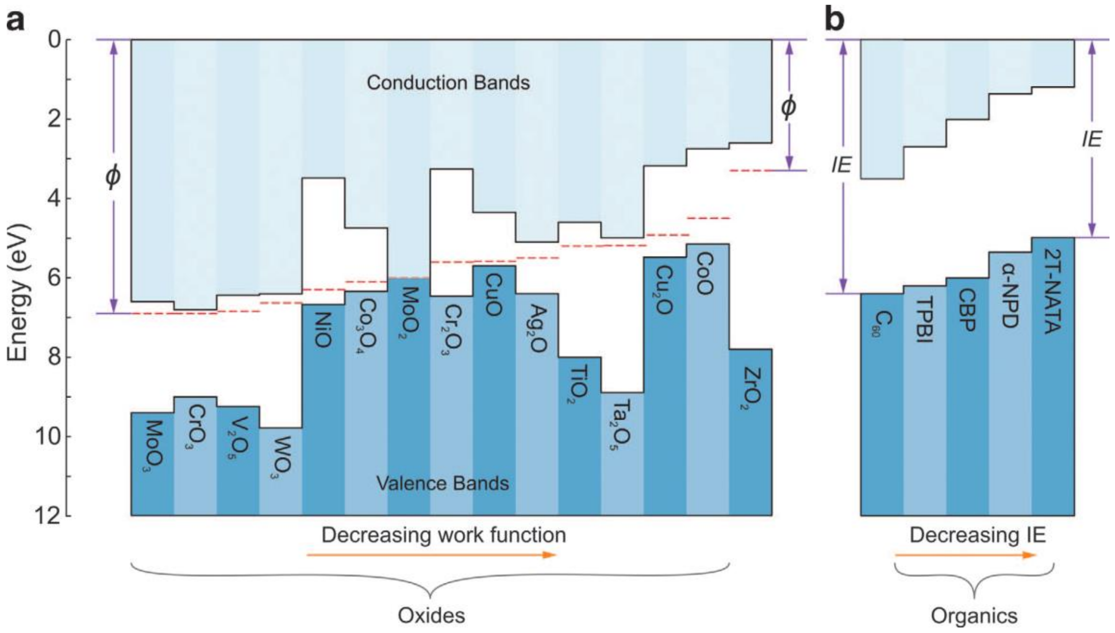

Figure 1.13 Schematic energy-level diagrams of (a) several transition metal oxides and (b) several organic semiconductors. The lower shaded regions represent the valence bands and the upper shaded regions represent the conduction bands [156, 157].

Homogenous smooth MoO_3 HTLs have been fabricated by evaporation and demonstrated as high performance in OSCs [164]. However, evaporation method is a time-consuming and complicated vacuum process that increases the manufacturing cost of OSCs and is incompatible with a large-area processing needed to produce flexible OSCs. Moreover, because evaporated MoO_3 ($eMoO_3$) is very sensitive to contaminants [165], evaporation process demands a high-purity MoO_3 source which further increases the fabrication cost of the OSCs. In addition, heating MoO_3 with an oxidation state of +6 during thermal evaporation leads to severe loss of oxygen, so the final deposited layer will have a lower oxidation state of +5 or even +4 (MoO_2). The lower oxidation state of Mo changes its energy levels and lowers its work function, making it less suitable for extracting holes from the active layer. It has been shown that MoO_2 with an oxidation state of +4 has similar electrical properties to those of Mo metal, which cannot act as an optimum HTL for OSCs [166].

Recently, solution-processed MoO_x ($sMoO_x$) interfacial HTLs have become widely preferred to fulfill the requirements of all-solution-processed OSCs by virtue of their precise composition control, homogeneity, large-area compatibility, flexibility, and low processing cost [167-169] compared with those of counterparts with an $eMoO_x$ or PEDOT:PSS HTL. However, there are still several difficulties to fabricate efficient OSCs with solution-processed HTLs, which are:

(1) Usually, high temperature annealing is needed to convert the precursors to MoO_x, which increases the manufacturing cost and limits the choice of flexible substrates. For example, Girotto et al. [170] fabricated $sMoO_3$-based OSCs with a fill factor of 65 %. However, the solution process needed a complicated reflux procedure and the annealing temperature (275 °C) was too high to be compatible with flexible substrates like Polyethylene naphthalate (PEN) or Polyethylene Terephthalate (PET). Murase and colleagues [171] developed a $(NH_4)_6Mo_7O_{24}\cdot 4H_2O$ solution decomposition route to fabricate OSCs with a high fill factor of 69.3 %. However, this process involved a long annealing time of 1 h, which limited the production speed and increased cost.

(2) Intrinsic $sMoO_x$ shows a high resistance, which will increase the series resistance and degrade the overall performance of OSCs. Wang et al. [172] developed a low-temperature (120 °C) solution process to form MoO_x HTLs, but the layers displayed high resistance and gave devices with insufficient performance. To settle the problem of high resistance, Li and co-workers [173] treated $sMoO_x$ HTLs in N_2 to produce oxygen vacancies in order to increase conductivity. To further increase the conductivity of $sMoO_x$, silver (Ag) particles were also added, which although enhanced the PCE of the resulting devices, increased the cost of the fabrication processes at last. Very recently, a conductive $sMoO_x$ HTLs were developed by our group, the improved performance of the resulting OSCs were reported [174].

1.5 Motivation and objective of this dissertation

Mo oxide has found various kinds of applications due to their fascinating crystal and electron structures. The main objective of this thesis is to synthesize α-MoO_3 nanorod arrays and MoO_x thin films through a simple solution process. The author try to investigate the gas sensing properties of α-MoO_3 nanorod arrays, and investe the hole transport abilities of MoO_x thin films in organic solar cells.

In chapter two, the author tried to synthesize α-MoO_3 nanorod arrays through a simple solution process combined with a short time annealing process in air. Solution process is very promising for the synthesis of oxide with nanoparticles and nanospheres morphologies, by virtue of homogeneous, large area, and low cost. However, solution process is facing great difficulties in controlling the anisotropic growth only in one directions, i.e. nanorods, due to the unconstrained growth condition which is different from the high pressure condition in the hydrothermal method. The author tried to synthesize α-MoO_3 nanorod arrays with controllable morphologies by adjusting the preparation parameters, such as molar ratio in precursors, annealing temperature and time.

In chapter three, the author tried to applicate α-MoO_3 nanorod arrays into gas sensors. Nanorod arrays morphologies are very desirable for gas sensing applications, because they not only possess high specific surface area but also facilitate the contact and diffusion of reagent gas molecules into the inner region of nanorod arrays. Metal oxide nanorod arrays composed of WO_3, ZnO, and SnO_2 have been demonstrated to be very sensitive to VOC vapors [175-177]. However, few α-MoO_3 nanorod arrays based gas sensors were reported because the complexities in common synthesis process of α-MoO_3 nanorod arrays, *i.e.*, complicated vacuum system or high pressure process, are restraining their application as gas sensors. The author has attempted to investigate the solid/gas reaction abilities of α-MoO_3 nanorod arrays with VOCs, and tried to find the dominantly morphological parameters for gas sensing properties.

In chapter four, the author tried to fabricate MoO_x based HTL for organic solar cell through a solution process. Solution process is expected to substitute evaporation process to fulfill entire solution process to decrease the fabrication cost of the OSCs. However the solution process are facing challenges of controlling the oxygen composition in MoO_x, which are dominating Femi level and band structure so as to hole transport abilities in OSCs. The author tried to control the oxygen stoichiometry in MoO_x through adjusting the composition in precursors. The optimized MoO_x will be used to fabricate the HTL of the OSCs which is expected to exhibit the same PCE with the referential cell from the evaporation process.

Thus, this study paves the way for the fabrication of α-MoO_3 nanorod arrays with controlled morphologies and MoO_x thin film with tunable oxygen composition; for the fabrication of their corresponding devices of gas sensors and organic solar cells with high performance by the relative simple, inexpensive, and scalable processing methods.

References

[1] Gabay M, Triscone J-M. Transition-metal oxides: It takes two to waver. Nature nanotechnology 2014;9:417.

[2] Luo K, Roberts MR, Hao R, Guerrini N, Pickup DM, Liu Y-S, Edström K, Guo J, Chadwick AV, Duda LC. Charge-compensation in 3d-transition-metal-oxide intercalation cathodes through the generation of localized electron holes on oxygen. Nature Chemistry 2016.

[3] Poizot P, Laruelle S, Grugeon S, Dupont L, Tarascon J. Nano-sized transition-metal oxides as negative-electrode materials for lithium-ion batteries. Nature 2000;407:496.

[4] Al-Kuhaili MF, Durrani SMA, Bakhtiari IA, Al-Shukri AM. Optical constants and thermocoloration of pulsed laser deposited molybdenum oxide thin films. Opt. Commun. 2010;283:2857.

[5] Guerfi A, Dao LH. Electrochromic molybdenum oxide thin-films prepared by electrodeposition. J. Electrochem. Soc. 1989;136:2435.

[6] Zhou J, Xu NS, Deng SZ, Chen J, She JC, Wang ZL. Large-area nanowire arrays of molybdenum and molybdenum oxides: synthesis and field emission properties. Advanced Materials 2003;15:1835.

[7] Khademi A, Azimirad R, Zavarian AA, Moshfegh AZ. Growth and field emission study of molybdenum oxide nanostars. J. Phys. Chem. C 2009;113:19298.

[8] Rouhani M, Hobley J, Subramanian GS, Phang IY, Foo YL, Gorelik S. The influence of initial stoichiometry on the mechanism of photochromism of molybdenum oxide amorphous films. Sol. Energy Mater. Sol. Cells 2014;126:26.

[9] Rouhani M, Foo YL, Hobley J, Pan JS, Subramanian GS, Yu XJ, Rusydi A, Gorelik S. Photochromism of amorphous molybdenum oxide films with different initial Mo^{5+} relative concentrations. Appl. Surf. Sci. 2013;273:150.

[10] Brezesinski T, Wang J, Tolbert SH, Dunn B. Ordered mesoporous alpha-MoO_3 with iso-oriented nanocrystalline walls for thin-film pseudocapacitors. Nat. Mater. 2010;9:146.

[11] Chang J, Jin M, Yao F, Kim TH, Le VT, Yue H, Gunes F, Li B, Ghosh A, Xie S, Lee YH. Asymmetric supercapacitors based on Graphene/MnO_2 nanospheres and Graphene/MoO_3 nanosheets with high energy density. Adv. Funct. Mater. 2013;23:5074.

[12] Sheehan PE, Lieber CM. Nanotribology and nanofabrication of MoO_3 structures by atomic force microscopy. Science 1996;272:1158.

[13] Greiner MT, Chai L, Helander MG, Tang WM, Lu ZH. Metal/metal-oxide interfaces: how metal contacts affect the work function and band structure of MoO_3. Adv. Funct. Mater. 2013;23:215.

[14] Scanlon DO, Watson GW, Payne DJ, Atkinson GR, Egdell RG, Law DSL. Theoretical and experimental study of the electronic structures of MoO_3 and MoO_2. J. Phys. Chem. C 2010;114:4636.

[15] Kalantar-zadeh K, Tang JS, Wang MS, Wang KL, Shailos A, Galatsis K, Kojima R, Strong V, Lech A, Wlodarski W, Kaner RB. Synthesis of nanometre-thick MoO_3 sheets. Nanoscale 2010;2:429.

[16] Balendhran S, Walia S, Nili H, Ou JZ, Zhuiykov S, Kaner RB, Sriram S, Bhaskaran M, Kalantar-zadeh K. Two-dimensional molybdenum trioxide and dichalcogenides. Adv. Funct. Mater. 2013;23:3952.

[17] Carcia PF, McCarron EM. Synthesis and properties of thin-film polymorphs of molybdenum trioxide. Thin Solid Films 1987;155:53.

[18] Phuc NHH, Phuong PTT, Tai VT, Huan NM, Duy NPH, Loc LC. Synthesis of alpha-MoO_3 thin sheets and their catalytic behavior for selective oxidation of methanol to formaldehyde. Catal. Lett. 2016;146:391.

[19] Hu JB, Ramadan A, Luo F, Qi B, Deng XJ, Chen J. One-step molybdate ion assisted electrochemical synthesis of alpha-MoO_3-decorated graphene sheets and its potential applications. J. Mater. Chem. 2011;21:15009.

[20] Yayapao O, Phuruangrat A, Thongtem T, Thongtem S. Synthesis, characterization and electrochemical properties of alpha-MoO_3 nanobelts for Li-ion batteries. Russ. J. Phys. Chem. A 2016;90:1224.

[21] Schuppert ND, Mukherjee S, Bates AM, Son EJ, Choi MJ, Park S. Ex-situ X-ray diffraction analysis of electrode strain at TiO_2 atomic layer deposition/alpha-MoO_3 interface in a novel aqueous potassium ion battery. J. Power Sources 2016;316:160.

[22] Hu B, Mai LQ, Chen W, Yang F. From MoO_3 Nanobelts to MoO_2 Nanorods: Structure Transformation and Electrical Transport. ACS Nano 2009;3:478.

[23] Si LL, Yuan ZQ, Liang JW, Hu L, Zhu YC, Qian YT. Fabrication of one-dimensional SnO_2/MoO_3/C nanostructure assembled of stacking SnO_2 nanosheets from its heterostructure precursor and its application in lithium-ion batteries. J. Mater. Chem. A 2014;2:9784.

[24] Parviz D, Kazemeini M, Rashidi AM, Jozani KJ. Naphtha hydrodesulfurization over micro and nanostructure MoO_3 catalysts. Sci. Iran. 2011;18:479.

[25] Gong JW, Wan XF. Hydrothermal synthesis of different nanostructure MoO_3 sensing materials: application for transformer fault diagnosis. Mater. Technol. 2015;30:332.

[26] Arbiol J, Morante JR, Bouvier P, Pagnier T, Makeeva EA, Rumyantseva MN, Gaskov AM. SnO_2/MoO_3-nanostructure and alcohol detection. Sens. Actuator B-Chem. 2006;118:156.

[27] Parise JB, McCarron EM, Vondreele R. Beta-MoO_3 produced from a novel freeze-drying route. J. Solid State Chem. 1991;93:193.

[28] Parise J, McCarron E, Von Dreele R, Goldstone J. β-MoO_3 produced from a novel freeze drying route. J. Solid State Chem. 1991;93:193.

[29] Pan WZ, Tian RY, Jin H, Guo YJ, Zhang LP, Wu XC, Zhang LN, Han ZH, Liu GY, Li JB, Rao GH, Wang HF, Chu WG. Structure, optical, and catalytic properties of novel hexagonal metastable h-MoO_3 nano- and microrods synthesized with modified liquid-phase processes. Chem. Mat. 2010;22:6202.

[30] Brandt BG, Skapski AC. A refinement of crystal structure of molybdenum dioxide. Acta Chem. Scand. 1967;21:661.

[31] Kumari L, Ma YR, Tsai CC, Lin YW, Wu SY, Cheng KW, Liou Y. X-ray diffraction and Raman scattering studies on large-area array and nanobranched structure of 1D MoO_2 nanorods. Nanotechnology 2007;18:7.

[32] Rao M, Ravindranadh K, Kasturi A, Shekhawat M. Structural stoichiometry and phase transitions of MoO_3 thin films for solid state microbatteries. Research Journal of Recent Sciences 2013;2277:2502.

[33] Wooster N. The crystal structure of molybdenum trioxide, MoO_3. Z. Kristall. 1931;80:504.

[34] Andersson G, Magneli A. On the crystal structure of molybdenum trioxide. Acta Chem. Scand. 1950;4:793.

[35] Huang PR, He Y, Cao C, Lu ZH. Impact of lattice distortion and electron doping on alpha-MoO_3 electronic structure. Sci Rep 2014;4:7.

[36] Vasilopoulou M, Douvas AM, Georgiadou DG, Palilis LC, Kennou S, Sygellou L, Soultati A, Kostis I, Papadimitropoulos G, Davazoglou D, Argitis P. The influence of hydrogenation and oxygen vacancies on molybdenum oxides work function and gap states for application in organic optoelectronics. J. Am. Chem. Soc. 2012;134:16178.

[37] Barsan N, Weimar U. Understanding the fundamental principles of metal oxide based gas sensors; the example of CO sensing with SnO_2 sensors in the presence of humidity. J. Phys.-Condes. Matter 2003;15:R813.

[38] Meixner H, Gerblinger J, Lampe U, Fleischer M. Thin-film gas sensors based on semiconducting metal-oxides. Sens. Actuator B-Chem. 1995;23:119.

[39] Liu Y, Chen C-C, Hong Z, Gao J, Yang YM, Zhou H, Dou L, Li G, Yang Y. Solution-processed small-molecule solar cells: breaking the 10% power conversion efficiency. Sci Rep 2013;3.

[40] Hughes GA. Nanostructure-mediated drug delivery. DM-Dis.-a-Mon. 2005;51:342.

[41] Thostenson ET, Ren ZF, Chou TW. Advances in the science and technology of carbon nanotubes and their composites: a review. Compos. Sci. Technol. 2001;61:1899.

[42] Reed MA, Randall JN, Aggarwal RJ, Matyi RJ, Moore TM, Wetsel AE. Observation of discrete electronic states in a zero-dimensional semiconductor nanostructure. Phys. Rev. Lett. 1988;60:535.

[43] Busche C, Vila-Nadal L, Yan J, Miras HN, Long DL, Georgiev VP, Asenov A, Pedersen RH, Gadegaard N, Mirza MM, Paul DJ, Poblet JM, Cronin L. Design and fabrication of memory devices based on nanoscale polyoxometalate clusters. Nature 2014;515:545.

[44] Fei Z, Rodin AS, Andreev GO, Bao W, McLeod AS, Wagner M, Zhang LM, Zhao Z, Thiemens M, Dominguez G, Fogler MM, Castro Neto AH, Lau CN, Keilmann F, Basov DN. Gate-tuning of graphene plasmons revealed by infrared nano-imaging. Nature 2012;487:82.

[45] Chen JN, Badioli M, Alonso-Gonzalez P, Thongrattanasiri S, Huth F, Osmond J, Spasenovic M, Centeno A, Pesquera A, Godignon P, Elorza AZ, Camara N, de Abajo FJG, Hillenbrand R, Koppens FHL. Optical nano-imaging of gate-tunable graphene plasmons. Nature 2012;487:77.

[46] Bai HX, Liu XH, Zhang YC. Synthesis of MoO_3 nanoplates from a metallorganic molecular precursor. Mater. Lett. 2009;63:100.

[47] Liu JJ, Sasidharan M, Liu DA, Yokoyama Y, Yusa S, Nakashima K. Novel MoO_3 and WO_3 hollow nanospheres assembled with polymeric micelles. Mater. Lett. 2012;66:25.

[48] Meduri P, Clark E, Kim JH, Dayalan E, Sumanasekera GU, Sunkara MK. MoO_{3-x} nanowire arrays as stable and high-capacity anodes for lithium ion batteries. Nano Lett. 2012;12:1784.

[49] Du K, Fu WY, Wei RH, Yang HB, Xu J, Chang LX, Yu QJ, Zou GT. Ultrasonic-assisted synthesis of highly dispersed MoO_3 nanospheres using 3-mercaptopropyltrimethoxysilane. Ultrason. Sonochem. 2008;15:233.

[50] Hu S, Wang X. Single-walled MoO_3 nanotubes. J. Am. Chem. Soc. 2008;130:8126.

[51] Zhou JB, Lin N, Wang LB, Zhang KL, Zhu YC, Qian YT. Synthesis of hexagonal MoO_3 nanorods and a study of their electrochemical performance as anode materials for lithium-ion batteries. J. Mater. Chem. A 2015;3:7463.

[52] Chen JS, Cheah YL, Madhavi S, Lou XW. Fast Synthesis of alpha-MoO_3 nanorods with controlled aspect ratios and their enhanced lithium storage capabilities. J. Phys. Chem. C 2010;114:8675.

[53] Lou XW, Zeng HC. Hydrothermal synthesis of alpha-MoO_3 nanorods via acidification of ammonium heptamolybdate tetrahydrate. Chem. Mat. 2002;14:4781.

[54] Wang Q, Wang Q, Zhang DA, Sun J, Xing LL, Xue XY. Core-shell alpha-Fe_2O_3@alpha-MoO_3 nanorods as lithium-ion battery anodes with extremely high capacity and cyclability. Chem.-Asian J. 2014;9:3299.

[55] Xing LL, Yuan SA, Chen ZH, Chen YJ, Xue XY. Enhanced gas sensing performance of SnO_2/alpha-MoO_3 heterostructure nanobelts. Nanotechnology 2011;22:6.

[56] Mitra S, Sridharan K, Unnam J, Ghosh K. Synthesis of nanometal oxides and nanometals using hot-wire and thermal CVD. Thin Solid Films 2008;516:798.

[57] Diaz-Droguett DE, Fuenzalida VM, Diaz-Espinoza MS, Solorzano G. Electron beam effects on amorphous molybdenum oxide nanostructures grown by condensation in hydrogen. J. Mater. Sci. 2008;43:591.

[58] Allen P, Cai LL, Zhou LT, Zhao CQ, Rao PM. Rapid synthesis of thin and long $Mo_{17}O_{47}$ nanowire-arrays in an oxygen deficient flame. Sci Rep 2016;6:11.

[59] Stetter JR, Penrose WR, Yao S. Sensors, chemical sensors, electrochemical sensors, and ECS. J. Electrochem. Soc. 2003;150:S11.

[60] Sukharev VY, Myasnikov IA. Theoretical principles of the semiconductor sensor method in an analysis of active gases .2. adsorption effect on electroconductivity of baked polycrystalline adsorbents. Zhurnal Fiz. Khimii 1987;61:302.

[61] Sukharev VY, Myasnikov IA. Theoretical principles of the semiconductor sensor method in the active gas-analysis .1. physical principles of semiconductor adsorbent utilization as detectors. Zhurnal Fiz. Khimii 1986;60:2385.

[62] Gaman VI. Physical principles of operation of oxidizing gas sensors based on metal oxide semiconductors. Russ. Phys. J. 2012;54:1364.

[63] Grossmann K, Weimar U, Barsan N. Semiconducting metal oxides based gas sensors. In: Svensson BG, Pearton SJ, Jagadish C, editors. Oxide Semiconductors, vol. 88. San Diego: Elsevier Academic Press Inc, 2013. p.261.

[64] Rebholz J, Bonanati P, Weimar U, Barsan N. Grain shape influence on semiconducting metal oxide based gas sensor performance: modeling versus experiment. Anal. Bioanal. Chem. 2014;406:3977.

[65] Kanan SM, El-Kadri OM, Abu-Yousef IA, Kanan MC. Semiconducting metal oxide based sensors for selective gas pollutant detection. Sensors 2009;9:8158.

[66] Huang J, Wan Q. Gas sensors based on semiconducting metal oxide one-dimensional nanostructures. Sensors 2009;9:9903.

[67] Zhang G, Liu ML. Effect of particle size and dopant on properties of SnO_2-based gas sensors. Sens. Actuator B-Chem. 2000;69:144.

[68] Korotcenkov G. Metal oxides for solid-state gas sensors: What determines our choice? Mater. Sci. Eng. B-Solid State Mater. Adv. Technol. 2007;139:1.

[69] Wang CX, Yin LW, Zhang LY, Xiang D, Gao R. Metal oxide gas sensors: sensitivity and influencing factors. Sensors 2010;10:2088.

[70] Yamazaki T, Jin CJ, Nakayama A, Ito K, Yoshizawa T, Kikuta T, Nakatani N, Yamabuchi T. NO_2 gas sensor made of porous MoO_3 sputtered films. Jpn. J. Appl. Phys. Part 1 - Regul. Pap. Brief Commun. Rev. Pap. 2005;44:792.

[71] Barsan N, Weimar U. Conduction model of metal oxide gas sensors. J. Electroceram. 2001;7:143.

[72] Li H, Ngan AHW. Indentation size effects on the strain rate sensitivity of nanocrystalline Ni-25at.%Al thin films. Scr. Mater. 2005;52:827.

[73] Alsaif MM, Chrimes AF, Daeneke T, Balendhran S, Bellisario DO, Son Y, Field MR, Zhang W, Nili H, Nguyen EP. High-performance field effect transistors using electronic inks of 2d molybdenum oxide nanoflakes. Adv. Funct. Mater. 2016;26:91.

[74] Alsaif MM, Latham K, Field MR, Yao DD, Medehkar NV, Beane GA, Kaner RB, Russo SP, Ou JZ, Kalantar‐zadeh K. Tunable plasmon resonances in two‐dimensional molybdenum oxide nanoflakes. Advanced Materials 2014;26:3931.

[75] Alsaif MM, Balendhran S, Field MR, Latham K, Wlodarski W, Ou JZ, Kalantar-zadeh K. Two dimensional α-MoO_3 nanoflakes obtained using solvent-assisted grinding and sonication method: Application for H_2 gas sensing. Sensors and Actuators B: Chemical 2014;192:196.

[76] Wang L, Gao P, Bao D, Wang Y, Chen Y, Chang C, Li G, Yang P. Synthesis of crystalline/amorphous core/shell MoO_3 composites through a controlled dehydration route and their enhanced ethanol sensing properties. Cryst. Growth Des. 2014;14:569.

[77] Battaglia C, Yin X, Zheng M, Sharp ID, Chen T, McDonnell S, Azcatl A, Carraro C, Ma B, Maboudian R. Hole selective MoOx contact for silicon solar cells. Nano Lett. 2014;14:967.

[78] Greiner MT, Chai L, Helander MG, Tang WM, Lu ZH. Transition metal oxide work functions: the influence of cation oxidation state and oxygen vacancies. Adv. Funct. Mater. 2012;22:4557.

[79] Xie W, Su M, Zheng Z, Wang Y, Gong L, Xie F, Zhang W, Luo Z, Luo J, Liu P. Nanoscale insights into the hydrogenation process of layered α-MoO_3. ACS Nano 2015;10:1662.

[80] Wei Q, Cheng S, Ramesh KT, Ma E. Effect of nanocrystalline and ultrafine grain sizes on the strain rate sensitivity and activation volume: fcc versus bcc metals. Mater. Sci. Eng. A-Struct. Mater. Prop. Microstruct. Process. 2004;381:71.

[81] Rothschild A, Komem Y. The effect of grain size on the sensitivity of nanocrystalline metal-oxide gas sensors. J. Appl. Phys. 2004;95:6374.

[82] Arafat MM, Dinan B, Akbar SA, Haseeb A. Gas sensors based on one dimensional nanostructured metal-oxides: A Review. Sensors 2012;12:7207.

[83] Ji FX, Ren XP, Zheng XY, Liu YC, Pang LQ, Jiang JX, Liu SZ. 2D-MoO_3 nanosheets for superior gas sensors. Nanoscale 2016;8:8696.

[84] Firooz AA, Mahjoub AR, Khodadadi AA. Fabrication and highly sensitive gas sensors based on h-MoO_3/SnO_2 hollow nanostructures operated at low temperatures. J. Nanosci. Nanotechnol. 2010;10:6155.

[85] Kim WS, Kim HC, Hong SH. Gas sensing properties of MoO_3 nanoparticles synthesized by solvothermal method. J. Nanopart. Res. 2010;12:1889.

[86] Jiang DS, Wei W, Li F, Li YJ, Liu CX, Sun DM, Feng CH, Ruan SP. Xylene gas sensor based on alpha-MoO_3/alpha-Fe_2O_3 heterostructure with high response and low operating temperature. RSC Adv. 2015;5:39442.

[87] Galatsis K, Li YX, Wlodarski W, Kalantar-zadeh K. Sol-gel prepared MoO_3-WO_3 thin-films for O_2 gas sensing. Sens. Actuator B-Chem. 2001;77:478.

[88] Rahmani MB, Keshmiri SH, Yu J, Sadek AZ, Al-Mashat L, Moafi A, Latham K, Li YX, Wlodarski W, Kalantar-zadeh K. Gas sensing properties of thermally evaporated lamellar MoO_3. Sens. Actuator B-Chem. 2010;145:13.

[89] Liu YL, Yang S, Lu Y, Podval'naya NV, Chen W, Zakharova GS. Hydrothermal synthesis of h-MoO_3 microrods and their gas sensing properties to ethanol. Appl. Surf. Sci. 2015;359:114.

[90] Li Y, Yang Q, Yu X, Trinchi A, Sadek A, Wlodarski W, Kalantar-Zadeh K. Nanostructured molybdenum oxide gas sensors. 2006 5th IEEE Conference on Sensors: IEEE, 2006. p.232.

[91] Bai SL, Chen S, Chen LY, Zhang KW, Luo RX, Li DQ, Liu CC. Ultrasonic synthesis of MoO_3 nanorods and their gas sensing properties. Sens. Actuator B-Chem. 2012;174:51.

[92] Hosono K, Matsubara I, Murayama N, Woosuck S, Izu N. Synthesis of polypyrrole/MoO_3 hybrid thin films and their volatile organic compound gas-sensing properties. Chem. Mat. 2005;17:349.

[93] Illyaskutty N, Sreedhar S, Kumar GS, Kohler H, Schwotzer M, Natzeck C, Pillai VPM. Alteration of architecture of MoO_3 nanostructures on arbitrary substrates: growth kinetics, spectroscopic and gas sensing properties. Nanoscale 2014;6:13882.

[94] Muraoka Y, Grenier JC, Petit S, Pouchard M. Preparation of hexagonal MoO_3 by "Chimie Douce" reaction with NO_2. Solid State Sci. 1999;1:133.

[95] Ferroni M, Guidi V, Martinelli G, Sacerdoti M, Nelli P, Sberveglieri G. MoO_3-based sputtered thin films for fast NO_2 detection. Sens. Actuator B-Chem. 1998;48:285.

[96] Barazzouk S, Tandon RP, Hotchandani S. MoO_3-based sensor for NO, NO_2 and CH_4 detection. Sens. Actuator B-Chem. 2006;119:691.

[97] Zhu J, Gao F, Dong LH, Yu WJ, Qi L, Wang Z, Dong L, Chen Y. Studies on surface structure of $M_xO_y/MoO_3/CeO_2$ system (M = Ni, Cu, Fe) and its influence on SCR of NO by NH_3. Appl. Catal. B-Environ. 2010;95:144.

[98] Yan ZF, Zuo ZJ, Lv XY, Li Z, Li Z, Huang W. Adsorption of NO on MoO_3 (0 1 0) surface with different location of terminal oxygen vacancy defects: A density functional theory study. Appl. Surf. Sci. 2012;258:3163.

[99] Wang XP, Yu SS, Yang HL, Zhang SX. Selective catalytic reduction of NO by C_2H_2 over MoO_3/HZSM-5. Appl. Catal. B-Environ. 2007;71:246.

[100] Koh HL, Park HK. Characterization of MoO_3-V_2O_5/Al_2O_3 catalysts for selective catalytic reduction of NO by NH3. J. Ind. Eng. Chem. 2013;19:73.

[101] Novoselova LY. Mo and MoO_3 powders: Structure and resistance to CO. J. Alloy. Compd. 2014;615:784.

[102] Bian ZC, Meng X, Tao M, Lv YH, Xin Z. Effect of MoO_3 on catalytic performance and stability of the SBA-16 supported Ni-catalyst for CO methanation. Fuel 2016;179:193.

[103] Bai SL, Chen C, Tian Y, Chen S, Luo RX, Li DQ, Chen AF, Liu CC. Facile synthesis of alpha-MoO_3 nanorods with high sensitivity to CO and intrinsic sensing performance. Mater. Res. Bull. 2015;64:252.

[104] Zhang J, Song P, Li ZQ, Zhang S, Yang ZX, Wang Q. Enhanced trimethylamine sensing performance of single-crystal MoO_3 nanobelts decorated with Au nanoparticles. J. Alloy. Compd. 2016;685:1024.

[105] Yang S, Liu YL, Chen W, Jin W, Zhou J, Zhang H, Zakharova GS. High sensitivity and good selectivity of ultralong MoO_3 nanobelts for trimethylamine gas. Sens. Actuator B-Chem. 2016;226:478.

[106] Deekshitha M, Nagarajan V, Chandiramouli R. First-principles studies on transport property and adsorption characteristics of trimethylamine on alpha-MoO_3 molecular device. Chem. Phys. Lett. 2015;641:129.

[107] Chu XF, Liang SM, Sun WQ, Zhang WB, Chen TY, Zhang QF. Trimethylamine sensing properties of sensors based on MoO_3 microrods. Sens. Actuator B-Chem. 2010;148:399.

[108] Cho YH, Ko YN, Kang YC, Kim ID, Lee JH. Ultraselective and ultrasensitive detection of trimethylamine using MoO_3 nanoplates prepared by ultrasonic spray pyrolysis. Sens. Actuator B-Chem. 2014;195:189.

[109] Xia YC, Wu CS, Zhao NY, Zhang H. Spongy MoO_3 hierarchical nanostructures for excellent performance ethanol sensor. Mater. Lett. 2016;171:117.

[110] Wang LQ, Gao P, Bao D, Wang Y, Chen YJ, Chang C, Li GB, Yang PP. Synthesis of crystalline/amorphous core/shell MoO_3 composites through a controlled dehydration route and their enhanced ethanol sensing properties. Cryst. Growth Des. 2014;14:569.

[111] Li ZC, Li Y, Zhan ES, Ta N, Shen WJ. Morphology-controlled synthesis of alpha-MoO_3 nanomaterials for ethanol oxidation. J. Mater. Chem. A 2013;1:15370.

[112] Illyaskutty N, Kohler H, Trautmann T, Schwotzer M, Pillai VPM. Enhanced ethanol sensing response from nanostructured MoO_3:ZnO thin films and their mechanism of sensing. J. Mater. Chem. C 2013;1:3976.

[113] Chen YJ, Meng FN, Ma C, Yang ZW, Zhu CL, Ouyang QY, Gao P, Li JQ, Sun CW. In situ diffusion growth of $Fe_2(MoO_4)_3$ nanocrystals on the surface of alpha-MoO_3 nanorods with significantly enhanced ethanol sensing properties. J. Mater. Chem. 2012;22:12900.

[114] Chen YJ, Meng FN, Ma C, Yang W, Zhu CL, Ouyang QY, Gao P, Li JQ, Sun CW. In situ diffusion growth of $Fe_2(MoO_4)_3$ nanocrystals on the surface of alpha-MoO_3

nanorods with significantly enhanced ethanol sensing properties (vol 22, pg 12900, 2012). J. Mater. Chem. 2012;22:25495.

[115] Chen DL, Liu MN, Yin L, Li T, Yang Z, Li XJ, Fan BB, Wang HL, Zhang R, Li ZX, Xu HL, Lu HX, Yang DY, Sun J, Gao L. Single-crystalline MoO_3 nanoplates: topochemical synthesis and enhanced ethanol-sensing performance. J. Mater. Chem. 2011;21:9332.

[116] Martins RL, Baldanza MAS, Souza M, Schmal M. The effect of support on methane activation over Pt catalysts in the presence of MoO_3. Appl. Catal. A-Gen. 2007;318:207.

[117] Burns S, Hargreaves JSJ, Pal P, Parida KM, Parija S. The effect of dopants on the activity Of MoO_3/ZSM-5 catalysts for the dehydroaromatisation of methane. Catal. Today 2006;114:383.

[118] Phuong PTT, Duy NPH, Tai VT, Huan NM, Phuc NHH, Loc LC. Facile synthesis of a green metastable MoO_3 for the selective oxidation of methanol to formaldehyde. React. Kinet. Mech. Catal. 2016;117:161.

[119] Pham TTP, Nguyen PHD, Vo TT, Nguyen HHP, Luu CL. Facile method for synthesis of nanosized beta-MoO_3 and their catalytic behavior for selective oxidation of methanol to formaldehyde. Adv. Nat. Sci.-Nanosci Nanotechnol 2015;6:6.

[120] Babichev IV, Il'in AA, Rumyantsev RN, Nikonorova NE, Il'in AP. Recovery of MoO_3 from spent catalysts of partial oxidation of methanol to formaldehyde. Russ. J. Appl. Chem. 2014;87:265.

[121] Matyshak VA, Kadushin AA, Burkhardt JS, Schnabel KH. Spectrokinetic study of the oxidation of ammonia on MoO_3. Kinet. Catal. 1985;26:286.

[122] Kasaoka S, Yamanaka T. Effect of supports and additions (metal-oxides) on iron(iii) sulfate catalysts for reduction of nitrogen-oxide with ammonia - selection of coprecipitated $Fe_2(SO_4)_3$-alpha-Fe_2O_3-TiO_2-MoO_3 (or WO_3) catalysts. Nippon Kagaku Kaishi 1977:907.

[123] Giordano N, Bart JCJ, Castellarin A, Ragaini V. Oxidation of ammonia over Bi_2O_3 single-bond MoO_3 Systems. React. Kinet. Catal. Lett. 1974;1:405.

[124] Datta AK, Ha JW, Regalbuto JR. The controlled dispersion of silica supported MoO_3 - the role of ammonia. J. Catal. 1992;133:55.

[125] Biermann JJP, Janssen F, Deboer M, Vandillen AJ, Geus JW, Vogt ETC. Molybdena on silica catalysts - selective catalytic-oxidation of ammonia to nitrogen over MoO_3 on SiO_2 catalysts. Journal of Molecular Catalysis 1990;60:229.

[126] Belokopytov YV, Kholyavenko KM, Gerei SV. Infrared study of the surface-properties of metal-oxides .2. interaction of ammonia with the surface of Fe_2O_3, ZnO, MoO_3, and V_2O_5. J. Catal. 1979;60:1.

[127] Alsdorf E, Hanke W, Schnabel KH, Schreier E. Infrared studies on the interaction of ammonia and water on MoO_3/SiO_2 catalysts. J. Catal. 1986;98:82.

[128] Kim JG, Regalbuto JR. The effect of calcination on H_2 spillover in Pt/MoO_3 .2. kinetic modeling. J. Catal. 1993;139:175.

[129] Mukund R, Kelly TJ, Spicer CW. Source attribution of ambient air toxic and other VOCs in Columbus, Ohio. Atmos. Environ. 1996;30:3457.

[130] Oliver KD, Adams JR, Daughtrey EH, McClenny WA, Yoong MJ, Pardee MA, Almasi EB, Kirshen NA. Technique for monitoring toxic VOCs in air: Sorbent preconcentration, closed-cycle cooler cryofocusing and GC/MS analysis. Environ. Sci. Technol. 1996;30:1939.

[131] Sui LL, Xu YM, Zhang XF, Cheng XL, Gao S, Zhao H, Cai Z, Huo LH. Construction of three-dimensional flower-like alpha-MoO_3 with hierarchical structure for highly selective triethylamine sensor. Sens. Actuator B-Chem. 2015;208:406.

[132] Zeng W, Zhang H, Li YQ, Chen WG. Net-like MoO_3 porous architectures: synthesis and their sensing properties. J. Mater. Sci.-Mater. Electron. 2014;25:338.

[133] Kamat PV. Meeting the clean energy demand: Nanostructure architectures for solar energy conversion. J. Phys. Chem. C 2007;111:2834.

[134] Green MA. The path to 25% silicon solar cell efficiency: History of silicon cell evolution. Progress in Photovoltaics: Research and Applications 2009;17:183.

[135] Green MA. Silicon photovoltaic modules: a brief history of the first 50 years. Progress in Photovoltaics: Research and applications 2005;13:447.

[136] Spanggaard H, Krebs FC. A brief history of the development of organic and polymeric photovoltaics. Sol. Energy Mater. Sol. Cells 2004;83:125.

[137] Juster NJ. Organic semiconductors. J. Chem. Educ 1963;40:547.

[138] You J, Dou L, Yoshimura K, Kato T, Ohya K, Moriarty T, Emery K, Chen C-C, Gao J, Li G. A polymer tandem solar cell with 10.6% power conversion efficiency. Nature communications 2013;4:1446.

[139] Ludwig GW, Watters RL. Drift and conductivity mobility in silicon. Physical Review 1956;101:1699.

[140] Reggiani S, Valdinoci M, Colalongo L, Rudan M, Baccarani G, Stricker AD, Illien F, Felber N, Fichtner W, Zullino L. Electron and hole mobility in silicon at large operating temperatures - Part I: Bulk mobility. IEEE Trans. Electron Devices 2002;49:490.

[141] Hoppe H, Sariciftci NS. Organic solar cells: An overview. J. Mater. Res. 2004;19:1924.

[142] Ramsdale C, Barker J, Arias A, MacKenzie J, Friend RH, Greenham N. The origin of the open-circuit voltage in polyfluorene-based photovoltaic devices. J. Appl. Phys. 2002;92:4266.

[143] Kaltenbrunner M, White MS, Głowacki ED, Sekitani T, Someya T, Sariciftci NS, Bauer S. Ultrathin and lightweight organic solar cells with high flexibility. Nature communications 2012;3:770.

[144] Scharber MC, Mühlbacher D, Koppe M, Denk P, Waldauf C, Heeger AJ, Brabec CJ. Design rules for donors in bulk‐heterojunction solar cells—Towards 10% energy‐conversion efficiency. Advanced materials 2006;18:789.

[145] Günes S, Neugebauer H, Sariciftci NS. Conjugated polymer-based organic solar cells. Chemical reviews 2007;107:1324.

[146] Cheng Y-J, Yang S-H, Hsu C-S. Synthesis of conjugated polymers for organic solar cell applications. Chemical reviews 2009;109:5868.

[147] Clarke TM, Durrant JR. Charge Photogeneration in Organic Solar Cells. Chemical Reviews 2010;110:6736.

[148] Kim JY, Lee K, Coates NE, Moses D, Nguyen T-Q, Dante M, Heeger AJ. Efficient tandem polymer solar cells fabricated by all-solution processing. Science 2007;317:222.

[149] Tress W, Leo K, Riede M. Influence of hole‐transport layers and donor materials on open‐circuit voltage and shape of i–v curves of organic solar cells. Adv. Funct. Mater. 2011;21:2140.

[150] Hoppea H, Sariciftci NS. Organic solar cells: An overview. J. Mater. Res 2004;19:1925.

[151] Zhou HQ, Zhang Y, Mai CK, Collins SD, Nguyen TQ, Bazan GC, Heeger AJ. Conductive conjugated polyelectrolyte as hole-transporting layer for organic bulk heterojunction solar cells. Advanced Materials 2014;26:780.

[152] Lei HW, Fang GJ, Cheng F, Ke WJ, Qin PL, Song ZC, Zheng Q, Fan X, Huang HH, Zhao XZ. Enhanced efficiency in organic solar cells via in situ fabricated p-type copper sulfide as the hole transporting layer. Sol. Energy Mater. Sol. Cells 2014;128:77.

[153] Gupta D, Wienk MM, Janssen RAJ. Efficient polymer solar cells on opaque substrates with a laminated pedot:pss top electrode. Adv. Energy Mater. 2013;3:782.

[154] Steirer KX, Chesin JP, Widjonarko NE, Berry JJ, Miedaner A, Ginley DS, Olson DC. Solution deposited NiO thin-films as hole transport layers in organic photovoltaics. Org. Electron. 2010;11:1414.

[155] Lattante S. Electron and hole transport layers: their use in inverted bulk heterojunction polymer solar cells. Electronics 2014;3:132.

[156] Greiner MT, Helander MG, Tang WM, Wang ZB, Qiu J, Lu ZH. Universal energy-level alignment of molecules on metal oxides. Nat. Mater. 2012;11:76.

[157] Ley L, Smets Y, Pakes CI, Ristein J. Calculating the universal energy-level alignment of organic molecules on metal oxides. Adv. Funct. Mater. 2013;23:794.

[158] Tan Za, Li L, Cui C, Ding Y, Xu Q, Li S, Qian D, Li Y. Solution-processed tungsten oxide as an effective anode buffer layer for high-performance polymer solar cells. The Journal of Physical Chemistry C 2012;116:18626.

[159] Nirupama V, Chandrasekhar M, Radhika P, Sreedhar B, Uthanna S. Characterization of molybdenum oxide films prepared by bias magnetron sputtering. Journal of optoelectronics and advanced materials 2009;11:320.

[160] Fan X, Fang G, Qin P, Sun N, Liu N, Zheng Q, Cheng F, Yuan L, Zhao X. Deposition temperature effect of RF magnetron sputtered molybdenum oxide films on the power conversion efficiency of bulk-heterojunction solar cells. Journal of Physics D: Applied Physics 2011;44:045101.

[161] Larsen JK, Simchi H, Xin P, Kim K, Shafarman W. Backwall superstrate configuration for ultrathin Cu(In,Ga)Se_2 solar cells. Appl. Phys. Lett. 2014;104:033901.

[162] Simchi H, McCandless BE, Meng T, Shafarman WN. Structure and interface chemistry of MoO_3 back contacts in Cu (In, Ga) Se_2 thin film solar cells. J. Appl. Phys. 2014;115:033514.

[163] Shrotriya V, Li G, Yao Y, Chu C-W, Yang Y. Transition metal oxides as the buffer layer for polymer photovoltaic cells. Appl. Phys. Lett. 2006;88:073508.

[164] Sun Y, Takacs CJ, Cowan SR, Seo JH, Gong X, Roy A, Heeger AJ. Efficient, air - stable bulk heterojunction polymer solar cells using MoO_x as the anode interfacial layer. Advanced materials 2011;23:2226.

[165] Meyer J, Shu A, Kro¨ ger M, Kahn A. Effect of contamination on the electronic structure and hole-injection properties of MoO_3/organic semiconductor interfaces. Appl. Phys. Lett. 2010;96:133308.

[166] Greiner MT, Lu Z-H. Thin-film metal oxides in organic semiconductor devices: their electronic structures, work functions and interfaces. NPG Asia Materials 2013;5:e55.

[167] Qiu W, Müller R, Voroshazi E, Conings B, Carleer R, Boyen H-G, Turbiez M, Froyen L, Heremans P, Hadipour A. Nafion-modified MoO_x as effective room-temperature hole injection layer for stable, high-performance inverted organic solar cells. ACS applied materials & interfaces 2015;7:3581.

[168] Zilberberg K, Gharbi H, Behrendt A, Trost S, Riedl T. Low-temperature, solution-processed MoO_x for efficient and stable organic solar cells. ACS applied materials & interfaces 2012;4:1164.

[169] Litzov I, Brabec CJ. Development of efficient and stable inverted bulk heterojunction (BHJ) solar cells using different metal oxide interfaces. Materials 2013;6:5796.

[170] Girotto C, Voroshazi E, Cheyns D, Heremans P, Rand BP. Solution-processed MoO_3 thin films as a hole-injection layer for organic solar cells. ACS applied materials & interfaces 2011;3:3244.

[171] Murase S, Yang Y. Solution processed MoO_3 interfacial layer for organic photovoltaics prepared by a facile synthesis method. Advanced Materials 2012;24:2459.

[172] Wang Y, Luo Q, Wu N, Wang Q, Zhu H, Chen L, Li Y-Q, Luo L, Ma C-Q. Solution-processed MoO_3: PEDOT: PSS hybrid hole transporting layer for inverted polymer solar cells. ACS applied materials & interfaces 2015;7:7170.

[173] Li X, Choy WC, Xie F, Zhang S, Hou J. Room-temperature solution-processed molybdenum oxide as a hole transport layer with Ag nanoparticles for highly efficient inverted organic solar cells. J. Mater. Chem. A 2013;1:6614.

[174] Qiu W, Hadipour A, Müller R, Conings B, Boyen H-G, Heremans P, Froyen L. Ultrathin ammonium heptamolybdate films as efficient room-temperature hole transport layers for organic solar cells. ACS applied materials & interfaces 2014;6:16335.

[175] Vallejos S, Stoycheva T, Umek P, Navio C, Snyders R, Bittencourt C, Llobet E, Blackman C, Moniz S, Correig X. Au nanoparticle-functionalised WO_3 nanoneedles and their application in high sensitivity gas sensor devices. Chemical Communications 2011;47:565.

[176] Yao K, Toole R, Basnet P, Zhao Y. Highly sensitive double-layered nanorod array gas sensors prepared by oblique angle deposition. Appl. Phys. Lett. 2014;104:073110.

[177] Tian S, Yang F, Zeng D, Xie C. Solution-processed gas sensors based on ZnO nanorods array with an exposed (0001) facet for enhanced gas-sensing properties. The Journal of Physical Chemistry C 2012;116:10586.

Chapter 2

Growth of molybdenum trioxide nanorod arrays via one-step solution process

Abstract

A simple sol-gel solution route for synthesis of α-MoO_3 nanorod arrays is investigated in terms of growth mechanism with controlling citric acid decomposition rate. The single-phase and single-crystal of nanorod arrays of MoO_3 grown in random directions from a silica glass substrate had mean diameters and lengths of 10 nm and 500 nm, respectively. The citric acid play a critical role for the nanorod arrays growth process from examination of the relative molar ratio of molybdate and citric acid in the precursor. Moreover, the dissociation timing of the citric acid, which were controlled by the other two synthesis parameters, i.e. annealing time and solvents, also greatly influence growth and phase transition of MoO_3 nanorod arrays by analyzing scanning electron microscopy (SEM) and X-ray diffraction (XRD). The optimizing synthesis parameters were expected to design with the nanorod arrays length and density. The longest nanorod arrays can be obtained up to 600 nm using a dimethylacetamide solvent, a molar ratio of Mo:citric acid = 0.5:1.5, and annealing at 400 ^{o}C for 15 min in ambient atmosphere. Findings of the present study describe that the factors of the nanorod arrays growth and phase changing are deeply correlated with disassemble steps of Mo metal-citric-acid complex in the sol-gel precursor solution, which will contribute to apply the material development in several electronic devices using MoO_3 nanostructures.

2.1 Introduction

In recent decades, tremendous achievements have been worldwidely obtained in the field of nanoscience and nanotechnology. However, synthesizing functional materials with controllable morphologies and a comparatively simple synthesis process is still difficult and of great significance in this field [1, 2]. In particular, finding novel synthesis routes for one-dimensional (1-D) nanostructured materials, including nanotubes, nanorods, nanospheres, nanoplates, nanoribbons, and nanobelts has been and will continue to be a hot subjects [3-7]. The reason for this is that their synthesis process is complex, but they have unique electronic, chemical, optical, and mechanical properties that are difficult to achieve in equivalent bulk materials [8-13]. Among them, nanorod arrays are some the most important morphologies because of their faster electronic transmission channels; they have been studied for a long time with respect to growing nanorod arrays with prolonged lengths along the axis or increased length-diameter ratios [14-16].

Recently, molybdenum trioxide (MoO_3), an indirect wide band-gap (3.5 eV) semiconductor material, has attracted much attention because of its special crystalline structure and the polyvalency attributes of molybdate [17]. Pure MoO_3 has three polymorphs, i.e., the orthorhombic phase (α-MoO_3), the monoclinic phase (β-MoO_3), and the hexagonal phase (h-MoO_3). The β-phase is metastable monoclinic and can be converted to the thermodynamically stable α-phase at high temperatures, near 673 K [18]. α-MoO_3 consists of a stable layer structure, as shown in the inset of Figure 2.1, with unit cell parameters a=3.9620 Å, b=13.86 Å, and c=3.70 Å. Moreover, corner-sharing chains of double layers of zigzag MoO_6 octahedra are hold together by covalent forces in the a- and c-axis directions, and by weak Van der Waals forces in the b-axis direction. During the synthesis process, the discrepancy of this weak Van der Waals force will limit the growth rate in the [010] direction, compared with the other two directions, which will result in anisotropic growth [19]. This unique feature makes it one of the most promising candidates to form a large surface area and high surface-to-volume ratio nanostructures [20-23]. In particular, MoO_3 nanorod arrays have been applied in field emission [22, 24], as anodes of lithium batteries [25-27], as buffer layer of organic light emitting diodes [28], and as gas sensors [20, 29], because of their high surface-to-volume ratio, superior crystallinity, and excellent electron transportation properties [30].

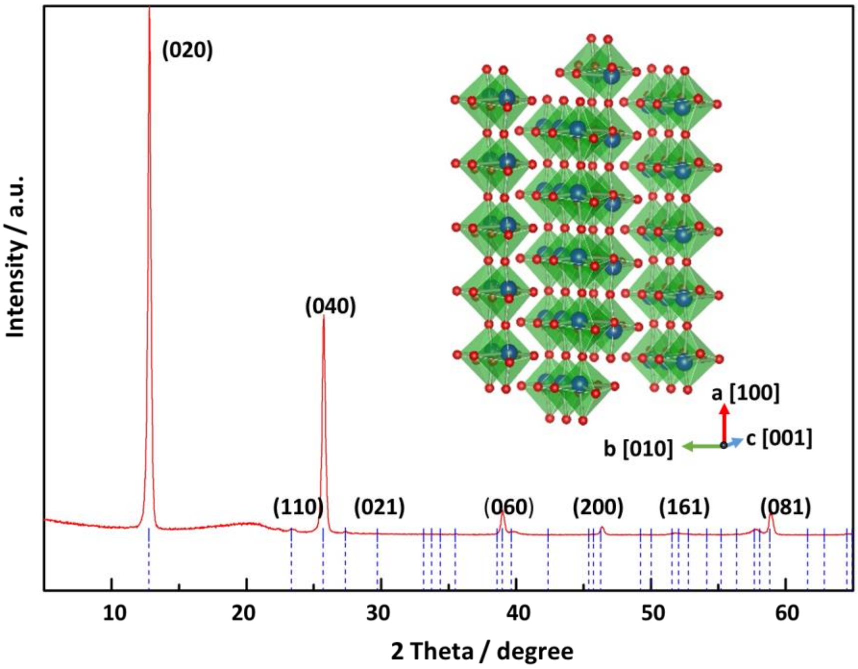

Figure 2.1 XRD pattern of MoO_3 nanorod arrays synthesized by 2-ME solvent, molybdate:citric acid = 0.5:1.5, spin coated at 1000 rpm for 10 s, annealing at 673 K for 15 min (inset, crystal structure of MoO_3).

In general, MoO_3 nanorod arrays can be synthesized by pulsed electron beam deposition [30], RF sputtering[31], thermal evaporation [31], and a hydrothermal method [32, 33]. However these methods are complicated because they involve high energy costs, as well as poor productivity and reproducibility. Developing a new synthesis method has become an urgent issue. Sol-gel method has many merits, such as being simple, homogeneous, applicable over a large area, performed in a short time, and easy to control with low energy costs; as such, it has been applied to prepare metal oxides, e.g., ZnO, TiO_2, and ITO, as well as other oxides [34, 35].

This work reports α-MoO_3 nanorod arrays grown randomly from silica glass substrates that exhibit a single-phase and single-crystal nature. The nanorod arrays were prepared by combining sol-gel, spin-coating, and annealing processes. The development of α-MoO_3 nanorod arrays from such routes is rarely reported. For this reason, the factors affecting the growth were studied in detail. The lengths of the nanorod arrays are prolonged by controlling these relative parameters for various electric devises.

2.2 Experimental

2.2.1 Synthesis process of α-MoO_3 nanorod arrays

To synthesize α-MoO_3 nanorod arrays, ammonium molybdate ($H_8N_2O_4Mo$, (0.5 M), Wako, 97.0 %, Osaka, Japan) and citric acid ($C_6H_8O_7$, 1.5 M, Wako, Anhydrous, 98.0 %, Osaka, Japan), were dissolved in 2-methoxyethanol (2-ME, $C_3H_8O_2$ (5 ml), Wako, 99.0%, boiling point 125 ^oC, Osaka, Japan) as a solvent at room temperature with magnetic stirring. After 4 h, the solution changed into a blue transparent sol-solution, which was aged at room temperature for 24 h to form a homogeneous sol-gel precursor. After aging, the precursors appeared yellow in a dark environment. When they were exposed to light for several minutes, the color changed from yellow to blue. After the color changed, the precursor (300 μl) was spin coated at 1000 rpm for 10 s (MIKASA SPINCOATER 1H-DX2, Tokyo, Japan) on a silica glass substrate cleaned by N_2 plasma for 1 min with a spin coater. Finally, the film was annealed at 400 ^oC in a preheated furnace for 15 min (DENKEN KDF-P90, Kyoto, Japan) to obtain thin film samples. The synthesis process was schematically depicted in Figure 2.2.

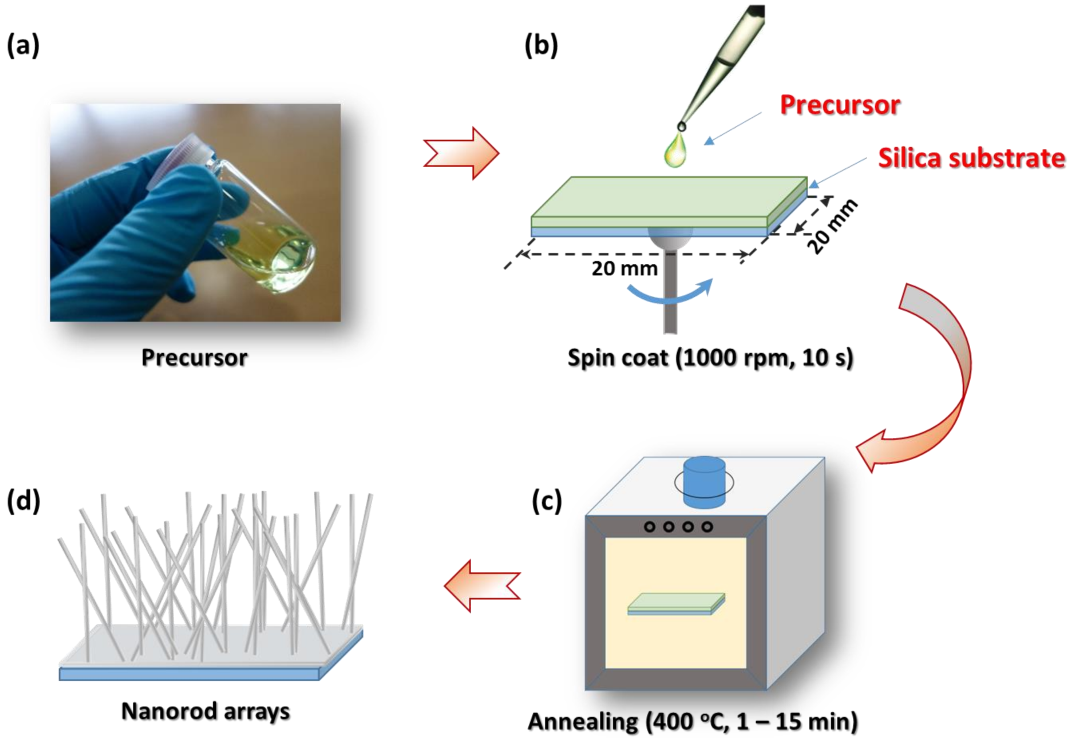

Figure 2.2 Schematic of synthesis process of nanorod arrays.

2.2.2 Characterization methods of α-MoO_3 nanorod arrays

The crystal structure, chemical composition, and physical properties of the thin film were investigated. The X-ray diffraction (XRD) patterns of the thin films were collected in the range of 2θ = 5–65° using an X-ray diffractometer (Rigaku SmartLab, Akishima, Tokyo, Japan) with CuKa radiation at 45 kV and 100 mA, using a step size of 0.02°, scanning rate of 4°/min, and incidence angle, ω, of 0.2°. FT-IR spectra were collected by Fourier transform infrared spectrometer (FTIR: JASCO FT/IR6100, Tokyo, Japan). Top and cross-sectional views of the morphology of these samples were observed by field-emission scanning electron microscopy (FE-SEM: Hitachi SU8020, Tokyo, Japan) at 5 kV and 10 mA. Before observation, the thin films were sputtered with Pt to reduce charging and obtain clear images. The crystal structure of single MoO_3 nanorod was examined by high-resolution transmission electron microscopy analysis

(HR-TEM: JEOL-EM-3000F, Tokyo, Japan) at 300 kV. Thermogravimetric and differential thermal analysis (TG/DTA, TG-DTA 2000SE/H/21/1, NETZSCH, Bavaria, Germany) was performed to elucidate the crystallization process of the MoO_3 nanorod arrays. The TG/DTA analysis was carried out at a heating rate of 5 ^{o}C/min between 50 and 800 ^{o}C in air.

2.3 Results and discussion

2.3.1 Synthesis and characterization of α-MoO_3 nanorod arrays

Figure 2.1 shows the XRD pattern of the products synthesized *via* sol-gel annealing treatment. The vertical dashed lines at the bottom of Figure 1 display the ideal patterns of α-MoO_3 from JCPDs No. 05-0508. The XRD patterns of the sample fit well with the data of the ideal patterns of orthorhombic α-MoO_3. The strong (020), (040), and (060) peaks revealed a highly crystalline anisotropic growth, almost the same as the reported XRD pattern [26, 36, 37]. Moreover, FT-IR spectroscopy of the sample was evaluated to obtain more structural information.

Figure 2.3 presents the FT-IR spectra of the as-synthesized MoO_3 nanorod arrays in the range of 400–1200 cm^{-1}. The absorption region around 600 cm^{-1} is a typical vibration of the Mo_2O_2 entity created by edge-shared MoO_6 octahedra forming the orthorhombic α-MoO_3 structure [38, 39]. The band at 990 cm^{-1} is characteristic of the vibration of the Mo=O terminal bond, which can be observed in the layered alpha-MoO_3 structure, as shown in the inset of Figure 1. A. Stoyanova *et al.* [40] and N. A. Chernova *et al.* [41] mentioned that the Mo=O terminal bond were inexistence in β-MoO_3 in the literature. The dominant band at 860 cm^{-1} is associated with the Mo-O-Mo bridging bonds. These results of XRD and FT-IR reveal that the sample shows almost a single-phase α-MoO_3 structure.

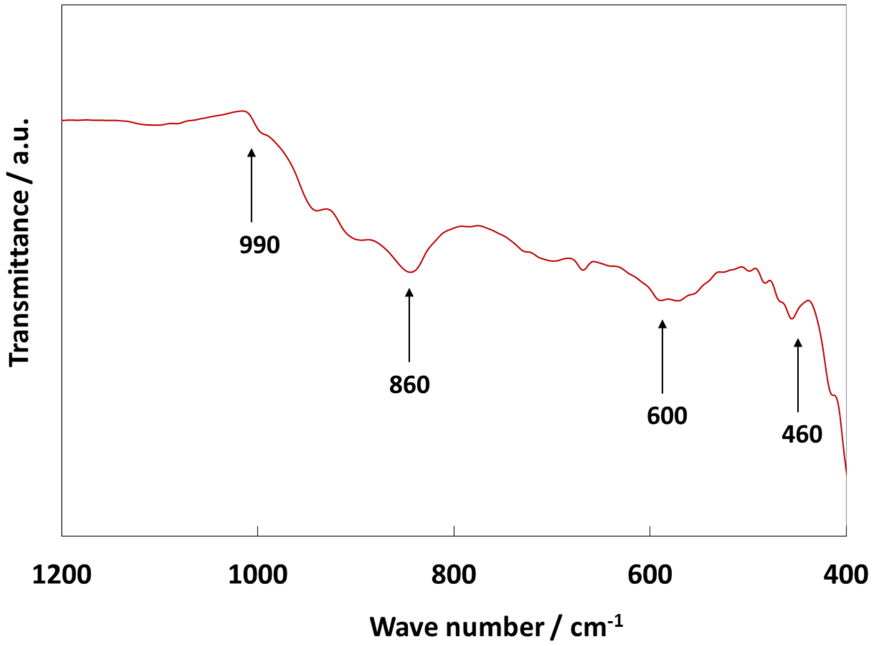

Figure 2.3 FT-IR spectra of as-synthesized MoO_3 nanorod arrays (2-ME, 0.5:1.5, 1000 rpm/10 s, 673 K/15 min).

Figure 2.4 shows FE-SEM and TEM images of the as-obtained α-MoO_3 sample, which was grown on a silica glass substrate by annealing at 400 °C for only 15 min. The top-view SEM image of the sample in Figure 2.4 (a) shows that many needle-like nanorod arrays were grown from the substrate with straight or curved shapes. The cross-sectional view of the nanorod arrays in Figure 2.4 (b) gives detailed information about the morphology of the nanorod arrays. The nanorod arrays are grown in random directions, with random lengths. The lengths of short nanorod arrays are below approximately 100 nm, and the long nanorod arrays are over 500 nm.

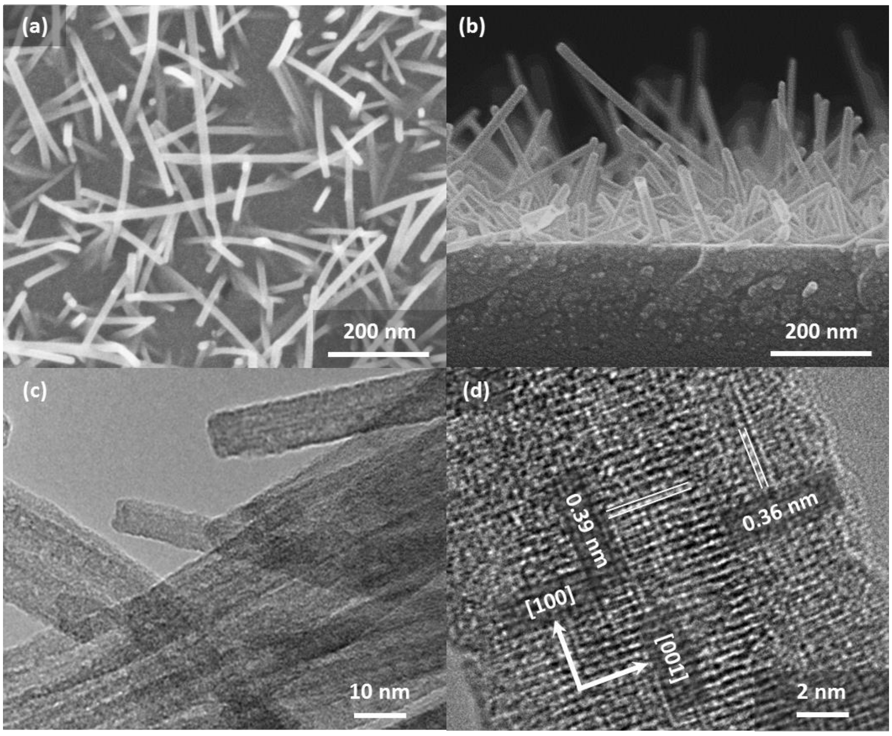

Figure 2.4 SEM and TEM images of as-synthesized MoO_3 nanorod arrays (2-ME, 0.5:1.5, 1000 rpm /10 s, 400 °C / 15 min): (a) vertical view of SEM image, (b) cross-sectional view of SEM image, (c) low-resolution TEM image of MoO_3 nanorod arrays, (d) high-resolution TEM image of MoO_3 nanorod arrays.

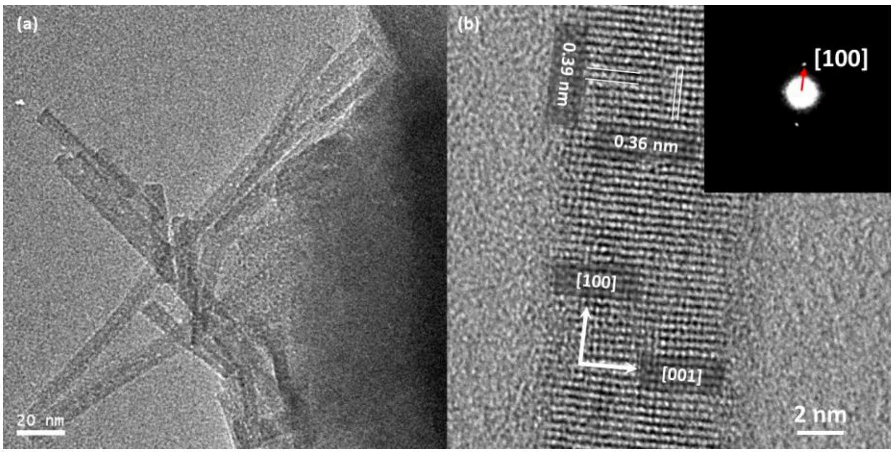

Figure 2.5 (a) low-resolution TEM image of MoO_3 nanorod arrays, (b) high-resolution TEM image of MoO_3 nanorod (inset, selected area electron diffraction (SAED) pattern of single MoO_3 nanorod).

The diameters of the nanorod arrays are approximately 10–20 nm, with a uniform needle shape. Figure 2.4 (c), (d) and Figure 2.5 show TEM images of the α-MoO_3 nanorod arrays. As can be seen in Figure 2.4 (c) and Figure 2.5 (a), the diameters of the nanorod arrays are also approximately 10–20 nm. The clear lattice fringes show the single-crystal nature of the nanorod arrays in Figure 2.4 (d) and Figure 2.5 (b). The spacings of the lattice plane are 0.39 nm and 0.36 nm, corresponding to the (100) and (001) planes of orthorhombic phase MoO_3, respectively. Combined with selected area electron diffraction (SAED) pattern of the nanorod, shown in the inset of Figure 2.5 (b), the nanorod arrays grow along the [100] direction. It also suggested that the maximum exposure side is the (010) facet, which agrees with the XRD results (Figure 2.1) and the literature[42].

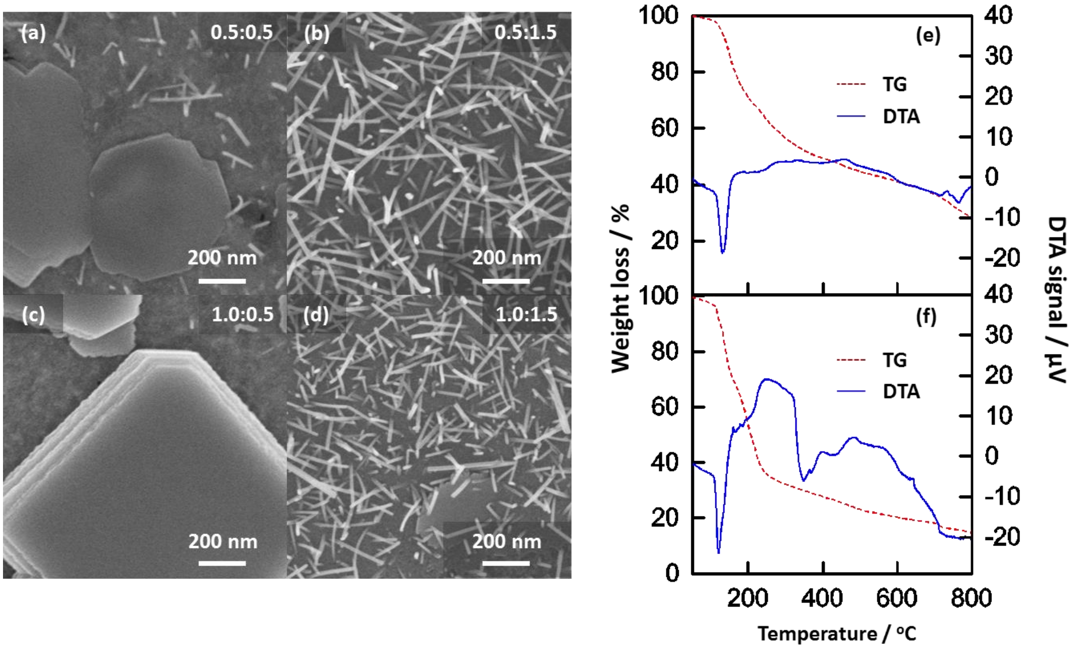

Figure 2.6 SEM images of as-synthesized samples (2-ME, 1000 rpm/10 s, 400 °C / 15 min) at various molar ratios: (a) 0.5:0.5, (b) 0.5:1.5, (c) 1.0:0.5, (d) 1.0:1.5, and TG/DTA (50 °C – 800 °C) curves of precursors with various molar ratios: (e) 0.5:0.5, (f) 0.5:1.5.

Finding that the obtained morphology strongly depended on the synthesis conditions, the molar ratio, solvents, and annealing parameters were assessed. The relationship between the molar ratio and the morphologies of the surface of the thin films was determined using nine different molar ratios of the molybdate source and citric acid, i.e., molybdate:citric acid ratios of 0.5–1.5:0.5–1.5. All of these precursors formed a transparent solution. The precursors were prepared using the same conditions, i.e., spin coating onto silica glass substrates at 1000 rpm for 10 s; then, all of the samples were sintered at 400 °C for 15 min in a preheated electro-furnace.

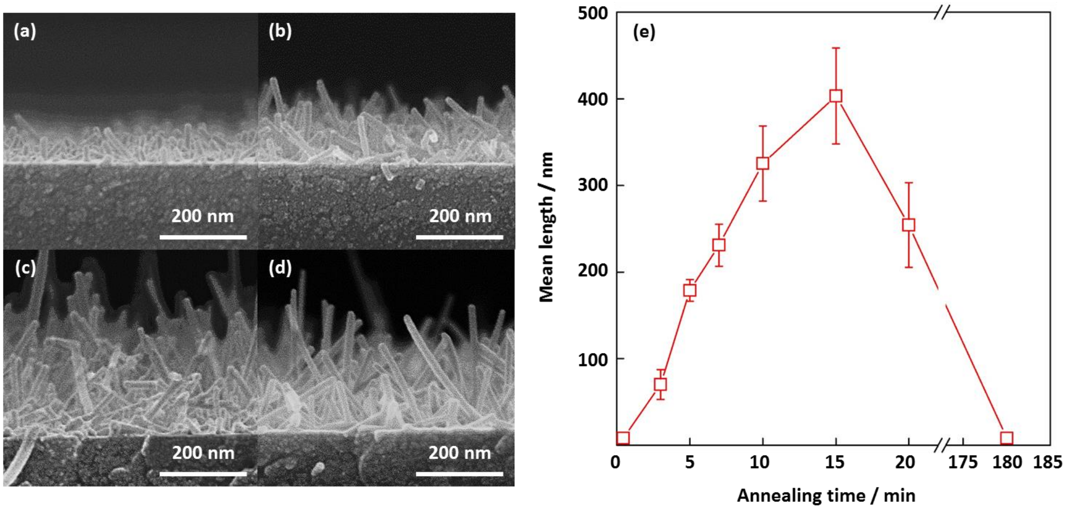

Figure 2.7 SEM images of nanorod arrays (2-ME, 0.5:1.5, 1000 rpm/10 s, 673 K) sintered for various times: (a) 3 min, (b) 5 min, (c) 10 min, (d) 15 min, and (e) curve of mean length of MoO_3 sintered at 400 °C for various times.

The SEM images of these samples are shown in Figures 2.6 (a)-(d) and Figure 2.7, and molar ratios of 0.5:0.5, 0.5:1.5, 1.0:0.5, and 1.0:1.5 are shown in Figure 2.6 (a)-(d). The morphologies of these samples are extremely different with varying molar ratios. Comparing Figure 2.6 (a) with 2.6 (b), and 2.6 (c) with 2.6 (d), the number of nanorod arrays increased with increasing relative amount of citric acid in the precursor (more detailed information can be seen in Figure 2.8). In particular, the 0.5:1.5 sample resulted in long MoO_3 nanorod arrays without nanoplates, nanospheres, or other nanoparticles. This indicated that the relative citric acid molar ratio with molybdate in the precursor play a crucial role in the competing crystal growth process of nanorod arrays and other particles. The influence of the molar ratio of molybdate:citric acid on the growth process of the nanorod arrays was also investigated with TG/DTA. Figures 2.6 (e) and 2.6 (f) show the TG/DTA curves with molar ratios of 0.5:0.5, and 0.5:1.5, respectively. The DTA plots of the 0.5:1.5 in Figure 2.6 (f) presented two endothermic peaks, one at approximately 127 ^{o}C and a broad peak at 330–400 ^{o}C; conversely, there is one endothermic peak at approximately 127 ^{o}C in the 0.5:0.5 DTA data of Figure 2.6 (e). From the TG/DTA data of citric oxidation [43], the possibility of reactions, given as equations (2.1) and (2.2):

$$(NH_4)_2MoO_4 + 3C_6H_8O_7 \rightarrow Mo(C_6H_6O_7)_3 + 4H_2O + NH_3 \tag{2.1}$$

$$2Mo(C_6H_6O_7)_3 + 27O_2 \rightarrow 2MoO_3 + 18H_2O + 36CO_2 \tag{2.2}$$

occur at the molar ratio of molybdate to citric acid of 1:3 during the synthesis process. The broad endothermic peak of the 0.5:1.5 sample (Figure 2.6 (f)) imply that the molar ratio of citric acid influences the nanorod growth process, and the growth temperature is consistent with the literature at around 400 ^{o}C [17, 44].

The influence of annealing time on the nanorod growth process was evaluated using spin-coated precursors with a molar ratio of 0.5:1.5 at 400 ^{o}C. Figures 2.7 (a)-(d) show the cross-sectional SEM images and the XRD patterns of samples annealed at 3–15 min.

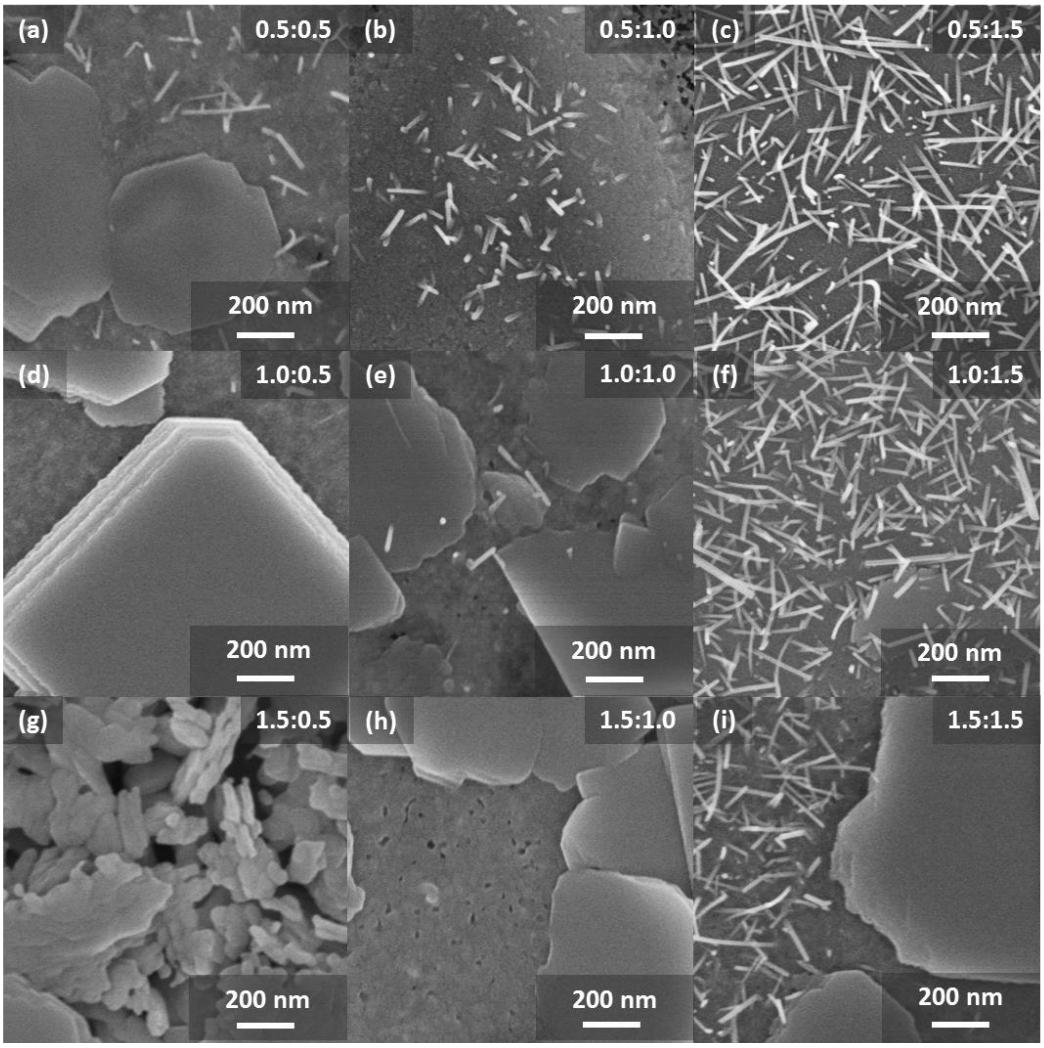

Figure 2.8 SEM images of nine types of samples (2-ME, 1000 rpm/10 s, 400 ^{o}C / 15 min) synthesized using solutions with various molar ratios of molybdate to citric acid, (a) 0.5:0.5, (b) 0.5:1.0, (c) 0.5:1.5, (d) 1.0:0.5, (e) 1.0:1.0, (f) 1.0:1.5, (g) 1.5:0.5, (h) 1.5:1.0, (i) 1.5:1.5.

The top-view SEM images of samples annealing from 1 min to 180 min are seen in Figures 2.8 and 2.9. From these SEM images, it is clear that the lengths of the nanorod arrays change with annealing time.

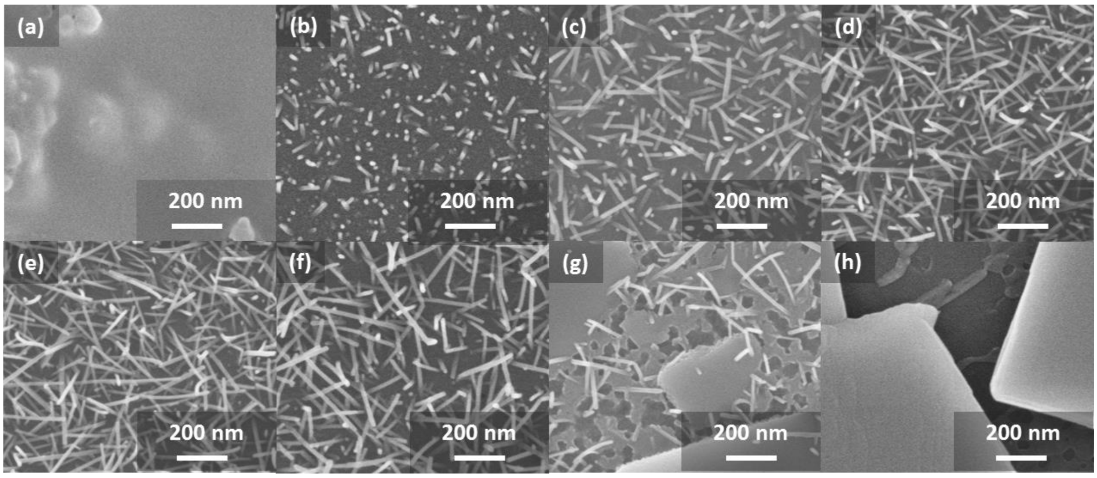

Figure 2.9 SEM images of MoO_3 nanorod arrays (2-ME, 0.5:1.5, 1000 rpm /10 s, 673 K) sintered at 673 K for various times: (a) 1 min, (b) 3 min, (c) 5 min, (d) 7 min, (e) 10 min, (f) 15 min, (g) 20 min, (g) 180 min.

The mean lengths of the nanorod arrays were collected from Figure 2.7 (a)-(d) and Figure 2.8 and plotted with standard deviation in Figure 2.7 (e) with respect to annealing time from 1 min to 180 min. There are two stages in the curve of Figure 2.7 (e). The lengths of nanorod arrays increase in the range from 0 min to 15 min as the first stage, then the lengths descend to zero at 180 min as the second stage. One possible reason for the increasing nanorod lengths at the first stage in Figure 2.7 (e) is that the nanorod arrays will nucleate and grow with the assistance of high temperature and citric acid as aforementioned. However, the process in the second stage will not react after 15 min because the molar ratio of the remaining citric acid could unsustain the growth of the nanorod arrays, resulting in the growth of the other particles, because of the citric acid decomposition and evaporation at high temperatures. These results suggest that the citric acid molar ratio in the precursors play a critical role in the growth of nanorod arrays.

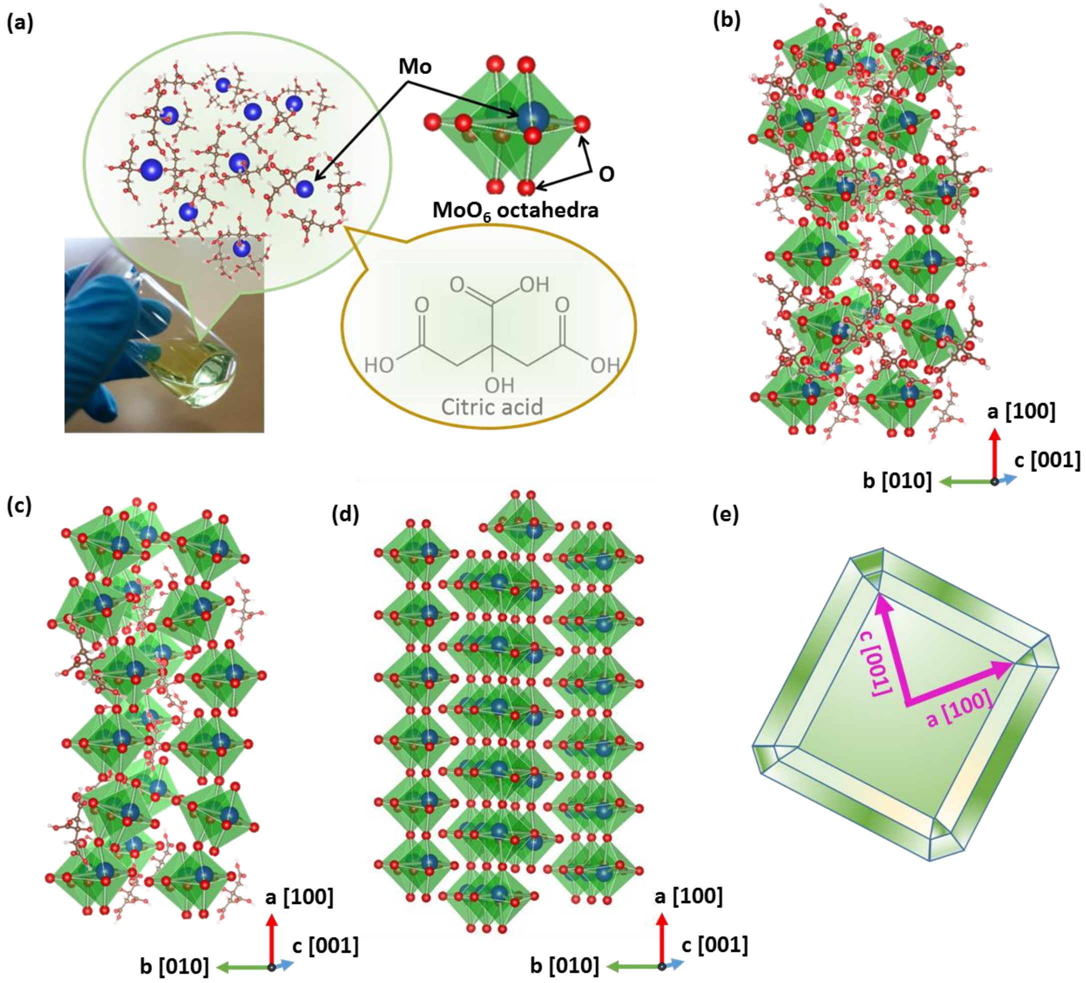

Figure 2.10 The schematic of growth mechanism for MoO_3 nanorod: (a) complex of Mo^{6+} and citric acid in precursor, (b) MoO_6 octahedra grow along the [100] direction at the assistance of citric acid, (c) β-MoO_3 nanorod, (d) α-MoO_3 nanorod, (e) nanorod change into nanoplate shape.

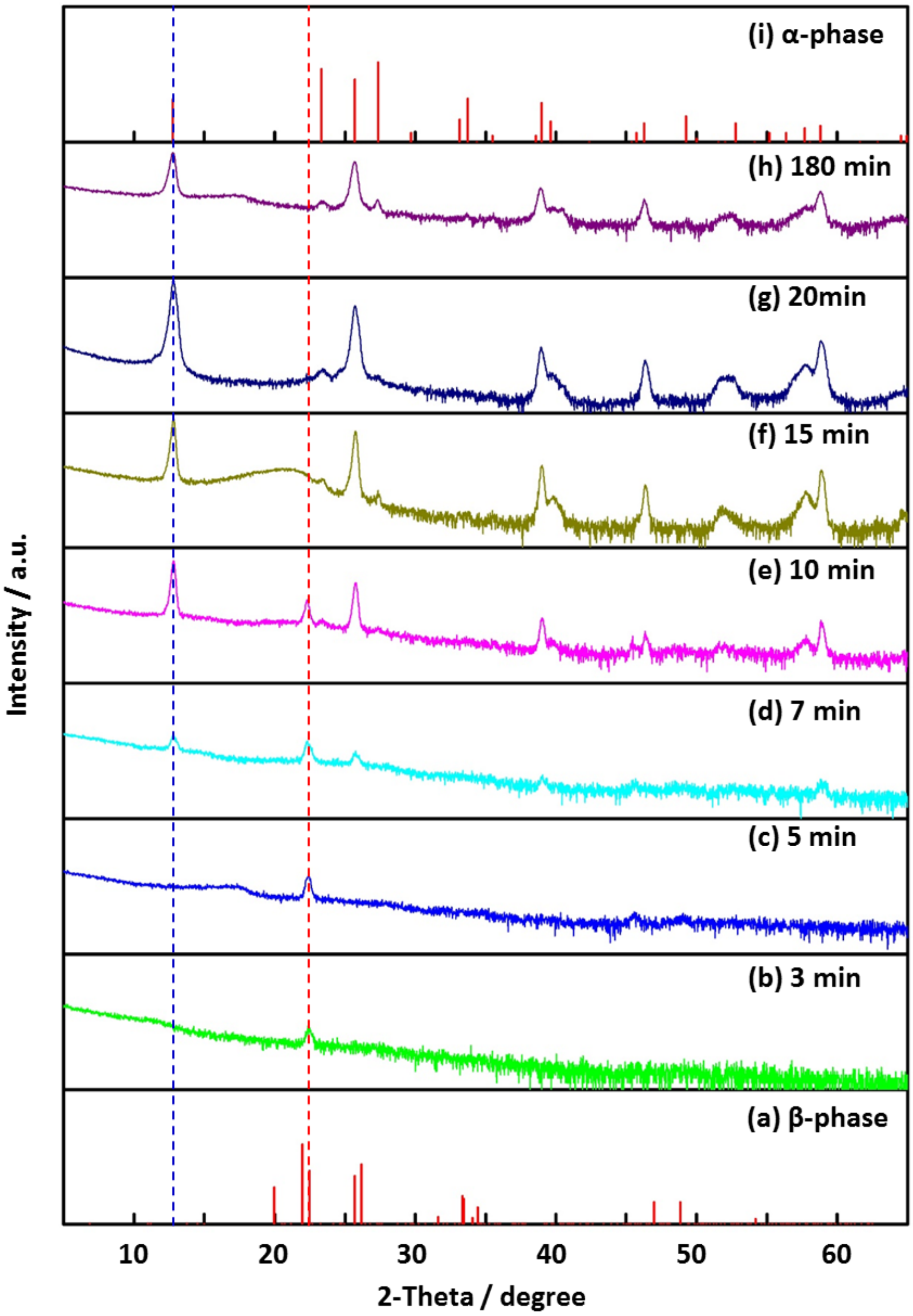

Figure 2.11 XRD patterns of MoO_3 (2-ME, 0.5:1.5, 1000 rpm/10 s, 400 °C) annealed for various times: (a) JCPDs card information 01-073-1537. (b) 3 min, (c) 5 min, (d) 7 min, (e) 10 min, (f) 15 min, (g) 20 min, (h) 180 min, (i) JCPDs card information 05-0508.

2.3.2 Mechanism of growth of α-MoO_3 nanorod arrays

The mechanism of the growth process of the nanorod arrays is presented from the above analysis, as shown in the Figure 2.10. During the entire course of the synthesis process citric acid should play multiple roles due to its chelating ability, provided by three carboxylic acid and one hydroxyl functional groups.

At the precursor forming stage, the citric acid coordinate as ligands with Mo^{6+} ions to form citrate complexes, shown in schematic Figure 2.10 (a), suggested by the transparent yellow solutions. At this stage, containing the citric acid in the precursors is very important. Only citric acid added into the mixtures can the molybdate powder be dissolved by organic solvents and can the transparent precursors form without the precipitate. Moreover, only the transparent precursor solutions can result in the nanorod arrays growth. After being sintered, Mo^{6+} will bond with oxygen resulting form into oxide. W. Di *et al.* maintained citrate ions can selectively bind to specific crystallographic facets, which will modify the nucleation rate and effectively restrict or promote the growth along specific directions, leading to dramatic modifications on the final shape of the crystals [45]. In the experiment on this study, MoO_3 nanorod arrays grow up along the direction of [100] at the action of citric acid and high temperature gradient (Figure 2.10 (a)-(b)). From XRD and SEM results of the annealing time, the phase of MoO_3 nanorod arrays change from β-phase to α-phase as seen in Figure 2.9 and 2.11. The part of citric acid around MoO_6 octahedra decompose and form the β-phase nanorod arrays in the step of Figure 2.10 (b) to Figure 2.10 (c). Then progressive citric acid decomposing, the β-phase nanorod arrays change to the α-phase nanorod arrays as shown in the Figure 2.10 (b) to Figure 2.10 (d). When the α-MoO_3 nanorod arrays continue to be annealed, the MoO_3 crystal will continue to grow up in terms of its inner bond strength, due to the vanish of citrate. The growth speed in the direction of [001] will exceeds the direction of [100], at the action of its stronger covalent force. While the growth speed in [010] direction is too low to grow in this direction, due to its weak Van der Waals force. Hence the growth in the direction of [001] and [100] results in the flat square shape of the α-MoO_3, as shown in Figure 2.10 (e) and Figure 2.9 (h). This mechanism imply that not only the amount of the citric acid in the precursor but also heating time dependence of the citric acid decomposition during film annealing is important factor in the anisotropic growth and phase transition of MoO_3.

To postpone the decomposition and evaporation of the citric acid to achieve much longer nanorod arrays, the solvent of the precursor is controlled. Three types of solvents, i.e., ethanol (C_2H_6O, Wako Pure Chemical Industries, Ltd., 99.0 %, boiling point 79 ^oC, Osaka, Japan), dimethylformamide (DMF, C_3H_7NO, Wako Pure Chemical Industries, Ltd., 99.5 %, boiling point 153 ^oC, Osaka, Japan), and dimethylacetamide (DMAC, C_4H_9NO, Wako Pure Chemical Industries, Ltd., 98.0 %, boiling point 167 ^oC, Osaka, Japan), were chosen to prepare the precursor solution because of their high solubilities and different boiling points. The three precursors from the different solvents all formed transparent solutions, in which the molar ratio of molybdate and citric acid is 0.5:1.5. After stable sol-solutions formed, they were treated at the same condition as the 2-ME solution (1000 rpm, 10 s, 400 ^oC, 15 min).

Figures 2.12 (a)-(d) show SEM images of the nanorod arrays synthesized using the four solutions: (a) ethanol, (b) 2-ME, (c) DMF, and (d) DMAC. The lengths of the nanorod arrays are quite different under the same synthesis conditions. The lengths of nanorod arrays in the ethanol sample are only about 100 nm, while those in DMAC are up to 600 nm, indicating that the solvent is also one of the determining parameters in nanorod synthesis [46, 47]. Foon *et al.* stated that the boiling points of solvents greatly influence the morphology of metal oxides [48]. The relationship between the mean length of the nanorod arrays and the boiling points of these four solvents is plotted in Figure 2.12 (e). As demonstrated in the curve, the lengths of nanorod arrays show an approximate linear dependence on the boiling points of the solvents. These results suggest that the solvent with higher boiling point will obviously postpone the evaporation of the precursor in the high-temperature conditions. The remnant excess precursor will provide further Mo ions to sustain the growth of MoO_3 nanorod arrays. Hence, solvents in the precursor act as an indirect factor during the growth process of nanorod arrays by altering the velocity of the decomposition and evaporation of citric acid in the precursor, which finally dominate the growth of the nanorod arrays up to 600 nm. As a consequence, this research study demonstrates a growth method for α-MoO_3 nanorod arrays by optimizing the relative molar ratio of citric acid, annealing time, and boiling temperature of the solvent, achieving a mean nanorod length of 500 nm.

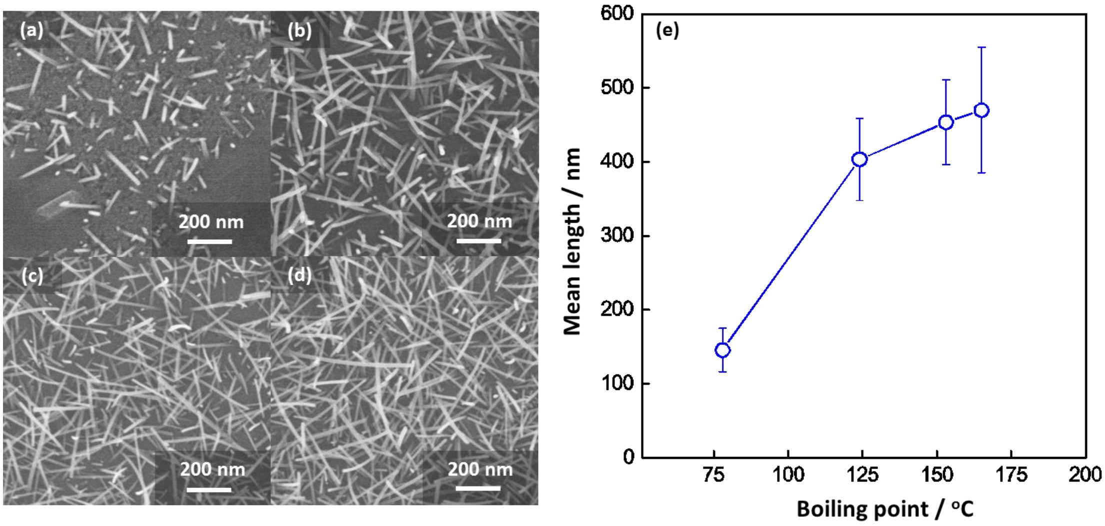

Figure 2.12 SEM images of MoO_3 nanorod arrays (0.5:1.5, 1000 rpm/10 s, 400 °C / 15 min) synthesized by using various solvents: (a) ethanol, (b) 2-ME, (c) DMF, (d) DMAC, and (e) curves of the relationship between the mean length of as-synthesized nanorod arrays and boiling points of these four solvents.

2.4 Conclusion

In this research, a simple sol-gel method was developed for synthesizing single-crystal α-MoO_3 nanorod arrays. Various synthesis conditions were examined to obtain the best criteria for producing longer nanorod arrays. The experiments indicate that the morphology of the obtained samples depends on the molar ratio of molybdate:citric acid, solvents, and annealing time. The molar ratio of citric acid is the key factor for the growth of the nanorod arrays. The lengths of the nanorod arrays increase with increasing relative molar ratio of citric acid. The controllable annealing times were optimized for the growth of nanorod arrays. According to the XRD results and TG-DTA analysis, the mechanism of MoO_3 anisotropic growth and phase transition from β to α with the decomposition timing of citric acid complex is derived. Moreover, the solvents also influence the morphologies of the nanorod arrays greatly by adjusting the rate of decomposition and evaporation of citric acid during the synthesis process of the nanorod arrays. The optimal growth conditions for long nanorod arrays are as follows: molar ratio of molybdate:citric acid = 0.5:1.5, DMAC as a solvent, and annealing at 673 K for 15 min. The mean length of the obtained α-MoO_3 nanorod arrays was about 500 nm, and the maximum nanorod arrays lengths can be extended up to approximately 600 nm. The knowledge which the decomposition rate of citric acid affect in growth of MoO_3 nanorod arrays can be applied to the material development for several electronic devices such as field emission, photo voltaic solar cell, lithium batteries, and gas sensors.

References

[1] Qi L. Colloidal chemical approaches to inorganic micro-and nanostructures with controlled morphologies and patterns. Coordination Chemistry Reviews 2010;254:1054.

[2] Liu Y, Goebl J, Yin Y. Templated synthesis of nanostructured materials. Chemical Society Reviews 2013;42:2610.

[3] Wang Z, Madhavi S, Lou XW. Ultralong α-MoO_3 nanobelts: synthesis and effect of binder choice on their lithium storage properties. The Journal of Physical Chemistry C 2012;116:12508.

[4] Zhou L, Wu HB, Wang Z, Lou XW. Interconnected MoO_2 nanocrystals with carbon nanocoating as high-capacity anode materials for lithium-ion batteries. ACS applied materials & interfaces 2011;3:4853.

[5] Wang Z, Chen JS, Zhu T, Madhavi S, Lou XW. One-pot synthesis of uniform carbon-coated MoO_2 nanospheres for high-rate reversible lithium storage. Chemical Communications 2010;46:6906.

[6] Wang Q, Wang Q, Zhang DA, Sun J, Xing LL, Xue XY. Core-shell α-Fe_2O_3@α-MoO_3 nanorods as lithium‐ion battery anodes with extremely high capacity and cyclability. Chemistry–An Asian Journal 2014;9:3299.

[7] Wang Q, Zhang D-A, Wang Q, Sun J, Xing L-L, Xue X-Y. High electrochemical performances of α-MoO_3@MnO_2 core-shell nanorods as lithium-ion battery anodes. Electrochimica Acta 2014;146:411.

[8] Morales AM, Lieber CM. A laser ablation method for the synthesis of crystalline semiconductor nanowires. Science 1998;279:208.

[9] Huang MH, Mao S, Feick H, Yan H, Wu Y, Kind H, Weber E, Russo R, Yang P. Room-temperature ultraviolet nanowire nanolasers. Science 2001;292:1897.

[10] Hu J, Odom TW, Lieber CM. Chemistry and physics in one dimension: synthesis and properties of nanowires and nanotubes. Accounts of chemical research 1999;32:435.

[11] Xia Y, Yang P, Sun Y, Wu Y, Mayers B, Gates B, Yin Y, Kim F, Yan H. One‐dimensional nanostructures: synthesis, characterization, and applications. Advanced materials 2003;15:353.

[12] Wen W, Wu J-M, Wang Y-D. Flash synthesis of macro-/mesoporous ZnO for gas sensors via self-sustained decomposition of a Zn-based complex. RSC Adv. 2013;3:12052.

[13] Law M, Greene LE, Johnson JC, Saykally R, Yang P. Nanowire dye-sensitized solar cells. Nat. Mater. 2005;4:455.

[14] Xu C, Shin P, Cao L, Gao D. Preferential growth of long ZnO nanowire array and its application in dye-sensitized solar cells. The Journal of Physical Chemistry C 2009;114:125.

[15] Qiu J, Li X, He W, Park S-J, Kim H-K, Hwang Y-H, Lee J-H, Kim Y-D. The growth mechanism and optical properties of ultralong ZnO nanorod arrays with a high aspect ratio by a preheating hydrothermal method. Nanotechnology 2009;20:155603.

[16] Chen JS, Cheah YL, Madhavi S, Lou XW. Fast synthesis of α-MoO_3 nanorods with controlled aspect ratios and their enhanced lithium storage capabilities. The Journal of Physical Chemistry C 2010;114:8675.

[17] Brezesinski T, Wang J, Tolbert SH, Dunn B. Ordered mesoporous [alpha]-MoO_3 with iso-oriented nanocrystalline walls for thin-film pseudocapacitors. Nat. Mater. 2010;9:146.

[18] Carcia P, McCarron E. Synthesis and properties of thin film polymorphs of molybdenum trioxide. Thin Solid Films 1987;155:53.

[19] Chu W, Zhang L, Wang H, Han Z, Han D, Li Q, Fan S. Direct thermal oxidization evaporation growth, structure, and optical properties of single-crystalline nanobelts of molybdenum trioxide. J. Mater. Res. 2007;22:1609.

[20] Taurino AM, Forleo A, Francioso L, Siciliano P, Stalder M, Nesper R. Synthesis, electrical characterization, and gas sensing properties of molybdenum oxide nanorods. Appl. Phys. Lett. 2006;88:2111.

[21] Li W, Cheng F, Tao Z, Chen J. Vapor-transportation preparation and reversible lithium intercalation/deintercalation of α-MoO_3 microrods. The Journal of Physical Chemistry B 2006;110:119.

[22] Zhou J, Deng S, Xu N, Chen J, She J. Synthesis and field-emission properties of aligned MoO_3 nanowires. Appl. Phys. Lett. 2003;83:2653.

[23] Wei XM, Zeng HC. Large-scale organizations of MoO_3 nanoplatelets with single-crystalline MoO_3(4,4'-bipyridyl)0.5. The Journal of Physical Chemistry B 2003;107:2619.

[24] Cong S, Sugahara T, Wei T, Jiu J, Hirose Y, Nagao S, Suganuma K. Growth and extension of one-step sol–gel derived molybdenum trioxide nanorods via controlling citric acid decomposition rate. Cryst. Growth Des. 2015;15:4536.

[25] Meduri P, Clark E, Kim JH, Dayalan E, Sumanasekera GU, Sunkara MK. MoO_{3-x} nanowire arrays as stable and high-capacity anodes for lithium ion batteries. Nano Lett. 2012;12:1784.

[26] Liang R, Cao H, Qian D. MoO_3 nanowires as electrochemical pseudocapacitor materials. Chemical Communications 2011;47:10305.

[27] Wang Q, Sun J, Wang Q, Zhang D-a, Xing L, Xue X. Electrochemical performance of α-MoO_3–In_2O_3 core–shell nanorods as anode materials for lithium-ion batteries. J. Mater. Chem. A 2015;3:5083.

[28] Dinh NN, Chung DN, Thao TT, Thuy TTC, Chi LH, Truong V-V. Enhancement of performance of organic light emitting diodes by using Ti-and Mo-oxide nano hybrid layers. Materials Sciences and Application, 2013;4;275.

[29] Comini E, Yubao L, Brando Y, Sberveglieri G. Gas sensing properties of MoO_3 nanorods to CO and CH_3OH. Chem. Phys. Lett. 2005;407:368.

[30] Ibrahem MA, Wu F-Y, Mengistie DA, Chang C-S, Li L-J, Chu CW. Direct conversion of multilayer molybdenum trioxide to nanorods as multifunctional electrodes in lithium-ion batteries. Nanoscale 2014;6:5484.

[31] Navas I, Vinodkumar R, Lethy K, Detty A, Ganesan V, Sathe V, Pillai VM. Growth and characterization of molybdenum oxide nanorods by RF magnetron sputtering and subsequent annealing. Journal of Physics D: Applied Physics 2009;42:175305.

[32] Lou XW, Zeng HC. Hydrothermal synthesis of α-MoO_3 nanorods via acidification of ammonium heptamolybdate tetrahydrate. Chem. Mat. 2002;14:4781.

[33] Zheng L, Xu Y, Jin D, Xie Y. Well-aligned molybdenum oxide nanorods on metal substrates: solution-based synthesis and their electrochemical capacitor application. J. Mater. Chem. 2010;20:7135.

[34] Cho IS, Lee CH, Feng Y, Logar M, Rao PM, Cai L, Kim DR, Sinclair R, Zheng X. Codoping titanium dioxide nanowires with tungsten and carbon for enhanced photoelectrochemical performance. Nature communications 2013;4:1723.

[35] Kim H-D, Yun MJ, Lee JH, Kim KH, Kim TG. Transparent multi-level resistive switching phenomena observed in ITO/RGO/ITO memory cells by the sol-gel dip-coating method. Sci Rep 2014;4.

[36] Shakir I, Shahid M, Kang DJ. MoO_3 and $Cu_{0.33}MoO_3$ nanorods for unprecedented UV/Visible light photocatalysis. Chemical Communications 2010;46:4324.

[37] Choopun S, Mangkorntong P, Subjareon P, Mangkorntong N, Tabata H, Kawai T. Orthorhombic molybdenum trioxide whiskers by vapor transport method. Japanese journal of applied physics 2003;43:L91.

[38] Fang L, Shu Y, Wang A, Zhang T. Green synthesis and characterization of anisotropic uniform single-crystal α-MoO_3 nanostructures. The Journal of Physical Chemistry C 2007;111:2401.

[39] Segawa K, Ooga K, Kurusu Y. Molybdenum peroxo complex. Structure and thermal behavior. Bulletin of the Chemical Society of Japan 1984;57:2721.

[40] Stoyanova A, Iordanova R, Mancheva M, Dimitriev Y. Synthesis and structural characterization of MoO_3 phases obtained from molybdic acid by addition of HNO_3 and H_2O_2. Journal of Optoelectronics and Advanced Materials 2009;11:1127.

[41] Chernova NA, Roppolo M, Dillon AC, Whittingham MS. Layered vanadium and molybdenum oxides: batteries and electrochromics. J. Mater. Chem. 2009;19:2526.

[42] Wang L, Gao P, Zhang G, Chen G, Chen Y, Wang Y, Bao D. Synthesis of mesoporous MoO_3 nanoribbons through a multi‐molybdate coordination‐polymer‐precursor route. European Journal of Inorganic Chemistry 2012;2012:5831.

[43] Shi L, Zeng C, Jin Y, Wang T, Tsubaki N. A sol–gel auto-combustion method to prepare Cu/ZnO catalysts for low-temperature methanol synthesis. Catalysis Science & Technology 2012;2:2569.

[44] Kurtoglu ME, Longenbach T, Gogotsi Y. Synthesis of quasi-oriented α-MoO_3 nanobelts and nanoplatelets on TiO_2 coated glass. J. Mater. Chem. 2011;21:7931.

[45] Di W, Willinger M-G, Ferreira RA, Ren X, Lu S, Pinna N. Citric acid-assisted hydrothermal synthesis of luminescent TbPO4: Eu nanocrystals: controlled morphology and tunable emission. The Journal of Physical Chemistry C 2008;112:18815.

[46] Epifani M, Imperatori P, Mirenghi L, Schioppa M, Siciliano P. Synthesis and characterization of MoO_3 thin films and powders from a molybdenum chloromethoxide. Chem. Mat. 2004;16:5495.

[47] Dong W, Dunn B. Sol–gel synthesis of monolithic molybdenum oxide aerogels and xerogels. J. Mater. Chem. 1998;8:665.

[48] Foo KL, Kashif M, Hashim U, Liu W-W. Effect of different solvents on the structural and optical properties of zinc oxide thin films for optoelectronic applications. Ceramics International 2014;40:753.

Chapter 3

VOC gas sensing devices based on molybdenum trioxide nanorod arrays

Abstract

Nanorod arrays gas sensors are attracting much scientific and engineering interest because of their excellent sensing performance arising from their unique nanostructures. In this work, large-scale random 3D networks of ultra-fine single-crystal α-MoO_3 nanorod arrays were synthesized and were applied as gas sensors. The arrays as sensor are spontaneously grown by a simple single-step solution route. A response and screaning capability of ethanol, methanol, isopropanol and acetone vapors at 300 ^{o}C are investigated *via* the modulation of the resistance of the gas sensors. The sensitivity, response time and recovery time of the sensors strongly depend on the specific morphologies of the nanorod arrays, such as length, number and coverage of nanorods in the 3D network. A reaction mechanism, in which the 3D-network nanorod arrays adsorb and react with the target molecules more readily than the seed layer, is proposed to explain the different response and recovery times of the sensors. These random 3D-network nanorod arrays with functionally tunable morphology are promising for universal application as gas sensors for detecting various vapors, and will provide valuable insights for the production of fast, large-scale, low-cost and simple synthesis of sensing devices.

3.1 Introduction

To fabricate electronic devices with high performance through simpler and faster processes is an objective of technological evolution [1-3]. In particular, the limitations of cost-effectiveness, time consumption and energy conservation in the synthesis of advanced functional materials and device fabrication are the main problems that need to be overcome for the mass production of electronic devices [4-7]. Over the past decades, semiconductor metal oxide (SMO)-based gas sensors for toxic and explosive volatile organic compounds (VOCs) have drawn much attention from researchers because of their advantages of sensitivity, rapid response and inexpensive production [8, 9]. Recently, considerable effort has been devoted to developing much simpler routes to control the shape and grain size of SMO to achieve a higher surface-to-area ratio and unique surface chemistry behavior to improve sensing performance [10-12].

Among the metal oxides, molybdenum trioxide (MoO_3) is one of the most desirable for use in gas sensors because of its indirect wide band gap of 3.5 eV [13-15]. MoO_3-based gas analyzing devices show excellent gas sensing properties for several kinds of gas species [16-21] because of their special quantum size effect, surface effect, high reactivity and the polyvalency of molybdate. In particular, MoO_3 nanostructures, such as MoO_3 nanobelts, flower-like microstructured MoO_3, and net-like MoO_3 porous architectures synthesized by the hydrothermal route, exhibit appealing sensing properties for VOC vapors [22-24]. The gas sensing properties of MoO_3 thin film fabricated by radio-frequency (RF) sputtering have also been investigated [25]. These reports showed the nanostructures possessed typical sensing performance for VOC vapors; however, these nanostructures need to be processed with two or more steps, which is time consuming. For instance, these nanostructures need to be transferred or arranged on a ceramic substrate and then annealed to obtain substantial growth/adhesion on the substrate. To increase the VOC gas sensing performance of nanostructures, they needed to be loaded with noble metal particles (*e.g.*, Au, Pt, Pd) by further sputtering or solution processes, which increased the fabrication time and cost of the gas sensor [26, 27]. Compared with other nanostructures, nanorod arrays are very promising for use as gas sensors because of their high surface-to-volume ratio and reaction rate with surface-adsorbed species resulting from the 3D structure that is less agglomerated than the bulk material [28-30]. SMO nanorod arrays composed of WO_3, ZnO, and SnO_2 have been demonstrated to be very sensitive to VOC vapors [31-33]. However, few MoO_3 nanorod arrays gas sensors have been reported. This is because it is difficult to grow MoO_3 nanorods in the vertical direction by simple methods. MoO_3 nanorod arrays have been synthesized by several methods, such as thermal evaporation [34], pulsed electron beam [35], RF sputtering [36], and chemical vapor deposition [37], all of which are time consuming and require complicated vacuum systems. Recently, Zhang *et al.* [38] reported a two-step solution-based route to synthesize MoO_3 nanorod arrays by firstly depositing a seed layer and subsequent hydrothermal treatment to directly grow well-aligned MoO_3 and MoO_2 nanorods on metallic substrates. However, this process was time consuming with multiple steps, and involved a high pressure environment. The aforementioned complicated methods seriously restrict the application of MoO_3 nanorod arrays in gas sensing. Recently, a simple one-step metal–organic decomposition (MOD) route was developed by our group to fabricate α-MoO_3 nanorod arrays [39]. The MOD route involves a facile, inexpensive, and one-step sol–gel process, making it attractive for the production of α-MoO_3 nanorod arrays for use as gas sensors.

In this work, α-MoO_3 nanorod array gas sensors were fabricated using a simple MOD method and their sensing properties for VOC vapors were investigated. The α-MoO_3 nanorod arrays consist of nanorods with a diameter of about 10 nm grown in random directions to form a 3D network structure by simply annealing in air for several minutes. The lengths and densities of the α-MoO_3 nanorods are controlled by modulating the synthesis conditions. The dependence of the sensing properties of the α-MoO_3 nanorod array gas sensors on structural parameters such as the length, number, and area of α-MoO_3 nanorod arrays is investigated. The relationships between the nanostructure and sensing properties of the α-MoO_3 nanorod arrays are established in detail along with the reaction and sensing mechanism. The knowledge garnered from this study can greatly contribute to the research and development of gas analyzer electronics devices.

3.2 Experimental

3.2.1 Fabrication of α-MoO_3 nanorod arrays gas sensors

All reagents were purchased from Wako Pure Chemical Industries, Ltd., Osaka, Japan. The α-MoO_3 nanorod arrays used for gas sensors were synthesized with the method narrated in chapter 2. In a typical process, ammonium molybdate ($H_8N_2O_4Mo$) and citric acid ($C_6H_8O_7$) were dissolved in EtOH, 2-ME, DMF or DMAC at room temperature. Following aging at room temperature for 24h, clear and transparent solutions were obtained. These precursor solutions were spin coated onto square silica-glass substrates (20×20 mm) to form uniform thin films, which were annealed at 400 ^oC in a preheated furnace for 15 min (DENKEN KDF-P90, Kyoto, Japan) in air for 15 min to produce thin α-MoO_3 nanorod arrays. Top and cross-sectional views of the morphology of these samples were observed by field-emission scanning electron microscopy (FE-SEM: Hitachi SU8020, Tokyo, Japan) at 5 kV and 10 mA, before observation, the thin films were sputtered with Pt to reduce charging and obtain clear images at the condition of 20 mA, 10 s (ION SPUTTER: Hitachi E-1045, Tokyo, Japan). Silver contacts were pasted on the two opposite edges of the as-prepared nanorod array samples after FE-SEM observation to fabricate typical gas sensors. The silver paste [40] electrodes were about 3 mm wide. After contact formation, the nanorod arrays were sintered at 200 ^oC for 30 min in air to obtain a substantial ohmic contact.

3.2.2 Characterization methods of α-MoO_3 nanorod arrays used for gas sensors

The gas sensing characteristics of the α-MoO_3 nanorod array devices were investigated using a specialized gas sensor testing system composed of a source meter

(2110 5 1/2 Digit multimeter, Keithley Instruments Inc., USA) combined with a quartz glass tube, which were surrounded and preheated to 300 °C by a tubular electric furnace. Two small vents were included at the two ends of the tube to introduce the target vapors and air. After the α-MoO_3 nanorod array gas sensor reached its thermal equilibrium state at 300 °C, a controlled volume of VOC was injected into the hot chamber by a pipette. The VOCs were immediately vaporized and completely filled the tube to react with the α-MoO_3 nanorod arrays. The concentrations of the target vapors were adjusted from 25 to 500 ppm calculated by equation (3.1).

$$V_{tg} = \frac{10^{-9} V_0 \cdot M \cdot C_{tg}}{22.4 \rho \cdot p} \tag{3.1}$$

Here, V_0 is the volume of the chamber (4.71 L); ρ, M, p, V_{tg} and C_{tg} are the density, molar mass, purity, volume and vapor concentration of the VOC liquid reagents [41].

The sensitivity was defined as the ratio of the normalized resistances of the α-MoO_3 nanorod gas sensor exposed to the air and VOC vapor. The normalized resistance of the gas sensor was the percentage of the real-time value to the initial resistance value of the sensor during the testing process. The response time was defined as the time when the resistance of the sensor reached 90 % of the stable value of the resistance in the target gas. Similarly, the recovery time was defined as the time at which the resistance returned to 90 % of its initial value as ambient air flowed into the glass tube.

3.3 Results and discussion

3.3.1 Characterization of α-MoO_3 nanorod arrays

First, α-MoO_3 nanorod arrays were fabricated, as shown in chapter 2, using four different solvents: ethanol (EtOH), 2-methoxyethanol (2-ME), dimethylformamide (DMF) and dimethylacetamide (DMAC). The four kinds of α-MoO_3 nanorod arrays using different solvents, *i.e.*, EtOH, 2-ME, DMF and DMAC, are denoted as NR-A, NR-B, NR-C, and NR-D, respectively. Ag contacts were pasted on the two opposite edges of the as-prepared each nanorod array samples to fabricate typical gas sensors and a schematic image of the gas sensing process., as shown in Figure 3.1a and 3.11b.

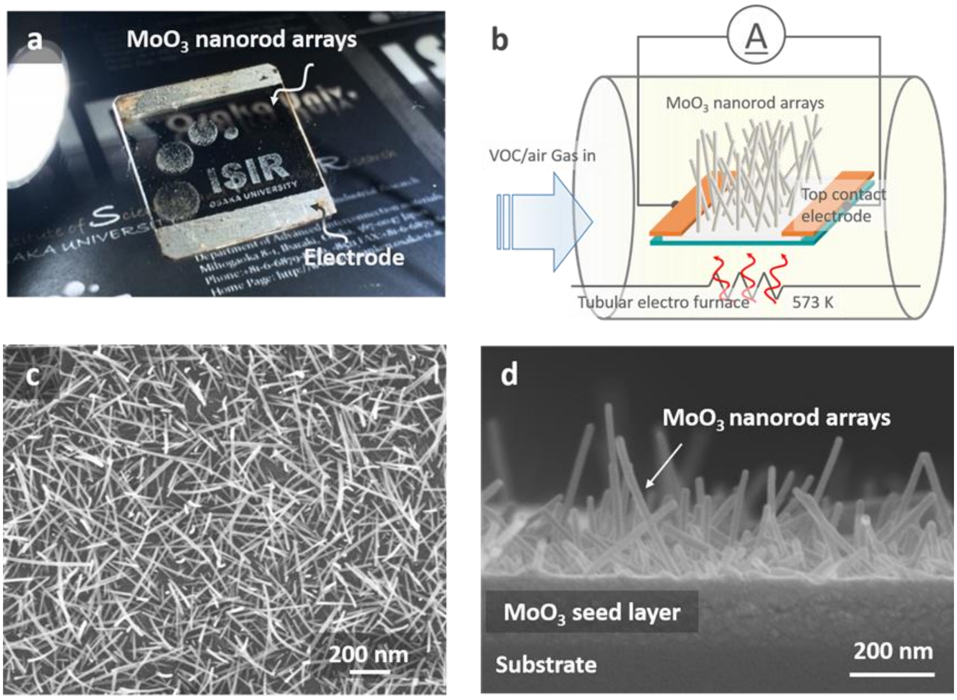

Figure 3.1 (a) Photograph of the α-MoO_3 nanorod arrays gas sensor; silver electrodes were pasted at the two opposite edges. (b) Schematic diagram of the gas sensing process of the α-MoO_3 nanorod arrays gas sensor. (c) Top-view scanning electron microscopy (SEM) images of NR-D. (d) Cross-sectional SEM images of NR-D.

Figure 3.1c shows a top-view field-emission scanning electron microscopy (FE-SEM) image of a typical NR-D. The nanorods grew from the substrates with different orientations to form random 3D network structures. Figure 3.1d depicts a cross-sectional FE-SEM image of the same α-MoO_3 nanorod arrays. The α-MoO_3 nanorods grew from the substrate in random directions, and had a diameter of about 10 nm and length of about 100 - 700 nm. The single-crystalline and single α-phase nature of the nanorods were confirmed in the previous chapter. In addition, a seed layer was observed about 200 nm above the substrate under the nanorod array layer, which provided a tight contact between the nanorods and substrates.

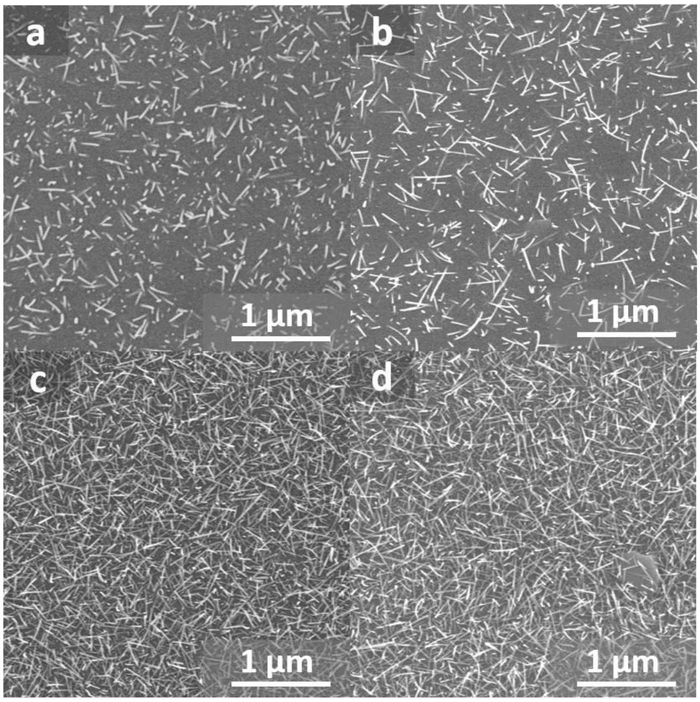

Figure 3.2 Top-view SEM images of α-MoO_3 nanorod arrays: (a) NR-A; (b) NR-B; (c) NR-C (d) NR-D.

The nanorod arrays synthesized using different solvents possessed different morphologies, as shown in Figure 3.2. NR-A exhibited the shortest and fewest nanorods. NR-B nanorods were longer and somewhat more numerous than NR-A, but shorter and fewer than NR-C ones. NR-D possessed the longest and most nanorods of the samples. Four specific morphological factors of the nanorods, *i.e.*, mean length, number, coverage area and their product were obtained from the SEM images in Figure 3.2 a–d within an area of 112 μm^2 and are depicted in Figure 3.3. When the four specific morphological factors were quantified, 7 lines of latitude and longitude with fixed interval distance were drawn across the area of Figure 3.2. Then the number and length of nanorods, which came across with the lines, were counted and averaged. The coverage area of nanorod arrays were calculated using the total area of SEM image in Figure 3.2 minus the total uncovered area. The total uncovered area was calculated from the product of uncovered area near the lines of latitude and longitude.

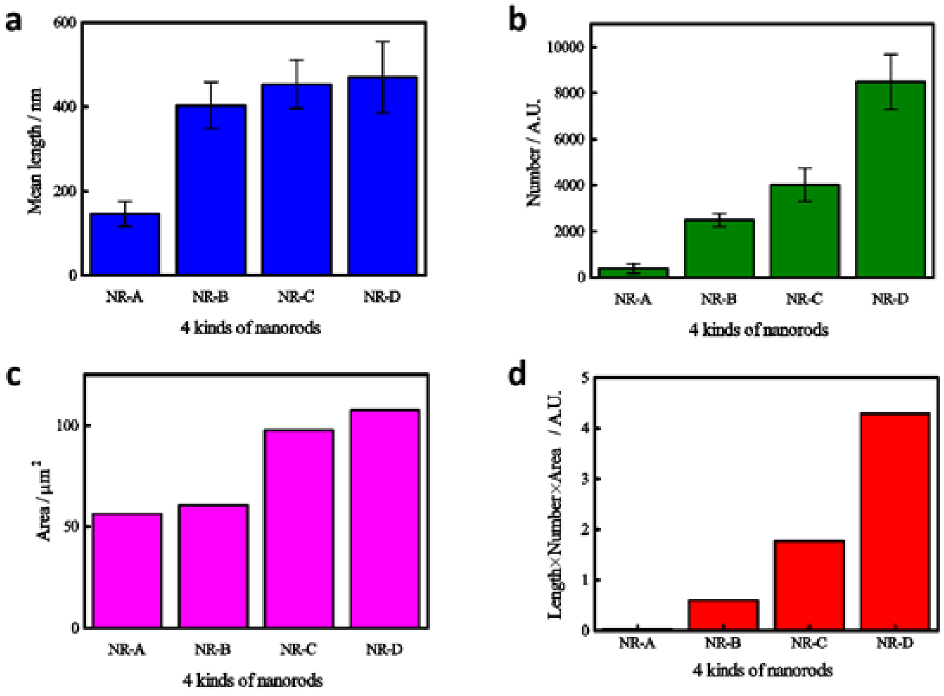

Figure 3.3 Specific structural parameter distributions of the nanorods in the four kinds of α-MoO_3 nanorod arrays, which was calculated from Figure 3.2: (a) Mean length distributions; (b) Number distributions; (c) Areas covered by the α-MoO_3 nanorods arrays; (d) length × number × area of the α-MoO_3 nanorod arrays for each sample.

3.2.2 Gas sensing properties of α-MoO_3 nanorod arrays to VOCs

The gas sensor performance of α-MoO_3 nanorod arrays was evaluated by detecting resistance variation at an operating temperature of 300 °C. Figure 3.4a presents the normalized resistance response of the nanorod gas sensors to 500 ppm EtOH. The resistance of all the nanorod arrays immediately decreased when exposed to EtOH vapor and increased in ambient air. This behavior is typical of an n-type SMO-based sensor [10].

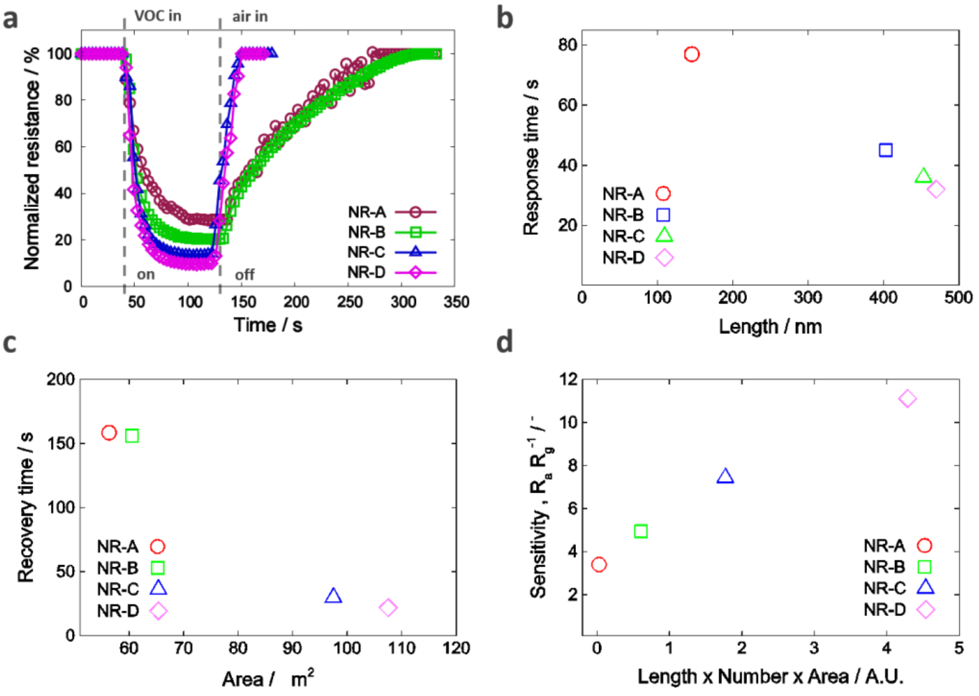

Figure 3.4 (a) Normalized resistance curves to 500 ppm ethanol for α-MoO_3 nanorod array gas sensors NR-A, NR-B, NR-C, and NR-D at 300 °C. (b) Length-dependent response times of α-MoO_3 nanorod array gas sensors. (c) Recovery times plotted against area coverage. (d) Comparison of sensitivities with the product of the specific morphological factors: length × number × area.

The resistance modulation amplitude and response times of these four samples exhibited obvious differences. NR-D exhibited the biggest and fastest decrease of resistance, followed by NR-C, and NR-A had the lowest response. These results indicate that NR-D was the most sensitive device to EtOH vapor, followed by NR-C, NR-B and then NR-A. Interestingly, the recovery speed following EtOH removal in Figure 3.4a showed obvious differences for the four kinds of nanorods. The recovery regions can be divided into two categories; one of NR-C and NR-D with fast recovery times of about 30 s, similar to their response times, and the other was NR-A and NR-B with slow recovery times of over 150 s. These results indicate that the sensitivity and response of the sensors depended on the geometrical aspect of nanorod arrays. Values of the sensitivity, response time and recovery time calculated from Figure 2a are summarized in Table 3.1. NR-D showed a sensitivity of 12, response time of 32 s, and recovery time of 23 s, which represented the highest performance of the random 3D nanorods arrays investigated here.

Table 3.1 Gas sensing performance of four α-MoO_3 nanorod arrays gas sensors to 500 ppm EtOH vapor.

Device	Sensitivity R_a/R_g	Response time s	Recovery time s
NR-A	3	77	159
NR-B	5	45	156
NR-C	7	36	30
NA-D	12	32	23

Gas sensor performance is very sensitive to morphological parameters such as surface area and porosity[42]. The relevance of the sensitivity, response time and recovery time of these nanorods to morphological factors is illustrated in Figure 3.4b, c and d, respectively. The sensitivities of sensors increased linearly with the values of the combined factors of length, number and coverage area of the nanorods (Figure 3.4d). This implies that the total sensor performance, that is, sensitivity, strongly depend on all the morphology factors of length, number and coverage area of nanorods. Meanwhile, the response and recovery times showed strong correlations with only some of the morphology factors. The response time of the sensors exhibited an inverse proportional relationship with the mean length of the α-MoO_3 nanorods (Figure 3.4b), suggesting the length of the nanorods is the major factor influencing the response time. In contrast, the recovery time of the α-MoO_3 nanorods was inversely linearly proportional to the area covered by the α-MoO_3 nanorods (Figure 3.4c). These results imply the different adsorption and desorption abilities of gas molecules for specific nanorod shapes.

As mentioned above, the random 3D nanorod array samples were composed of two parts: an upper layer of nanorods and lower seed layer. The sensor performance might be affected by the different adsorption/desorption abilities of these two parts for target molecules due to the nanorod arrays provided much more active sites, compared with the dense seed layer. When exposed to EtOH vapor, the much higher adsorption of the nanorod layer than the seed one gives rise to the faster change and more induced charges in the nanorod layer [43]. Rath *et al* [44]. stated that the response process can be considered as the adsorption rate increase with the increase of reaction frequency with the expanding surface area and rising VOC gas pressure. If the active layer of a gas sensor is covered with nanorods, the resistance variation of the nanorod layer represents the resistance variation of the whole sensor during the response process. The longer nanorods substantially shorten the carrier transportation routes because of the many junctions between the 3D nanorod networks. Therefore, the response time considerably decreases with increasing length of the nanorods (Figure 3.4b).

In contrast to the response process, Rath *et al*.[44] proposed that the desorption rate is determined by the strength of gas molecule–surface bonding with oxide (MoO_3 in this case) and the surface area. In this experiment, the MoO_3 nanorods showed almost the same molecule–surface bonding force, but the bulk MoO_3, such as the dense seed layer, possesses a different molecule–surface bonding force because the surface potential energy of nanorods is higher than that of the bulk layer [45], as seen in Figure 3.5. Because the lower surface potential energy results in a stronger bonding force between the oxide surface and gas molecules, the desorption ability becomes weak when exposed to the gas during the recovery process, which suggests that recovery time can be delayed in the dense seed layer compared with that of the nanorods.

For NR-A and NR-B, the surface coverage of nanorods are only about half that of NR-C and NR-D; *i.e.*, half the surface area required EtOH to be desorbed from the dense seed layer in NR-A and NR-B. The porous, randomly distributed 3D nanorods with much higher surface potential energy than that of the seed layer display rapid desorption of EtOH vapor and readsorption of oxygen, leading to a rapid increase in resistance. Conversely, the dense seed layer area can retain comparatively more remnant charges, because of the slow desorption/readsorption process, which are caused by the strong bonding of VOC molecules. The slow decrease of charges in the dense seed layer results in the slow increase of the whole sensor resistance, which explains the slow recovery times of NR-A and NR-B. This mean that the nanorod-covered surface area dominate the recovery process of the VOC gas sensing devices. The detailed mechanism of the NR-C and NR-D-based sensors is outlined in Figure 3.6.

Moreover, the random 3D nanorod array samples are composed of an upper layer of nanorods and lower seed layer. The sensor performance are influenced by the different adsorption and desorption abilities of these two layers to target molecules. Compared with the dense seed layer, the nanorod array layer provided much more active sites to allow the quicker and increased adsorption of target molecules[43]. The nanorod arrays possess much higher surface potential than the seed layer[45], which cause more induced charges to generate and combine more quickly in the nanorod arrays layer than in the seed layer. Surface energy band variation of the nanorods and seed layer in air and EtOH are shown in Figure 3.5a and b.

When exposed to EtOH vapor, the much higher adsorption velocity gives rise to the faster and greater number of induced charges in the nanorod layer than in the seed layer. The rate of resistance decrease of the nanorod layer was therefore much higher than that of the seed layer ($\{dR/dt\}_{\text{nanorods}} >> \{dR/dt\}_{\text{seed}}$). At a certain applied voltage, the induced charges in the gas sensor would preferentially transport along the nanorod layer, as shown in the schematic diagrams in Figure 3.6 a-c. The resistance variation of the nanorod layer represented that of the whole sensor. The longer nanorods will shorten the transportation routes because of the many junctions in the 3D nanorod networks. Therefore, the response time shortened considerably as the nanorod length increased, as illustrated in Figure 3.4b.

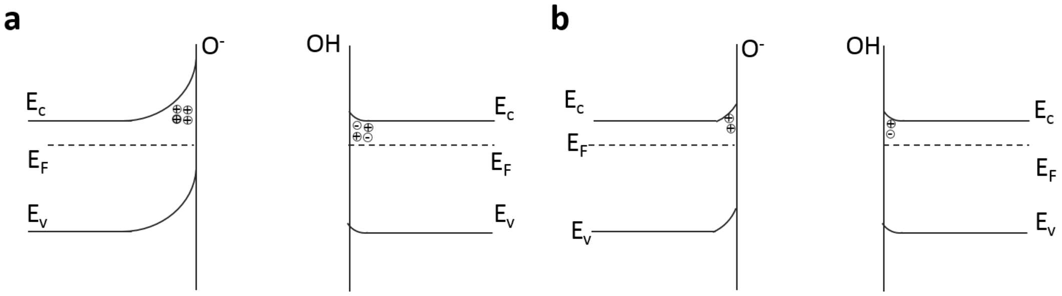

Figure 3.5 Surface energy band bending of the nanorods are higher than that of the seed layer because of their higher surface potential. (a) Surface energy band bending of nanorods when exposed to oxygen and ethanol; (b) Surface energy band bending of the seed layer when exposed to oxygen and ethanol.

When the sensor is exposed to air again, the target gas will be desorbed and oxygen would be readsorbed to recover the initial higher resistance of the sensor. For the NR-A and NR-B sensors, the surface coverage of nanorods was low. The porous random 3D nanorods with high surface potential underwent rapid desorption of EtOH vapor and readsorption of oxygen, leading to a rapid increase in resistance. In contrast, the dense seed layer with much lower surface potential would retain comparatively more remnant charges because of its slow desorption/readsorption process. The slow decrease of charge in the seed layer resulted in the slow increase of the sensor resistance, which explains the slow recovery time of the NR-A and NR-B sensors. A schematic illustration of the charge variation in the NR-A and NR-B sensor is provided in Figure 3.6 d-f. In contrast, for the NR-C and NR-D sensors, the nanorod arrays covered almost the whole surface of the sensors, unlike the cases of NR-A and NR-B, as depicted in Figure 3.2 and 3.3c. When exposed to air, the nanorod arrays would also quickly adsorb numerous oxygen ions and then deplete the charges in the nanorods. At the same time, the large oxygen density gradient between the nanorod layer and seed layer caused the oxygen to transport from the nanorod array layer to almost all the surface of the seed layer. The abundant oxygen at the surface of the seed layer would quickly deplete the charges in the seed layer, which led to the rapid increase of the resistance of the seed layer, like that of the nanorod layer. The quick depletion of charges in both the nanorod and seed layers caused the resistance of the NR-C and NR-D sensors to increase promptly when exposed to air. Schematic diagrams of the charge variation in NR-C and NR-D are shown in Figure 3.6 g-i. Overall, the sensors with higher coverage of nanorods showed a quicker recovery time, while those with a lower coverage of nanorods exhibited a slower recovery time.

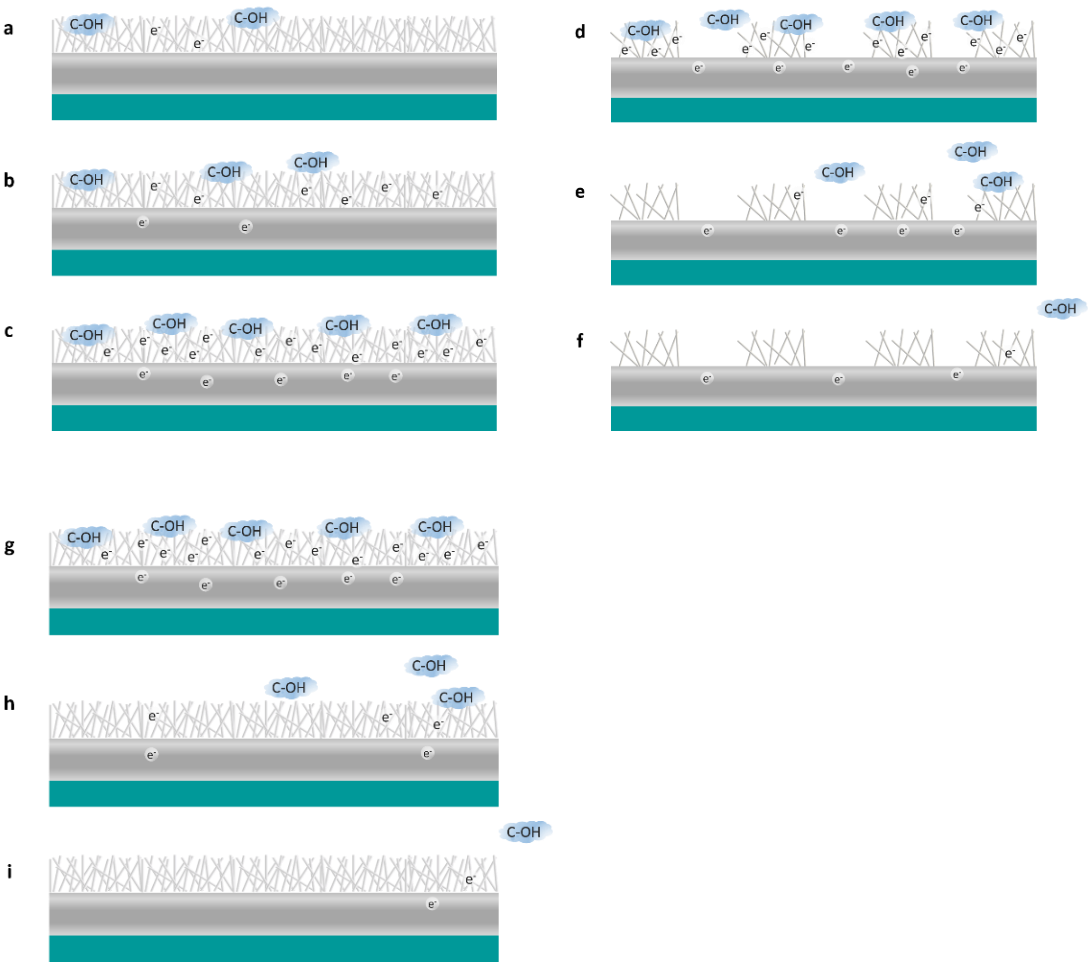

Figure 3.6 Schematic diagrams of the charge variation in the nanorod arrays when exposed to ethanol (EtOH) and oxygen: (a - c) charges generation process of the nanorods and seed layer when exposed to EtOH; (d - f) charges depletion process in NR-A and NR-B sensors, when exposed to the air; (g - j) charges depletion process in NR-C and NR-D, when exposed to air.

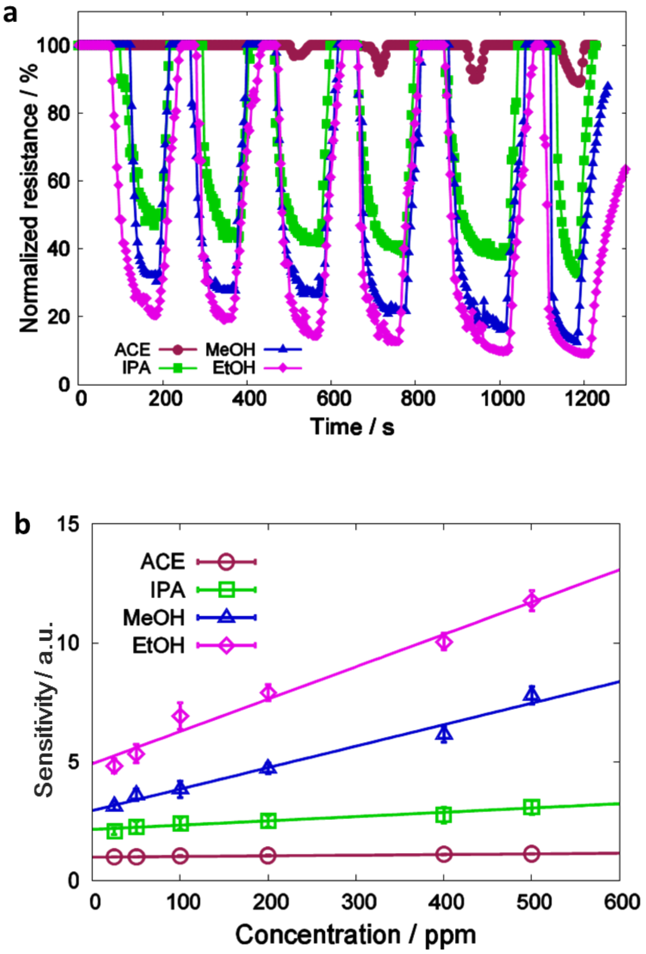

Figure 3.7 (a) Normalized resistance modulation in the NR-D gas sensor to four types of VOC vapors with different concentrations at 300 °C. (b) Sensitivity-dependent concentration of four types of VOC vapors for the NR-D sensor. Purple, blue, red and green indicate EtOH, MeOH, IPA and ACE vapors, respectively.

The above results reveal that the dependence of the response and recovery times of the sensors on different morphological factors, *i.e.*, the length and surface coverage of the nanorods, respectively, originated from the different adsorption/desorption abilities of the 3D-network of nanorods and dense seed layer. The sensitivity of the sensors was controlled by the whole surface area-to-volume ratio, *i.e.*, the integration of the length, number and area coverage of nanorods in the sensor.

To demonstrate the response of the NR-D to various gases, methanol (MeOH), ethanol (EtOH), isopropyl ethanol (IPA) and acetone (ACE) were selected as target substances to evaluate the selectivity of the NR-D sensor at 300 °C (Figure 3.7a). The NR-D sensor showed a change in resistance upon exposure to all the target vapors, and the change had different magnitudes. The largest response was to EtOH vapor, with smaller responses to MeOH, IPA and ACE vapors. The mean sensitivities of the sensor to VOC vapors at 25–500 ppm are presented in Table 3.2.

Table 3.2 Sensitivities of the α-MoO_3 nanorod arrays gas sensors to different concentrations of four gas species.

Concentration ppm	Sensitivity to ACE R_a/R_g	Sensitivity to IPA R_a/R_g	Sensitivity to MeOH R_a/R_g	Sensitivity to EtOH R_a/R_g
25	1.0	2.1	3.1	4.8
50	1.0	2.3	3.6	5.3
100	1.1	2.4	3.8	6.9
200	1.2	2.5	4.7	7.9
400	1.3	2.8	6.2	10.1
500	1.5	3.1	7.8	11.8

Figure 3.7b shows the relationship of mean sensitivity of the sensor to different concentrations of these VOC vapors. The fitting line for the sensitivity for each kind of vapor was plotted using the least squares method. The sensitivities of the sensor increase linearly with concentrations of all the VOC vapors. At any determined concentration of VOC vapors, the sensor showed sensitivities with a decreasing order of EtOH > MeOH > IPA > ACE vapor. The sensor was about 8 times more sensitive to EtOH than MeOH. It shows the same sensitivity of 4.8 for 25 ppm EtOH and 200 ppm MeOH. The sensor demonstrated 20 times higher sensitivity for MeOH than IPA, with

the same sensitivity of 3.1 for 25 ppm MeOH and 500 ppm IPA. These results indicate that the sensor possessed good discrimination of the four kinds of VOC vapors at any concentration, which represents one of the most important characteristics as gas sensors.

The ability of the α-MoO_3 nanorod arrays sensor to discriminate among VOC vapors can be attributed to the different abilities of these vapors to decrease resistance and undergo adsorption/desorption. The discrimination of alcohols (EtOH, MeOH and IPA) from ACE vapor results from the lattice oxygen at the MoO_3 surface layer preferentially oxidizing the hydroxyl group of the alcohols into the carbonyl group of a ketones through a catalytic process, as shown in equation 3.6. As for the distinction of the three kinds of alcohol, the lower reduction ability of IPA will lead to lower sensitivity than those for EtOH and MeOH, because EtOH and MeOH molecules contain fewer carbon atoms than IPA. The higher sensitivity of the sensor to EtOH than MeOH could probably result from the different adsorption ability of the nanorods for EtOH and MeOH. The nanorod arrays showed the same sensitivity (about 4.8) for 25 ppm EtOH and 200 ppm MeOH, which suggests that the nanorods can adsorb EtOH vapor 8 times more readily than MeOH vapor.

3.2.3 Mechanism of gas sensing process of α-MoO_3 nanorod arrays to VOCs

On the basis of the experimental results and the reported mechanism of nano-structured MoO_3, a reasonable gas sensing mechanism for the 3D hierarchical MoO_3 nanorod arrays structure was proposed. Figure 3.8a–c presents schematic diagrams of the gas sensing mechanism of the MoO_3 nanorod arrays. The gas sensing mechanism of MoO_3 involves initial state (Figures 3.8a-1), adsorption state (Figures 3.8a and 3.8a-2), reduction state (Figures 3.8b and 3.8b-1,-2), desorption state (Figure 3.8c), and oxidation state (Figures 3.8c and 3.8c-1) processes.

Different from other typical metal oxide semiconductors (SnO_2 or ZnO), the gas detection process of MoO_3 dominated mainly by the surface lattice oxygen rather than the chemisorbed oxygen, as shown in the schematic Figure 3.8a. Alsaif *et al*, [46, 47] pointed that hydrogen ions etc. can be intercalated into van der Waals's gaps of α-MoO_3, accompanied with the lower oxidation state. As confirmed in Chapter 2, the orientation direction of the ultra-fine nanorods in this work is [100][39]. The (010) facet lies in the side of the nanorods, which is very readily for the intercalation of H^+ ions, as shown in Figures 3.8a and 3.8a-2. When the VOCs, *e.g.* EtOH, were adsorbed onto the surface of the MoO_3 nanorod arrays, the O-H bond of the adsorbed EtOH dissociated heterolytically to yield ethoxide groups and hydrogen as follows [48].

$$C_2H_5OH_{(ads)} \rightarrow C_2H_5O^-_{(ads)} + H^+_{(ads)} \tag{3.2}$$

Subsequently, the H^+ ions will spill over the (010) plane of the MoO_3 [49-51], are then interact with the lattice corner-sharing oxygen atoms, forming the theoretical OH_2 groups and H_xMoO_3 structures. At elevated operating temperatures, H_2O molecules are eventually formed, through leaving the oxygen vacancies, i.e. MoO_{3-x}. Each of the possible reactions was described by the following reactions and schematic of Figures 3.8a-2 and 3.8b-1, respectively.

$$MoO_3 + xH^+ + xe^- \rightarrow H_xMoO_3 \tag{3.3}$$

$$2H_xMoO_3 \rightarrow xH_2O + 2MoO_{3-x/2} \tag{3.4}$$

Besides the H^+ ion intercalation, the ethoxide groups $C_2H_5O^-$ can form an ionic bond with the unsaturated metal site. The adsorbed hydroxyl groups then undergo dehydrogenation with subsequent proton donation to the cation, due to the reducible cationic nature of Mo, as illustrated in equation (3.5, 3.6) [52]

$$C_2H_5O_{(ads)} + H_{(ads)} + \text{-O-Mo-O-Mo} \rightarrow \text{-OH}_{(ads)} + C_2H_5\text{O-Mo-O-Mo} \tag{3.5}$$

$$C_2H_5\text{O-Mo-O-Mo} \rightarrow CH_3CHO + \text{Mo-O-Mo-H} \tag{3.6}$$

The acetaldehyde undergoes subsequent oxidation to form H_2O and CO_2. The adsorbed hydroxyl groups are assumed to be desorbed as H_2O, leaving a surface oxygen vacancy, shown in Figure 3.8b and 3.8b-2.

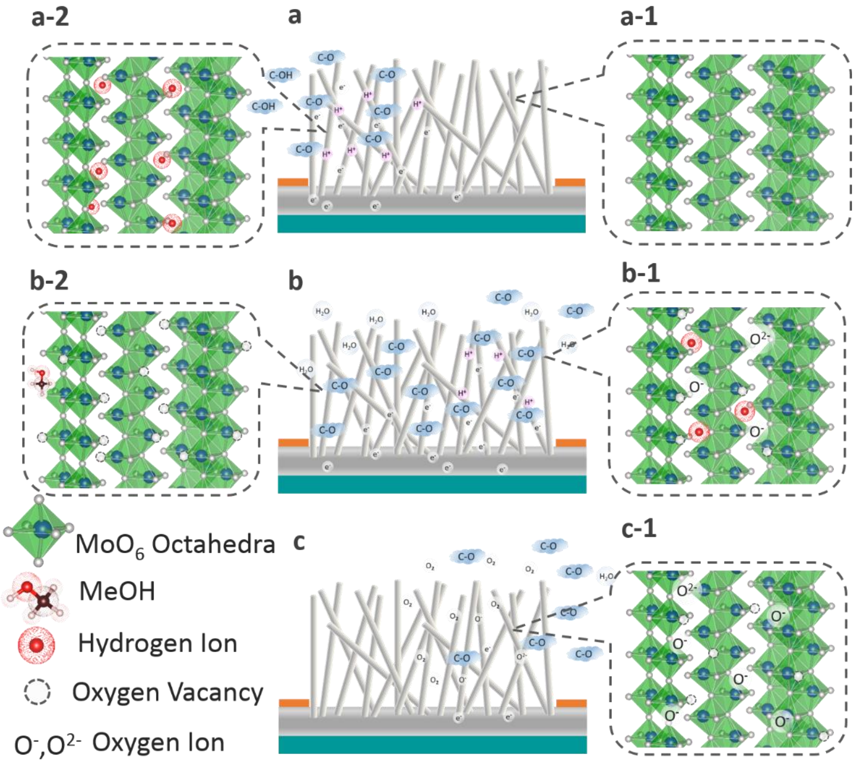

Figure 3.8 Schematic diagrams illustrating the mechanism of the gas sensing process of the α-MoO_3 nanorod arrays gas sensors detecting alcoholic vapors: a and a-1. initial state of the MoO_3 nanorod arrays, a and a-2. beginning of the adsorption state the MoO_3 nanorod arrays to VOCs, the hydrogen decomposed from VOCs intercalated into the van de Waals's gaps of layered α-MoO_3; b. reduction state of the MoO_3 nanorod arrays, b-1. MoO_3 was reduced by the intercalated hydrogen reacting with cornered oxygen into H_2O and non-stoichiometric MoO_{3-x}, b-2. oxygen defects at the surface and inter-layer of the MoO_3 nanorod arrays resulted from the remained the ethoxide group; c and c-1 desorption process to the VOCs and reoxidation process when air reflowed onto the surface of the MoO_3 naonrod arrays.

When the 3D-network nanorod arrays were exposed to air again, the reduced film surface returned to its original fully oxidized state, shown in Figure 3.8c and 3.8c-1, as described in the equation (3.7):

$$(x/4)O_2 + MoO_{3-x/2} \rightarrow MoO_3 \tag{3.7}$$

The MoO_3 nanorod arrays were involved in the whole gas sensing process; for instance, the adsorption/desorption of oxygen and VOC vapors, the interaction with the VOC vapors, and oxygen vacancy transportation. When exposed to different types of VOC vapors, different amounts of vacancies formed at the surface of the nanorods. The resulting vacancy gradient led to different amounts of oxygen anions being transported from the seed layer to the nanorod arrays to give different contents of induced carriers. In this work, the more numerous and quickly induced carriers in the seed layers observed for EtOH vapor > MeOH vapor > IPA vapor > ACE vapor resulted from the different adsorption and reduction abilities of these vapors.

3.3 Conclusion

In summary, a prototype alcoholic gas analysis device made from α-MoO_3 nanorod arrays was developed. The ultrafine α-MoO_3 nanorod arrays with 3D network structures were synthesized by a simple sol–gel route. Gas sensing performance for VOC vapors were quantitatively studied by adjusting the specific nanostructures of the nanorod arrays. The 3D nanorod arrays showed excellent sensitivity and discrimination of the various vapors at 300 ^{o}C, with considerable dependence on the structure of the 3D network nanorod arrays. The hydrogen decomposed from VOCs intercalated into the van de Waals's gaps of layered α-MoO_3 which subsequently was reduced by the hydrogen reacting with cornered oxygen into H_2O, and the remained ethoxide group resulted in the conductance of the oxygen defect non-stoichiometric MoO_{3-x}. The sensor with more numerous and longer nanorods showed a larger and quicker response to the

VOC vapors than that of the sensors with fewer and shorter nanorods. The different morphological factors dominated the different facets of the sensing performance, illustrating that the 3D nanorod arrays possessed much stronger adsorption ability than the underlying dense seed layer, which was attributed to their different active sites and surface potential. The development of gas sensors based on α-MoO_3 nanorod arrays with the ability to functionally control morphology opens the door to realize a low-power-consumption, low-cost fabrication process for VOC gas sensors.

Reference

[1] Wu T, Zhang X, Yuan Q, Xue J, Lu G, Liu Z, Wang H, Wang H, Ding F, Yu Q. Fast growth of inch-sized single-crystalline graphene from a controlled single nucleus on Cu-Ni alloys. Nat. Mater. 2016;15:43.

[2] Kraemer D, Poudel B, Feng H-P, Caylor JC, Yu B, Yan X, Ma Y, Wang X, Wang D, Muto A. High-performance flat-panel solar thermoelectric generators with high thermal concentration. Nat. Mater. 2011;10:532.

[3] Kravets V, Schedin F, Jalil R, Britnell L, Gorbachev R, Ansell D, Thackray B, Novoselov K, Geim A, Kabashin AV. Singular phase nano-optics in plasmonic metamaterials for label-free single-molecule detection. Nat. Mater. 2013;12:304.

[4] Pust P, Schmidt PJ, Schnick W. A revolution in lighting. Nat. Mater. 2015;14:454.

[5] Mannsfeld SC, Tee BC, Stoltenberg RM, Chen CVH, Barman S, Muir BV, Sokolov AN, Reese C, Bao Z. Highly sensitive flexible pressure sensors with microstructured rubber dielectric layers. Nat. Mater. 2010;9:859.

[6] Beekman M, Morelli DT, Nolas GS. Better thermoelectrics through glass-like crystals. Nat. Mater. 2015;14:1182.

[7] McAlpine MC, Ahmad H, Wang D, Heath JR. Highly ordered nanowire arrays on plastic substrates for ultrasensitive flexible chemical sensors. Nat. Mater. 2007;6:379.

[8] Ho GW. Gas sensor with nanostructured oxide semiconductor materials. Science of Advanced Materials 2011;3:150.

[9] Arafat M, Dinan B, Akbar SA, Haseeb A. Gas sensors based on one dimensional nanostructured metal-oxides: a review. Sensors 2012;12:7207.

[10] Jimenez-Cadena G, Riu J, Rius FX. Gas sensors based on nanostructured materials. Analyst 2007;132:1083.

[11] Wang X, Sun X, Hu PA, Zhang J, Wang L, Feng W, Lei S, Yang B, Cao W. Colorimetric sensor based on self-ssembled Polydiacetylene/graphene-stacked composite film for vapor-phase volatile organic compounds. Adv. Funct. Mater. 2013;23:6044.

[12] Dasgupta NP, Sun J, Liu C, Brittman S, Andrews SC, Lim J, Gao H, Yan R, Yang P. 25th anniversary article: semiconductor nanowires–synthesis, characterization, and applications. Advanced Materials 2014;26:2137.

[13] Stubhan T, Ameri T, Salinas M, Krantz J, Machui F, Halik M, Brabec CJ. High shunt resistance in polymer solar cells comprising a MoO_3 hole extraction layer processed from nanoparticle suspension. Appl. Phys. Lett. 2011;98:253308.

[14] Girotto C, Voroshazi E, Cheyns D, Heremans P, Rand BP. Solution-processed MoO_3 thin films as a hole-injection layer for organic solar cells. ACS applied materials & interfaces 2011;3:3244.

[15] Hadipour A, Cheyns D, Heremans P, Rand BP. Electrode considerations for the optical enhancement of organic bulk heterojunction solar cells. Adv. Energy Mater. 2011;1:930.

[16] Wang T-S, Wang Q-S, Zhu C-L, Ouyang Q-Y, Qi L-H, Li C-Y, Xiao G, Gao P, Chen Y-J. Synthesis and enhanced H_2S gas sensng properties of α-MoO_3/CuO p–n junction nanocomposite. Sensors and Actuators B: Chemical 2012;171:256.

[17] Bai S, Chen S, Chen L, Zhang K, Luo R, Li D, Liu CC. Ultrasonic synthesis of MoO_3 nanorods and their gas sensing properties. Sensors and Actuators B: Chemical 2012;174:51.

[18] Zhao X, Cao M, Hu C. Thermal oxidation synthesis hollow MoO_3 microspheres and their applications in lithium storage and gas-sensing. Mater. Res. Bull. 2013;48:2289.

[19] Chen Y, Meng F, Ma C, Yang Z, Zhu C, Ouyang Q, Gao P, Li J, Sun C. In situ diffusion growth of $Fe_2(MoO_4)_3$ nanocrystals on the surface of α-MoO_3 nanorods with significantly enhanced ethanol sensing properties. J. Mater. Chem. 2012;22:12900.

[20] Sui L, Song X, Cheng X, Zhang X, Xu Y, Gao S, Wang P, Zhao H, Huo L. An ultraselective and ultrasensitive TEA sensor based on α-MoO_3 hierarchical nanostructures and the sensing mechanism. Crystengcomm 2015;17:6493.

[21] Yamazaki T, Jin C, Nakayama A, Ito K, Yoshizawa T, Kikuta T, Nakatani N, Yamabuchi T. NO_2 gas sensor made of porous MoO_3 sputtered films. Japanese journal of applied physics 2005;44:792.

[22] Xing L-L, Yuan S, Chen Z-H, Chen Y-J, Xue X-Y. Enhanced gas sensing performance of $SnO_2/\alpha\text{-}MoO_3$ heterostructure nanobelts. Nanotechnology 2011;22:225502.

[23] Sui L-l, Xu Y-M, Zhang X-F, Cheng X-L, Gao S, Zhao H, Cai Z, Huo L-H. Construction of three-dimensional flower-like $\alpha\text{-}MoO_3$ with hierarchical structure for highly selective triethylamine sensor. Sensors and Actuators B: Chemical 2015;208:406.

[24] Zeng W, Zhang H, Li Y, Chen W. Net-like MoO_3 porous architectures: synthesis and their sensing properties. Journal of Materials Science: Materials in Electronics 2014;25:338.

[25] Illyaskutty N, Kohler H, Trautmann T, Schwotzer M, Pillai VM. Enhanced ethanol sensing response from nanostructured MoO_3: ZnO thin films and their mechanism of sensing. J. Mater. Chem. C 2013;1:3976.

[26] Yu J, Ippolito S, Shafiei M, Dhawan D, Wlodarski W, Kalantar-zadeh K. Reverse biased Pt/nanostructured MoO_3/SiC Schottky diode based hydrogen gas sensors. Appl. Phys. Lett. 2009;94:3504.

[27] Wang C, Yin L, Zhang L, Xiang D, Gao R. Metal oxide gas sensors: sensitivity and influencing factors. Sensors 2010;10:2088.

[28] Ma S, Li R, Lv C, Xu W, Gou X. Facile synthesis of ZnO nanorod arrays and hierarchical nanostructures for photocatalysis and gas sensor applications. Journal of hazardous materials 2011;192:730.

[29] Wen Z, Zhu L, Mei W, Hu L, Li Y, Sun L, Cai H, Ye Z. Rhombus-shaped Co_3O_4 nanorod arrays for high-performance gas sensor. Sensors and Actuators B: Chemical 2013;186:172.

[30] Lupan O, Chai G, Chow L. Fabrication of ZnO nanorod-based hydrogen gas nanosensor. Microelectronics Journal 2007;38:1211.

[31] Tian S, Yang F, Zeng D, Xie C. Solution-processed gas sensors based on ZnO nanorods array with an exposed (0001) facet for enhanced gas-sensing properties. The Journal of Physical Chemistry C 2012;116:10586.

[32] Yao K, Toole R, Basnet P, Zhao Y. Highly sensitive double-layered nanorod array gas sensors prepared by oblique angle deposition. Appl. Phys. Lett. 2014;104:073110.

[33] Vallejos S, Stoycheva T, Umek P, Navio C, Snyders R, Bittencourt C, Llobet E, Blackman C, Moniz S, Correig X. Au nanoparticle-functionalised WO_3 nanoneedles and their application in high sensitivity gas sensor devices. Chemical Communications 2011;47:565.

[34] Zhou J, Xu NS, Deng SZ, Chen J, She JC, Wang ZL. Large-area nanowire arrays of molybdenum and molybdenum oxides: synthesis and field emission properties. Advanced Materials 2003;15:1835.

[35] Liu C, Li Z, Zhang Z. Growth of [010] oriented α-MoO_3 nanorods by pulsed electron beam deposition. Appl. Phys. Lett. 2011;99:223104.

[36] Navas I, Vinodkumar R, Lethy K, Detty A, Ganesan V, Sathe V, Pillai VM. Growth and characterization of molybdenum oxide nanorods by RF magnetron sputtering and subsequent annealing. Journal of Physics D: Applied Physics 2009;42:175305.

[37] Meduri P, Clark E, Kim JH, Dayalan E, Sumanasekera GU, Sunkara MK. MoO_{3-x} nanowire arrays as stable and high-capacity anodes for lithium ion batteries. Nano Lett. 2012;12:1784.

[38] Zheng L, Xu Y, Jin D, Xie Y. Well-aligned molybdenum oxide nanorods on metal substrates: solution-based synthesis and their electrochemical capacitor application. J. Mater. Chem. 2010;20:7135.

[39] Cong S, Sugahara T, Wei T, Jiu J, Hirose Y, Nagao S, Suganuma K. Growth and extension of one-step sol–gel derived molybdenum trioxide nanorods via controlling citric acid decomposition rate. Cryst. Growth Des. 2015;15:4536.

[40] Suganuma K, Sakamoto S, Kagami N, Wakuda D, Kim K-S, Nogi M. Low-temperature low-pressure die attach with hybrid silver particle paste. Microelectronics Reliability 2012;52:375.

[41] Chen D, Liu M, Yin L, Li T, Yang Z, Li X, Fan B, Wang H, Zhang R, Li Z. Single-crystalline MoO_3 nanoplates: topochemical synthesis and enhanced ethanol-sensing performance. J. Mater. Chem. 2011;21:9332.

[42] Hu Y, Zhou J, Yeh PH, Li Z, Wei TY, Wang ZL. Supersensitive, fast-response nanowire sensors by using schottky contacts. Advanced Materials 2010;22:3327.

[43] Wen Z, Zhu L, Li Y, Zhang Z, Ye Z. Mesoporous Co_3O_4 nanoneedle arrays for high-performance gas sensor. Sensors and Actuators B: Chemical 2014;203:873.

[44] Rath J, Agarawalla S, Roy G. Principles of Gas Sensing Application of metal oxide semiconductor devices.

[45] Qin G, Gao F, Jiang Q, Li Y, Liu Y, Luo L, Zhao K, Zhao H. Well-aligned Nd-doped SnO_2 nanorod layered arrays: preparation, characterization and enhanced alcohol-gas sensing performance. Physical Chemistry Chemical Physics 2016;18:5537.

[46] Alsaif MM, Balendhran S, Field MR, Latham K, Wlodarski W, Ou JZ, Kalantar-zadeh K. Two dimensional α-MoO_3 nanoflakes obtained using solvent-assisted grinding and sonication method: Application for H_2 gas sensing. Sensors and Actuators B: Chemical 2014;192:196.

[47] Alsaif MM, Chrimes AF, Daeneke T, Balendhran S, Bellisario DO, Son Y, Field MR, Zhang W, Nili H, Nguyen EP. High-performance field effect transistors using electronic inks of 2d molybdenum oxide nanoflakes. Adv. Funct. Mater. 2016;26:91.

[48] Wang L, Gao P, Bao D, Wang Y, Chen Y, Chang C, Li G, Yang P. Synthesis of crystalline/amorphous core/shell MoO_3 composites through a controlled dehydration route and their enhanced ethanol sensing properties. Cryst. Growth Des. 2014;14:569.

[49] Xie W, Su M, Zheng Z, Wang Y, Gong L, Xie F, Zhang W, Luo Z, Luo J, Liu P. Nanoscale insights into the hydrogenation process of layered α-MoO_3. ACS Nano 2015;10:1662.

[50] Greiner MT, Chai L, Helander MG, Tang WM, Lu ZH. Transition metal oxide work functions: the influence of cation oxidation state and oxygen vacancies. Adv. Funct. Mater. 2012;22:4557.

[51] Battaglia C, Yin X, Zheng M, Sharp ID, Chen T, McDonnell S, Azcatl A, Carraro C, Ma B, Maboudian R. Hole selective MoO_x contact for silicon solar cells. Nano Lett. 2014;14:967.

[52] Illyaskutty N, Kohler H, Trautmann T, Schwotzer M, Pillai VPM. Enhanced ethanol sensing response from nanostructured MoO_3:ZnO thin films and their mechanism of sensing. J. Mater. Chem. C 2013;1:3976.

Chapter 4

Solution processed molybdenum oxide buffer layer for organic solar cell

Abstract

Molybdenum oxide (MoO_x) films show great potential in various electrical devices via displaying diversity of valence state of Mo cation. In this work, a simple and mild sol–gel route was developed for the synthesis of MoO_x hole transport layers (HTLs) for the organic solar cells (OSCs) to substitute the traditional vapor process of MoO_x film, which restricts the fabrication of OSCs in large-scale and low-cost. The oxygen vacancy and valence of the molybdenum in the MoO_x HTLs can be well controlled as high conductivity, transparency and well-aligned band structure with the HOMO of the active layer by introducing and adjusting the amount of the hydrogen peroxide (H_2O_2) in the precursors. The molar ratio of Mo to citric acid in the precursor solution and annealing temperature also play important roles and were optimized as Mo:citric=0.025:0.075 mol/l, and 200 ºC to fabricate the more efficient solar cells. The performance of the OSCs containing this solution-processed MoO_x HTL is comparable with that of the reference devices with the evaporated MoO_x HTLs or the poly (3,4-ethylenedioxythiohene):poly(styrenesulfonate) (PEDOT:PSS) HTLs. HTL from this route are very promising for universal application of variety of solar cell, and provide valuable insight for the production of fast, large-scale, low-cost and simple synthesis of renewable energy.

4.1 Introductrion

Interesting electrical properties of Molybdenum oxide ($MoO_{x,}$) [1-4], recently, are attracting more and more attention from the material and the device researchers, because the semiconductor state of p- and n-type are existence with different material synthesis and device fabrication processing of MoO_x [5-7]. The crystal structure of MoO_x displays variety phases such as alpha-, beta- and h-phases of MoO_3 with wide range of the oxygen stoichiometry (e.g., $Mo_{18}O_{52}$, Mo_9O_{26}, Mo_8O_{23}, Mo_5O_{14}, $Mo_{17}O_{47}$, Mo_4O_{11}, and MoO_2) and valence state (e.g. 4+, 5+, 6+ etc.) of Mo cation, which makes molybdenum oxide's physical properties controllable from insulator to metal by changing band structure, density of states and band gap[8, 9]. Moreover, the Femi level can also change with the doping of different deponents, such as Sr [10], Al [11] (n-type) and In (p-type) [12] allow for the development of modified carrier density and conduction type, meaning tunable charges transport ability for various electronics devices. In such background, the MoO_x can be used as buffer layer e.g. electron transport layer (ETL) and hole transport layer (HTL) for the organic electronics devices, which have been steadily evolving and have begun to penetrate the mainstream consumer electronics market [13-17]. In particular, MoO_x are used for the photo voltaic solar cells due to its adjustable properties of work function, band gap (3.1-3.8 eV), lowest unoccupied molecular orbital (LUMO), and highest occupied molecular orbital (HOMO) level with coating processing by band gap engineering with high transparency (> 80 %) in the visible and near IR range [18-22].

Nowadays, homogenous and smooth MoO_x HTLs have been fabricated with vapor process (eMoO_x) and demonstrated as high performance being applied into organic solar cells (OSCs) [23-25]. However, the vapor process is time-consuming and very sensitive to the contaminations [26], which increase the manufacturing cost of the organic solar cell and incompatible with the large-area processing of flexible OSCs. In addition, the evaporation process showed the handicap that severe loss of oxygen in the oxide, which will change its energy levels, lower its work function and make it less suitable for extracting holes from the active layer [27].

Recently, the solution processed MoO_x ($sMoO_x$) interfacial HTLs are widely preferred to fulfill the requirements of the entire solution processed OSCs with the simplified device fabrication process. Several routes for the $sMoO_x$ HTLs have been reported by virtue of precise composition control, high homogeneity, large area, flexible, and low processing cost [28-30]. However, the solution-processed MoO_x HTLs are still facing several challenges in fabricating the efficient OSCs. One of the difficulties is to control the stoichiometry of oxygen and Mo within the intrinsic oxide using a simple annealing process, which is required to optimize the annealing temperature to convert the precursors to MoO_x to fabricate oxide HTL with abundant polyvalence and high work function [31-34].

Hydrogen peroxide (H_2O_2) is a strong oxidizer, which can be used to control the oxidation state of the oxides though simple solution process. Choy et al, [10, 35] developed a solution process for the efficient MoO_x HTLs by using H_2O_2 as the solvents to dissolve the metallic Mo into the water, which demonstrated that the H_2O_2 can effectively control the stoichiometry of Mo and oxygen in the MoO_x HTLS. However, this dissolving process will also introduce more excessive oxygen vacancies to lower the work function and is a violently exothermic oxidation reaction, which needs to be processed with further step to lower the reaction temperature. Very recently, a much more mild H_2O_2-based process for the $sMoO_x$ HTLs were developed by our group [36]. The smooth and more conductive $sMoO_x$ HTLs were fabricated and a better performance of the OSCs were achieved, which show a light for achieving the solution-processed MoO_x HTLs with a simple annealing process. However, the function of the H_2O_2 for fabricating the HTLs is still far away from entirely clear.

In this work, a mild route for the H_2O_2-disposed $sMoO_x$ HTLs was developed with a modified recipe from our previous work [36-38]. The corresponding HTLs and the referential $eMoO_x$ or PEDOT:PSS HTLs was used to fabricate the OSCs. This $sMoO_x$ HTLs were recently testified by our group as very promising for the CZTSe-based solar cells [39], which requires the high temperature and corrosive environment. Here the material properties of this sMoO$_x$ HTLs were focused on, by trying to analyze the function of H_2O_2 in the precursors and by examining the hole transport abilities for the OSCs. A detailed study to understand the evolution of their structural, chemical, and electronic properties of the sMoO$_x$ were carried out. The knowledge garnered from this study will greatly contribute to the research and development universal applications for the organic electronic devices by using the solution coated MoO$_x$ buffer layer (or HTLs).

4.2 Experimental

4.2.1 Fabrication process of sMoO$_x$ based thin films

For comparison, precursor solutions with and without H_2O_2 were prepared, as shown in Figure 4.1a. The precursors without H_2O_2 were prepared using a modified procedure from that in our previous work [37, 40]. Ammonium molybdate (97.0 %, Sigma-Aldrich, Germany) and citric acid (anhydrous, 98.0 %, Sigma-Aldrich) were dissolved in 2-methoxyethanol (5 mL, Sigma-Aldrich) with a ratio of 0.025:0.075 mol/L, by magnetic stirring for 4h and then the solution was aged for 24 h in air. This solution was defined as (A). The precursor with H_2O_2 was prepared as A, except H_2O_2 (30 wt.%, Sigma-Aldrich) was added to 2-methoxyethanol to give a total volume of 5 mL with a volume ratio of H_2O_2 to 2-methoxyethanol of 10:90 (vol.%). This solution was defined as solution (B). After adding H_2O_2 into the precursor solution, it instantly changed from faint to bright yellow, as shown in the inset of Figure 1(c) and (d). This suggested that the valence of the Mo ions in the solution changed from +5 to +6 and Mo octahedral formed [36].

4.2.2 Fabrication process of organic solar cells based on sMoO$_x$ HTLs

To fabricate sMoO$_x$ HTLs, patterned ITO substrates were first cleaned with detergent, and then sequentially sonicated in deionized water, acetone, and isopropyl alcohol for 10 min. The ITO substrates were further cleaned by UV/ozone treatment to improve their wettability for the solutions. The Mo solutions with and without H_2O_2 were then spin coated on the precleaned ITO substrates at 1000 rpm for 30 s, as shown in Figure 4.1b. Subsequently, these samples were annealed on a preheated hotplate at about 200 °C for 10 min in air to make the solution-processed MoO_x-based HTLs, as shown in Figure 4.1c. Films synthesized without and with H_2O_2 were defined as $sMoO_x$_A and $sMoO_x$_B, respectively. For comparison, 25 nm-thick spin-coated PEDOT:PSS (Heraeus Clevios 4083, Heraeus, USA) and 20 nm-thick $eMoO_x$ layers were also fabricated on clean ITO substrates as HTLs to compare with the solution-processed MoO_x HTLs. The PEDOT:PSS HTLs were annealed at 110 °C in air.

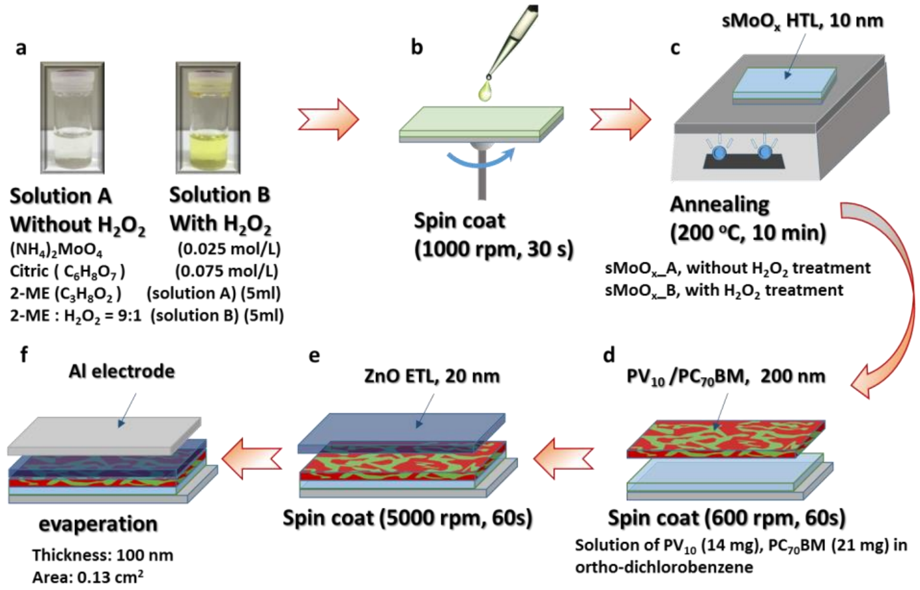

Figure 4.1 Fabrication process of organic solar cells based on solution processed hole transport layer.

PV_{10} (14 mg, Polyera, USA) and $PC_{70}BM$ (21 mg, Nano-C, USA) were dissolved with a weight ratio of 1:1.5 in *ortho*-dichlorobenzene (1 mL, anhydrous, 99.0 %, Sigma-Aldrich) by magnetic stirring at 80 °C for 24 h to form a $PV_{10}/PC_{70}BM$ blend solution. This solution was spin coated on different HTLs ($sMoO_x$_A, $sMoO_x$_B, $eMoO_x$, and

PEDOT:PSS) to form an active layer with a thickness of 200 nm, and then dried inside a nitrogen-filled glove box without any heating, as shown in Figure 4.1d. A solution-processed ZnO ETL layer with a thickness of about 20 nm was spin coated on the surface of the active layer as reported previously, as shown in Figure 4.1e. Finally, Al (100 nm) was evaporated onto the active layers through a shadow mask to define twelve devices with an area of 0.13 cm^2 on each substrate, as shown in Figure 4.1f.

4.2.3 Characterization methods of sMoO$_x$ based thin film and organic solar cells

XPS (JPS-9010, JEOL, Japan) was performed using monochromatized Mg Kα photons (1253.6 eV) with a resolution of 0.05eV and input power of 100 W (10 kV, 10 mA). Cross-sectional views of the samples were obtained by SEM (SU8020, Hitachi, Japan) at 5 kV and 10 mA. Before observation, the thin films were sputtered with Pt to minimize the electron charging and obtain clear images. The surface morphologies of the MoO$_x$-based HTLs were investigated by AFM (Nanocute, SII Nano Technology Inc., Japan) in tapping mode. The examined MoO$_x$ thin film were fabricated on silicon surfaces and annealed at 200 °C for 10 min before imaging. The transparency of the MoO$_x$-based films was measured by an UV-Vis (V-670, Jasco, Japan) from 200–900 nm with a resolution of 2 nm. The photovoltaic characteristics of devices were measured under a nitrogen atmosphere inside a glove box using a source meter (2602A, Keithley, USA) and solar simulator (Sun 3000, Abet, USA) with 100 mW/cm^2 AM 1.5G illumination.

4.3 Results and discussion

4.3.1 Characterization of solution processed MoO$_x$ thin films

Figure 4.2a and b show cross-sectional scanning electron microscopy (SEM) images of sMoO$_x$_A and sMoO$_x$_B thin films on ITO substrates, respectively (sMoO$_x$_A is a sMoO$_x$ film fabricated without H_2O_2 and sMoO$_x$_B is a sMoO$_x$ film fabricated with H_2O_2). Both of the $sMoO_x$ films homogenously covered the surface of the substrates and had a thickness of about 10 nm. Figure 4.3 depicts the cross-sectional SEM images of OSCs with a structure of ITO/MoO_x/PV_{10}:$PC_{70}BM$/ZnO from bottom to top. The boundary of each layer can be clearly observed, especially for the interfacial ZnO ETL (~20 nm thick) and $sMoO_x$ HTL (~10 nm thick), indicating there is no interpenetration between the solution-processed layers. To further observe the surface morphology of the thin films, tapping-mode atomic force microscope (AFM) images of $sMoO_x$_A and $sMoO_x$_B on silicon substrates are presented in Figure 4.2c and d, respectively.

The $sMoO_x$ based HTLs showed the amorphous properties. The $sMoO_x$_A and $sMoO_x$_B films possessed similar surface morphology with root mean square (RMS) roughness values of 0.27 and 0.24 nm, respectively, and average roughness values of 0.21 and 0.18 nm, respectively. The smooth surfaces of both films will enhance the contact abilities to the active layer then lengthen the lifetime of photocarriers and improve the performance of OSCs [41, 42].

To determine the effect of H_2O_2 treatment on the electronic structure of the $sMoO_x$-based films, high-resolution X-ray photoelectron spectroscopy (XPS) measurements was used to study the chemical characteristics and stoichiometry of $eMoO_x$, $sMoO_x$_A and sMoOx_B, as illustrated in Figure 4.4. Survey scans were conducted from 0 to 600 eV and were calibrated by the standard peak value of carbon at 284.6 eV. The Mo 3d peaks for the three films are located at the same position. The fine peaks of Mo 3d were fitted by Gaussian–Lorentzian curves with a ratio of $3d_{5/2}$ to $3d_{3/2}$ of 3:2 and the spin orbit splitting of the Mo 3d doublets is fix at 3.13 eV. After being fitted, the MoO_x thin films mainly featured two 3d doublet Gaussian peaks centered at 232.7 and 235.8 eV. These values are close to those of the $3d_{5/2}$ and $3d_{3/2}$ Mo^{6+} oxidation states (232.8 and 235.9 eV, respectively) [34]. Two more doublets at 231.6 and 234.7 eV were identified under the main Mo^{6+} peaks, which were attributed to Mo^{5+}.

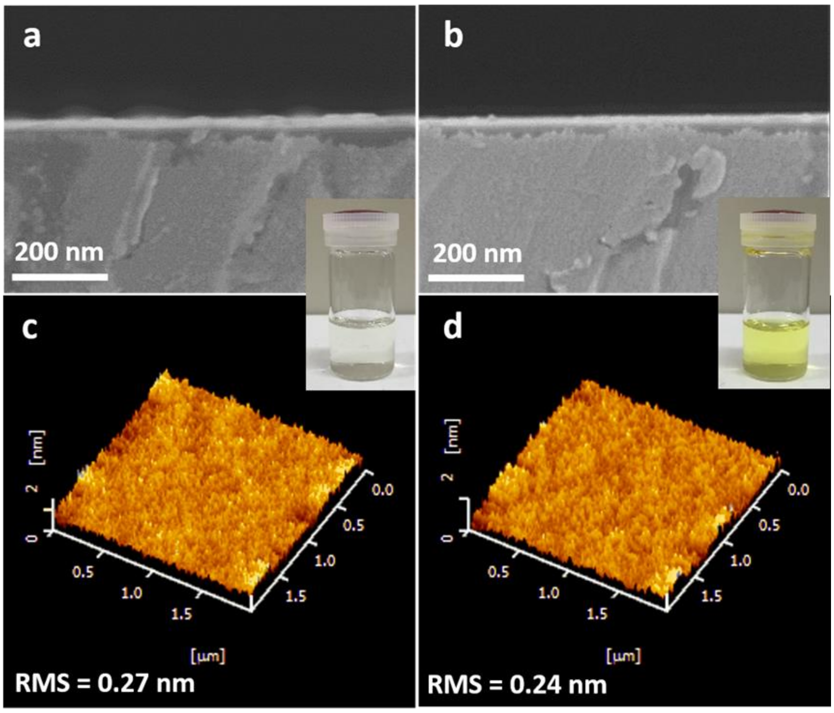

Figure 4.2 Cross-sectional SEM images of solution-processed MoO_x HTLs on ITO substrates: (a) $sMoO_x$_A, and (b) $sMoO_x$_B. AFM images of solution-processed MoO_x HTLs on silicon substrates (scan area of 2 × 2 μm): (c) $sMoO_x$_A, (inset, photograph of precursor solution without H_2O_2), and (d) $sMoO_x$_B (inset, photograph of precursor solution with H_2O_2).

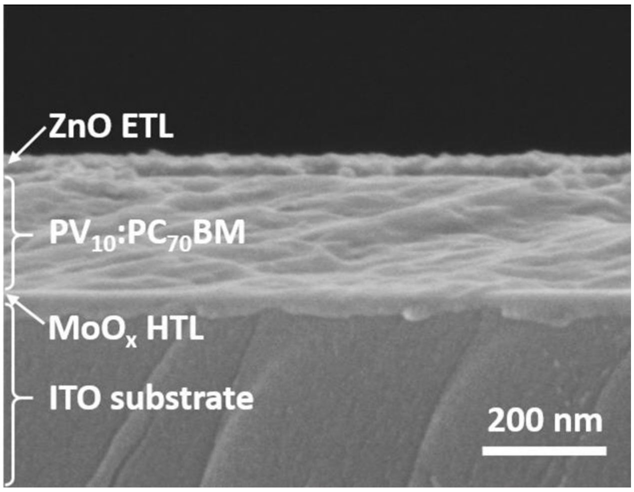

Figure 4.3 Cross-sectional SEM image of a single OSC.

The sMoO$_x$_A film exhibited almost the same peaks as eMoO$_x$, with weak Mo^{5+} peaks. The sMoO$_x$_B film showed broad peaks, which contained much more intense Mo^{5+} peaks than those of sMoO$_x$_A. The higher polyvalence of the sMoO$_x$_B film than the sMoO$_x$_A one indicated that it contained more oxygen vacancies; that is, H_2O_2 promoted the formation of oxygen vacancies. Li et al. [34] stated that oxygen vacancies modified the Fermi level and enhanced carrier transfer in thin films. Therefore, the sMoO$_x$_B film possessing more vacancies than the sMoO$_x$_A one will decrease the series resistance of the HTLs and show better performance in OSCs.

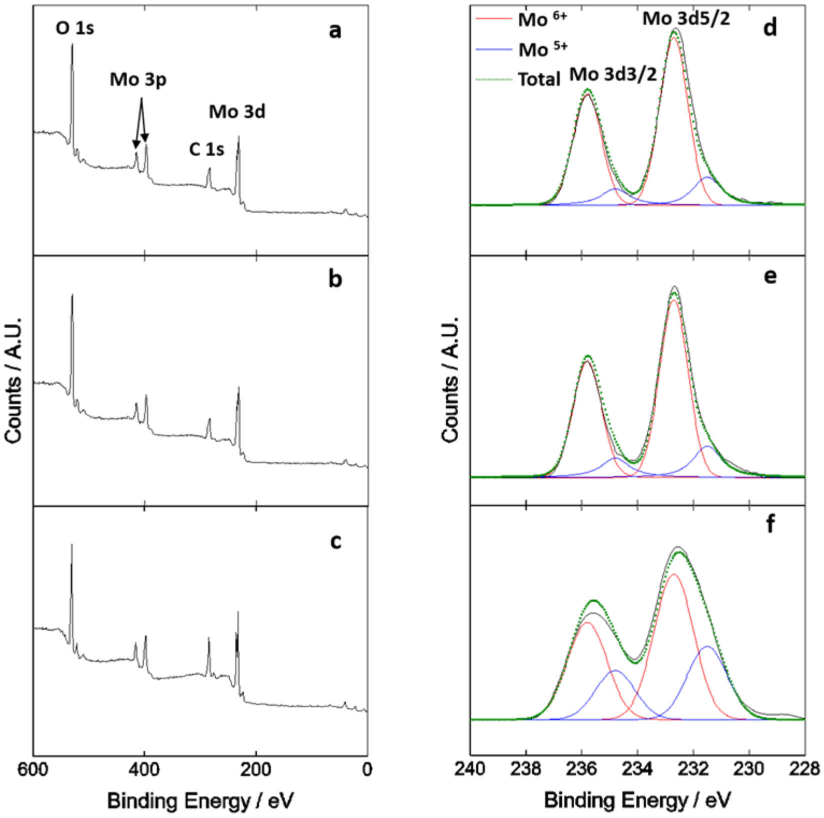

Figure 4.4 (a–c) XPS spectra wide scan spectra in scan range of 0-600 eV and (d–f) Mo 3d core-level spectra for (a), (d) eMoO$_x$, (b), (e) sMoO$_x$_A, and (c), (f) sMoO$_x$_B.

To investigate the optical properties of the MoO$_x$-based films, the ultraviolet–visible spectrophotometer light absorption and transmission spectra (UV-Vis) of the eMoO$_x$, sMoO$_x$_A and sMoO$_x$_B films on ITO substrates were measured, as shown in Figure 4.5 a.

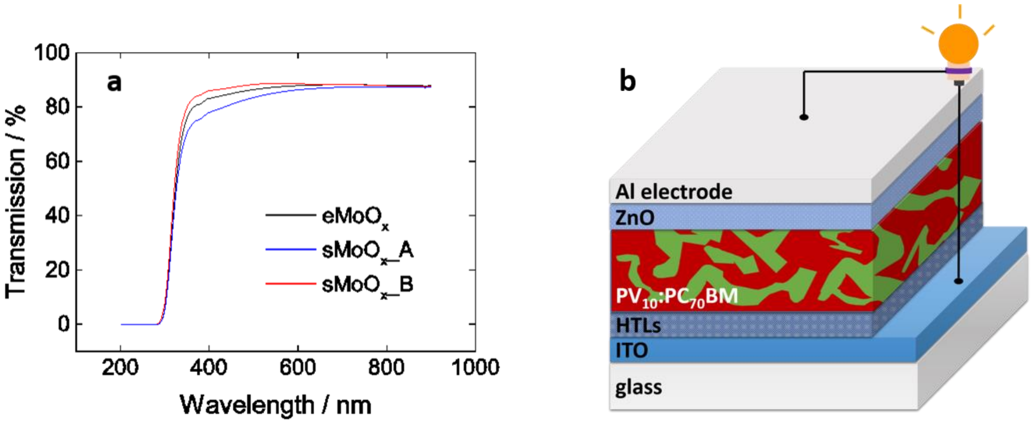

Figure 4.5 (a) Optical transmittance of eMoO$_x$, sMoO$_x$_ A, and sMoO$_x$_B HTLs on ITO substrates. (b) Schematic of the OSC layer structure used in this study.

All three films showed high transparency of > 80 % in the wavelength range of 600 – 900 nm. At the shorter wavelength range of visible light of 300 – 600 nm, the transparency of sMoO$_x$_B was about 80 %, which was a little bit higher than that of the eMoO$_x$ layer. In contrast, the transparency of sMoO$_x$_A was about 70 % in this range, suggesting undesirable optical properties. A plot obtained via transformation based on the Kubelka–Munk function versus the energy of light (Figure 4.6) reveals the estimated bandgaps of the samples to be 3.57, 3.59, and 3.61 eV, corresponding to sMoOx_A, eMoOx, sMoOx_B, respectively. The different transparencies of these three films can affect their performance as HTLs in OSCs [43].

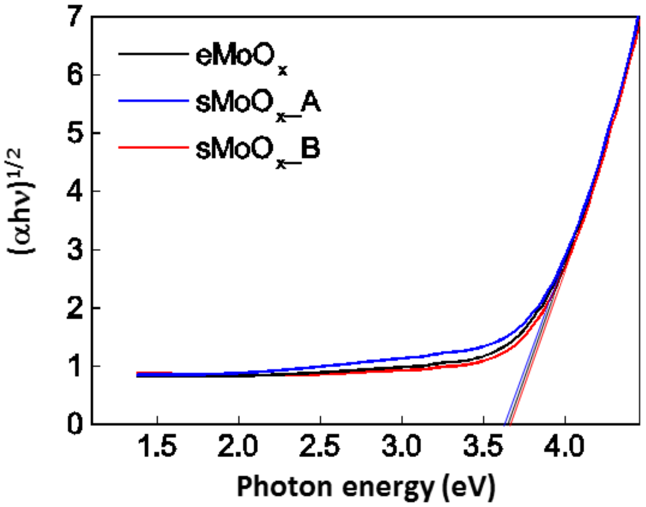

Figure 4.6 Plot of transformed Kubelka-Munk function versus energy of light.

4.3.2 Performance of OSCs based on sMoO$_x$-based HTLs

To investigate the function of the sMoO$_x$-based HTLs, OSCs with a PV$_{10}$:PC$_{70}$BM polymer/fullerene-based active layer and conventional device structure were used, as shown in Figure 4.5b. For comparison, reference devices with PEDOT:PSS or eMoO$_x$ as the interfacial layer were also fabricated. The current density–voltage (J–V) characteristics of the devices under illumination and in the dark are presented in Figure 4.7a and b, respectively. The parameters measured for the devices are summarized in Table 4.1 The external quantum efficiencies (EQEs) of the OSCs with sMoO$_x$_A and sMoO$_x$_B are shown in Figure 4.7c.

The device with sMoO$_x$_B exhibited the highest power conversion efficiency (PCE) of 7.19 %, a fill factor (FF) of 72.55 %, the highest short-circuit current density (J_{sc}) of 13.57 mA/cm^2, and a moderate open-circuit voltage (V_{oc}) of 0.73 V, as shown in Figure 4.7a. The device with sMoO$_x$_A displayed a moderate FF of 69.81 %, and the lowest PCE of the devices (6.41 %) because of its lowest V_{oc} of 0.71 V. The device containing PEDOT:PSS showed the lower PCE (7.05 %) than the sMoO$_x$_B one's even though it possessed the highest V_{oc} of 0.82 V, because it had the lowest FF of 68.26 % and J_{sc} of 12.61 mA/cm^2. Like the device with PEDOT:PSS, the device with eMoO$_x$ achieved an moderate PCE of 6.48 %, because its FF and J_{sc} were low (70.93 % and 12.51 mA/cm^2, respectively) although it showed the same V_{oc} as that of the sMoO$_x$_B device (0.73 V).

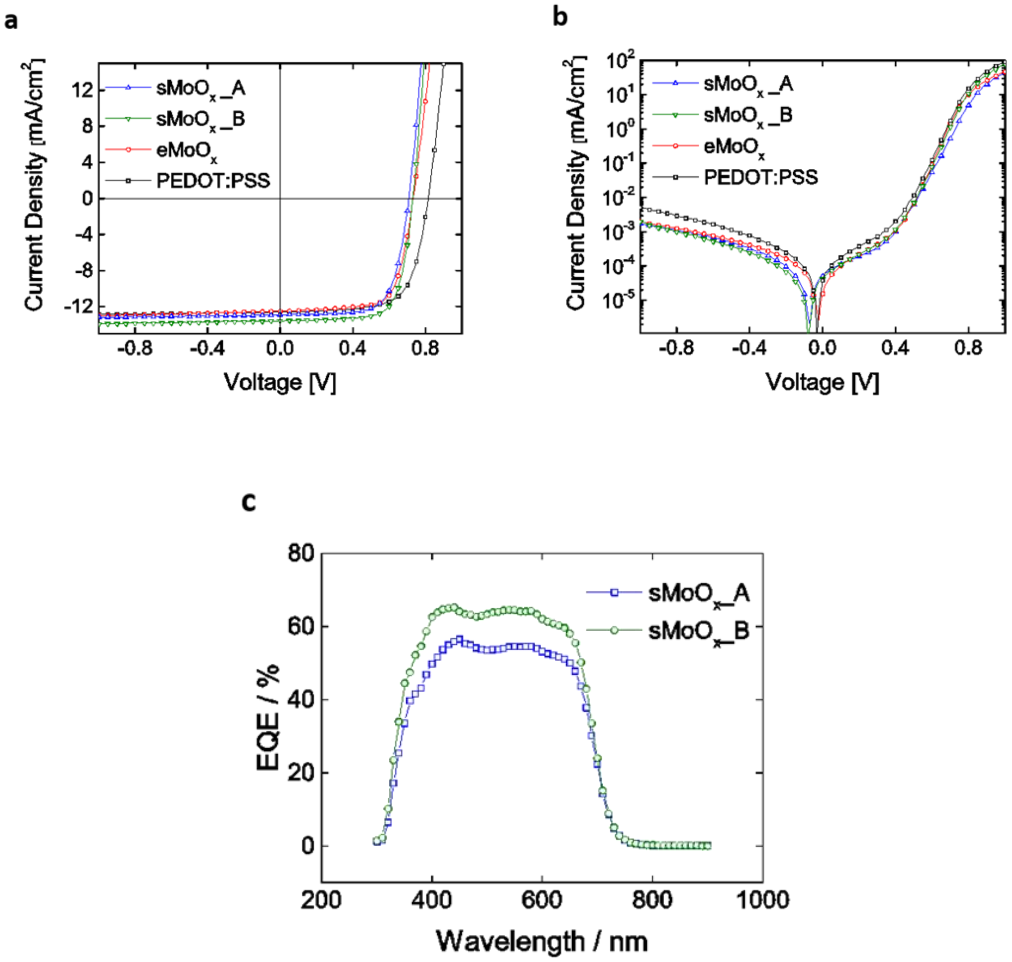

Figure 4.7 J-V curves of HTL-based OSCs (a) under illumination, and (b) in the dark. (c) EQE curves of the OSCs based on sMoO$_x$_A and sMoO$_x$_B.

The above-mentioned device characteristics were also reflected in the current curves of the devices obtained in the dark, as illustrated in Figure 4.7b. The device with a PEDOT:PSS HTL showed the highest leakage current density in both reverse and forward bias, implying poor diode properties, which coincides with its low J_{sc} and FF. Although the $sMoO_x$_B and $sMoO_x$_A devices showed almost the same low leakage current, the current density of the H_2O_2-modified HTL in forward bias was a little higher than that of the one fabricated without H_2O_2, indicating that $sMoO_x$_B possesses the lowest series resistance and thus improved performance compared with that of $sMoO_x$_A. The reverse-bias current of the $eMoO_x$-based device was higher than that of the device with $sMoO_x$_B but lower than that of the one with PEDOT:PSS. The EQE of the $sMoO_x$_B device was also much higher than that of the one with $sMoO_x$_A.

The J-V curves of the $sMoO_x$_A, $sMoO_x$_B, and $eMoO_x$-based OSCs indicate that V_{oc} of the three devices are almost the same; however, their J_{sc} values follow the order of $sMoO_x$_B > $sMoO_x$_A > $eMoO_x$. Considering the UV-Vis, XPS, AFM, J-V, and EQE results, the $sMoO_x$_B-based device exhibited the highest performance, which coincides with its high transparency throughout the visible region, high polyvalence, and smooth surface.

To optimize the OSCs with $sMoO_x$_B HTLs, the molar ratio of the Mo and citric acid in precursors was changed to 0.05:0.15 and 0.1:0.3 to study the influence of HTL thickness on device performance. The HTLs synthesized from these precursor solutions by spin coating on ITO substrates and subsequent annealing at 200 °C for 10 min were defined as $sMoO_x$_2B and $sMoO_x$_4B, respectively. The J-V curves of these OSCs are shown in Figure 4.8a. The J_{sc}, V_{oc}, FF, and PCE values of these solar cells are also listed in Table 4.1 Figure 4.8a revealed that the devices fabricated with various precursor molar ratios exhibited different performance.

The cells without a HTL showed poor performance with the lowest V_{oc}, J_{sc}, FF, and PCE of 0.14 V, 11.73 mA/cm^2, 41.08 %, and 0.67 %, respectively, indicating mismatch of energy levels at the interface between the electrode and active layer. In contrast to the device without a HTL, those with $sMoO_x$_B, $sMoO_x$_2B, and $sMoO_x$_4B HTLs showed improved performance. These three devices displayed almost the same V_{oc} of about 0.7 eV. Meanwhile, J_{sc} decreased with the increasing of molar ratio of Mo in the precursors, which resulted from the non-optimum layer thickness by increasing of the series resistance of these HTLs [32]. The sMoO$_x$_B-based device exhibited the highest FF and PCE of 72.5 % and 7.19 %, respectively.

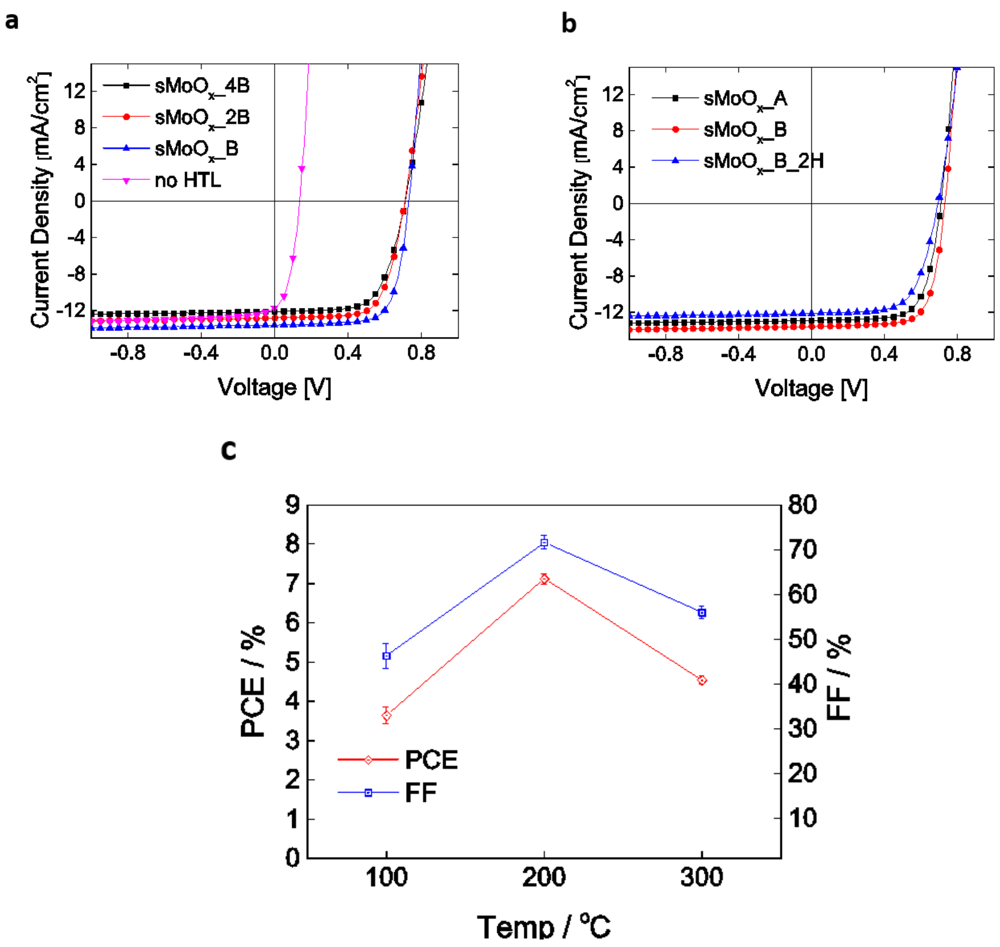

Figure 4.8 (a) J-V curves of OSCs with sMoO$_x$ HTLs fabricated using precursors with different Mo molar ratios. (b) J-V curves of OSCs with sMoO$_x$ HTLs fabricated with different H_2O_2 vol.%. (c) PCEs and fill factors of OSCs annealed at different temperatures.

Table 4.1 Photovoltaic parameters of PV_{10}:$PC_{70}BM$ devices with different HTLs

HTLs	J_{sc} (mA/cm^2)	V_{oc} (V)	FF (%)	PCE (%)	R_s (Ω/cm^2)
No HTL	11.73	0.14	41.08	0.67	4.1
$sMoO_x$_A	12.92	0.71	69.81	6.41	4.5
$sMoO_x$_B	13.57	0.73	72.55	7.19	3.9
$sMoO_x$_2B	12.82	0.71	67.77	6.16	8.0
$sMoO_x$_4B	12.12	0.71	65.39	5.62	9.9
$sMoO_x$_B_2H	12.12	0.69	65.67	5.49	10.3
$eMoO_x$	12.51	0.73	70.93	6.48	5.5
PEDOT:PSS	12.61	0.82	68.26	7.05	5.3

To further investigate the influence of H_2O_2 on the performance of OSCs with $sMoO_x$-based HTLs, the volume percentage of H_2O_2 in the precursor solution was adjusted to 10 and 20 vol.% to fabricate HTLs, which were defined as $sMoO_x$_B and $sMoO_x$_B_2H, respectively. The J–V characteristics of OSCs with these HTLs are shown in Figure 4.8b. The device with $sMoO_x$_B_2H possessed both the lower J_{sc} and V_{oc} of 0.69 mA/cm^2 and 12.12 V, respectively, and corresponding low FF of 65.67 % and PCE of 5.49 %. The poor performance of the $sMoO_x$_B_2H-based solar cell indicated 20 vol.% was too much H_2O_2 in the precursor solution.

The annealing temperature of the $sMoO_x$_B-based HTL was also investigated to optimize the performance of the corresponding OSCs. OSCs containing $sMoO_x$_B HTLs annealed at temperatures of 100, 200, and 300 °C were fabricated; the FF and PCE of these solar cells are presented in Figure 4.8c. The HTL annealed at 200 °C showed the optimum fill factor and PCE. The poorer performance of the devices annealed at 100 and 300 °C can be attributed to the remaining organic components in the case of the lower annealing temperature of 100 °C, and higher surface roughness and discontinuity of the HTL annealed at the higher temperature of 300 °C, as shown in Figure 4.9.

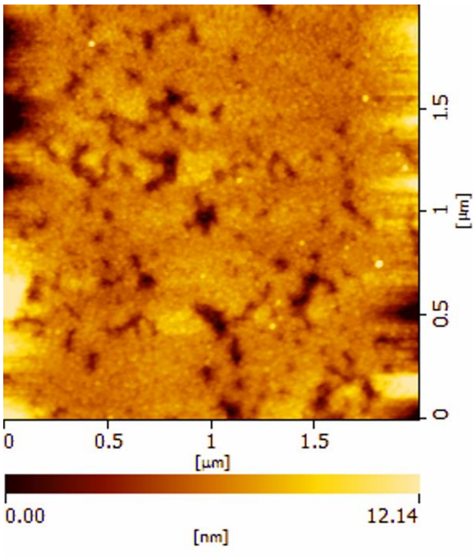

Ra = 1.07 nm
RMS = 1.66 nm

Figure 4.9 AFM image of a solution-processed MoO$_x$_B film on a Si substrate following annealing at 300 °C for 10 min.

4.4 Conclusion

Solution-processed MoO_x-based HTLs for OSCs were fabricated by dissolving $(NH_4)_2MoO_4$ and citric acid in H_2O_2-modified 2-methoxyethanol. The resulting HTLs showed a smoother surface (RMS roughness of 0.24 nm), higher transparency (> 90 %), and lower resistivity (3.9 Ω/cm^2) than those of ones fabricated without H_2O_2. The performance of an OSC containing the HTL produced from the H_2O_2-modified precursor was higher than that of the device produced without H_2O_2, and comparable to those of cells with a PEDOT:PSS or $eMoO_x$ HTL. The enhancement of device performance was attributed to the increased polyvalence of Mo in the oxide thin films attained by introducing 10 vol.% H_2O_2 into the precursors, which resulted in increased hole transport ability. The influence of the molar ratio of the Mo source and annealing temperature on the performance of OSCs based on the solution-processed HTLs were also investigated; optimized values were 0.075 mol/L and 200 °C, respectively. These results reveal that MoO_x HTLs fabricated by the developed route are promising to replace conventional $eMoO_x$ HTLs, and contributed to the mass production of OSCs by virtue of their simple fabrication and low cost.

Reference

[1] Kim T, Kim J-H, Kang TE, Lee C, Kang H, Shin M, Wang C, Ma B, Jeong U, Kim T-S. Flexible, highly efficient all-polymer solar cells. Nature communications 2015;6.

[2] Guo X, Zhou N, Lou SJ, Smith J, Tice DB, Hennek JW, Ortiz RP, Navarrete JTL, Li S, Strzalka J. Polymer solar cells with enhanced fill factors. Nature Photonics 2013;7:825.

[3] Li G, Zhu R, Yang Y. Polymer solar cells. Nature Photonics 2012;6:153.

[4] Brezesinski T, Wang J, Tolbert SH, Dunn B. Ordered mesoporous [alpha]-MoO_3 with iso-oriented nanocrystalline walls for thin-film pseudocapacitors. Nat. Mater. 2010;9:146.

[5] Zhou J, Deng S, Xu N, Chen J, She J. Synthesis and field-emission properties of aligned MoO_3 nanowires. Appl. Phys. Lett. 2003;83:2653.

[6] Meduri P, Clark E, Kim JH, Dayalan E, Sumanasekera GU, Sunkara MK. MoO_{3-x} nanowire arrays as stable and high-capacity anodes for lithium ion batteries. Nano Lett. 2012;12:1784.

[7] Dinh NN, Chung DN, Thao TT, Thuy TTC, Chi LH, Truong V-V. Enhancement of performance of organic light emitting diodes by using Ti-and Mo-oxide nano hybrid layers. Materials Sciences and Applications 2013;4:275.

[8] Scanlon DO, Watson GW, Payne D, Atkinson G, Egdell R, Law D. Theoretical and experimental study of the electronic structures of MoO_3 and MoO_2. The Journal of Physical Chemistry C 2010;114:4636.

[9] Greiner MT, Chai L, Helander MG, Tang WM, Lu ZH. Metal/metal-oxide interfaces: how metal contacts affect the work function and band structure of MoO_3. Adv. Funct. Mater. 2013;23:215.

[10] Li X, Xie F, Zhang S, Hou J, Choy WC. MoO_x and V_2O_x as hole and electron transport layers through functionalized intercalation in normal and inverted organic optoelectronic devices. Light: Science & Applications 2015;4:273.

[11] Liu J, Shao S, Fang G, Meng B, Xie Z, Wang L. High-efficiency inverted polymer solar cells with transparent and work‐function tunable MoO_3‐Al composite film as cathode buffer layer. Advanced Materials 2012;24:2774.

[12] Chen H-Y, Su H-C, Chen C-H, Liu K-L, Tsai C-M, Yen S-J, Yew T-R. Indium-doped molybdenum oxide as a new p-type transparent conductive oxide. J. Mater. Chem. 2011;21:5745.

[13] You J, Dou L, Yoshimura K, Kato T, Ohya K, Moriarty T, Emery K, Chen C-C, Gao J, Li G. A polymer tandem solar cell with 10.6% power conversion efficiency. Nature communications 2013;4:1446.

[14] Chen LM, Hong Z, Li G, Yang Y. Recent progress in polymer solar cells: manipulation of polymer: fullerene morphology and the formation of efficient inverted polymer solar cells. Advanced Materials 2009;21:1434.

[15] Hadipour A, de Boer B, Wildeman J, Kooistra FB, Hummelen JC, Turbiez MG, Wienk MM, Janssen RA, Blom PW. Solution-processed organic tandem solar cells. Adv. Funct. Mater. 2006;16:1897.

[16] Hadipour A, Cheyns D, Heremans P, Rand BP. Electrode considerations for the optical enhancement of organic bulk heterojunction solar cells. Adv. Energy Mater. 2011;1:930.

[17] Shrotriya V. Organic photovoltaics: Polymer power. Nature Photonics 2009;3:447.

[18] Jasieniak JJ, Seifter J, Jo J, Mates T, Heeger AJ. A solution-processed MoO_x anode interlayer for use within organic photovoltaic devices. Adv. Funct. Mater. 2012;22:2594.

[19] Lattante S. Electron and hole transport layers: their use in inverted bulk heterojunction polymer solar cells. Electronics 2014;3:132.

[20] Nirupama V, Chandrasekhar M, Radhika P, Sreedhar B, Uthanna S. Characterization of molybdenum oxide films prepared by bias magnetron sputtering. Journal of optoelectronics and advanced materials 2009;11:320.

[21] Fan X, Fang G, Qin P, Sun N, Liu N, Zheng Q, Cheng F, Yuan L, Zhao X. Deposition temperature effect of RF magnetron sputtered molybdenum oxide films on

the power conversion efficiency of bulk-heterojunction solar cells. Journal of Physics D: Applied Physics 2011;44:045101.

[22] Larsen JK, Simchi H, Xin P, Kim K, Shafarman W. Backwall superstrate configuration for ultrathin Cu(In,Ga)Se_2 solar cells. Appl. Phys. Lett. 2014;104:033901.

[23] Simchi H, McCandless BE, Meng T, Shafarman WN. Structure and interface chemistry of MoO_3 back contacts in Cu (In,Ga)Se_2 thin film solar cells. J. Appl. Phys. 2014;115:033514.

[24] Shrotriya V, Li G, Yao Y, Chu C-W, Yang Y. Transition metal oxides as the buffer layer for polymer photovoltaic cells. Appl. Phys. Lett. 2006;88:073508.

[25] Sun Y, Takacs CJ, Cowan SR, Seo JH, Gong X, Roy A, Heeger AJ. Efficient, air-stable bulk heterojunction polymer solar cells using MoO_x as the anode interfacial layer. Advanced materials 2011;23:2226.

[26] Meyer J, Shu A, Kro¨ ger M, Kahn A. Effect of contamination on the electronic structure and hole-injection properties of MoO_3/organic semiconductor interfaces. Appl. Phys. Lett. 2010;96:133308.

[27] Greiner MT, Lu Z-H. Thin-film metal oxides in organic semiconductor devices: their electronic structures, work functions and interfaces. NPG Asia Materials 2013;5:e55.

[28] Qiu W, Müller R, Voroshazi E, Conings B, Carleer R, Boyen H-G, Turbiez M, Froyen L, Heremans P, Hadipour A. Nafion-modified MoO_x as effective room-temperature hole injection layer for stable, high-performance inverted organic solar cells. ACS applied materials & interfaces 2015;7:3581.

[29] Zilberberg K, Gharbi H, Behrendt A, Trost S, Riedl T. Low-temperature, solution-processed MoO_x for efficient and stable organic solar cells. ACS applied materials & interfaces 2012;4:1164.

[30] Litzov I, Brabec CJ. Development of efficient and stable inverted bulk heterojunction (BHJ) solar cells using different metal oxide interfaces. Materials 2013;6:5796.

[31] Girotto C, Voroshazi E, Cheyns D, Heremans P, Rand BP. Solution-processed MoO_3 thin films as a hole-injection layer for organic solar cells. ACS applied materials & interfaces 2011;3:3244.

[32] Murase S, Yang Y. Solution processed MoO_3 interfacial layer for organic photovoltaics prepared by a facile synthesis method. Advanced Materials 2012;24:2459.

[33] Wang Y, Luo Q, Wu N, Wang Q, Zhu H, Chen L, Li Y-Q, Luo L, Ma C-Q. Solution-processed MoO_3: PEDOT: PSS hybrid hole transporting layer for inverted polymer solar cells. ACS applied materials & interfaces 2015;7:7170.

[34] Li X, Choy WC, Xie F, Zhang S, Hou J. Room-temperature solution-processed molybdenum oxide as a hole transport layer with Ag nanoparticles for highly efficient inverted organic solar cells. J. Mater. Chem. A 2013;1:6614.

[35] Choy WC, Zhang D. Solution-processed metal oxides as efficient carrier transport layers for organic photovoltaics. Small 2016;12:416.

[36] Qiu W, Hadipour A, Müller R, Conings B, Boyen H-G, Heremans P, Froyen L. Ultrathin ammonium heptamolybdate films as efficient room-temperature hole transport layers for organic solar cells. ACS applied materials & interfaces 2014;6:16335.

[37] Cong S, Sugahara T, Wei T, Jiu J, Hirose Y, Nagao S, Suganuma K. Diverse adsorption/desorption abilities originating from the nanostructural morphology of voc gas sensing devices based on molybdenum trioxide nanorod arrays. Advanced Materials Interfaces 2016;3:1600252.

[38] Sugahara T, Hirose Y, Cong S, Koga H, Jiu J, Nogi M, Nagao S, Suganuma K. sol-gel-derived high-performance stacked transparent conductive oxide thin films. Journal of the American Ceramic Society 2014;97:3238.

[39] Ranjbar S, Brammertz G, Vermang B, Hadipour A, Cong S, Suganuma K, Schnabel T, Meuris M, da Cunha A, Poortmans J. Improvement of kesterite solar cell performance by solution synthesized MoO_3 interfacial layer. physica status solidi (a) 2016 DOI: 10.1002/pssa.201600534, in press.

[40] Cong S, Sugahara T, Wei T, Jiu J, Hirose Y, Nagao S, Suganuma K. Growth and extension of one-step sol–gel derived molybdenum trioxide nanorods via controlling citric acid decomposition rate. Cryst. Growth Des. 2015;15:4536.

[41] Zazoui M, Bourgoin J, Stievenard D, Deresmes D, Strobl G. Recombination centers in electron-irradiated Czochralski silicon solar cells. J. Appl. Phys. 1994;76:815.

[42] Street R, Northrup J, Krusor B. Radiation induced recombination centers in organic solar cells. Physical Review B 2012;85:205211.

[43] Schmit J. Intrinsic Carrier Concentration of $Hg_{1-x}Cd_xTe$ as a function of x and T using k· p calculations. J. Appl. Phys. 1970;41:2876.

Chapter 5

Conclusion and prospect

As one of the most promising candidates for next generation electronic material, molybdenum oxide, are attracting more and more attentions from researchers because of its special crystal and electronic structure. α-MoO_3 can be designed as low-dimension nanocrystal with large specific surface area for gas sensors. Moreover, the MoO_x can be tuned as high work function and high conductivity for fabricating the hole transport layer (HTL) in the organic solar cells. We try to use the simple solution process to control the nanomorphology and electronic structure of the molybdenum oxide to fabricate the electronic devices.

The general introduction of this research is presented in chapter one, including the fundamental characteristics of MoO_3, synthesis method for the nanostructure of MoO_3, gas sensor properties of MoO_3 and hole transport layer in the organic solar cells. Finally, the author defined the main objective of this thesis.

In the chapter two, a simple sol-gel method was developed for synthesizing ultra-fine (about 10 nm) α-MoO_3 nanorod arrays. The experiments indicate that the morphology of the obtained samples depends on the molar ratio of molybdate:citric acid, solvents, and annealing time. The optimal growth conditions for long nanorods are as follows: molar ratio of molybdate:citric acid = 0.5:1.5, DMAC as a solvent, and annealing at 400 ^{o}C for 15 min. The mean length of the obtained α-MoO_3 nanorods was about 500 nm, and the maximum nanorods lengths can be extended up to approximately 600 nm.

In chapter three, we developed a prototype alcoholic gas analysis device made from α-MoO_3 nanorod arrays. The 3D nanorod arrays showed excellent sensitivity and discrimination of the various vapors at 300 ^{o}C, with considerable dependence on the structure of the 3D network nanorod arrays. The sensor with more numerous and longer nanorods showed a larger and quicker response to the VOC vapors than that of the sensors with fewer and shorter nanorods.

In chapter four, solution-processed MoO_x-based HTLs for OSCs were fabricated by dissolving $(NH_4)_2MoO_4$ and citric acid in H_2O_2-modified 2-methoxyethanol. The resulting HTLs showed a smoother surface (RMS roughness of 0.24 nm), higher transparency (>90%), and lower resistivity (3.9 Ω/cm^2) than those of ones fabricated without H_2O_2. The enhancement of device performance was attributed to the increased polyvalence of Mo in the oxide thin films attained by introducing 10 vol.% H_2O_2 into the precursors, which resulted in increased hole transport ability. The influence of the molar ratio of the Mo source and annealing temperature on the performance of OSCs based on the solution-processed HTLs were also investigated; optimized values were 0.075 mol/L and 200 °C, respectively.

In the present study, the main focus of the discussion is synthesizing the Mo base oxide nanorods and corresponding electronic device (gas sensor and organic solar sell). The key for the research is using a simple and effective solution process to synthesize the nanorods arrays, gas sensor and hole transport layer. The knowledge garnered from this study will greatly facilitate the research and development of gas analyzer or organic electronic devices with universal applications with a relatively simple, inexpensive, and scalable processing methods.

Further research in this regime is expected to give an explicit answer for the controversy of the conductive mechanism of MoO_3/MoO_x-based nanorods/film in electrical devices. One way is to research the conduction type of MoO_3/MoO_x-based nanorods/film in electrical devices. However, the high resistance of MoO_3/MoO_x-based nanorods/film make it very difficult to determine the conduction type. To develop an effective method to confirm the conduction type of MoO_3/MoO_x-based nanorods/film can be an intending research interests in the future. A systematic effort is expected to continue to clarify the nature of MoO_3/MoO_x-based system and broaden the practical application in electrical devices.

List of publications

[A] Papers

[A-1] "Growth and Extension of One–Step Sol–Gel Derived Molybdenum Trioxide Nanorods via Controlling Citric Acid Decomposition Rate"

Shuren Cong, Tohru Sugahara, Tingting Wei, Jinting Jiu, Yukiko Hirose, Shijo Nagao, and Katsuaki Suganuma

Cryst. Growth Des. **15** (2015) 4536-4542 (**XRD pattern in this paper were recorded into ICDD data base as No. I06003**)

[A-2] "Diverse Adsorption/Desorption Abilities Originating from the Nanostructural Morphology of VOC Gas Sensing Devices Based on Molybdenum Trioxide Nanorod Arrays"

Shuren Cong, Tohru Sugahara, Tingting Wei, Jinting Jiu, Yukiko Hirose, Shijo Nagao, and Katsuaki Suganuma

Adv. Mater. Interfaces, **3** (2016) 1600252 (8 pages). **(Inside cover paper)**

[A-3] "Modifying Valence State of Molybdenum in the Efficient Oxide Buffer Layer for Organic Solar Cell through a Mild Hydrogen Peroxide-Treatment Solution Route"

Shuren Cong, Afshin Hadipour, Tohru Sugahara, Tingting Wei, Jinting Jiu, Samaneh Ranjbar, Yukiko Hirose, Karakawa Makoto, Shijo Nagao, Tom Aernouts, and Katsuaki Suganuma, J. Mater. Chem. C, (2016) DOI: 10.1039/C6TC04461A, *In press*.

[A-4] "Sol–Gel-Derived High-Performance Stacked Transparent Conductive Oxide Thin Films"

Tohru Sugahara, Yukiko Hirose, **Shuren Cong**, Hirotaka Koga, Jinting Jiu, Masaya Nogi, Shijo Nagao, Katsuaki Suganuma, J. Am. Ceram. Soc., **97** (2014), 3238–3243.

[A-5] "Self-Reducible Copper Ink Composed of Copper-Amino Complexes and Preset Submicron Copper Seeds for Thick Conductive Patterns on a Flexible Substrate"

Wanli Li, **Shuren Cong**, Jinting Jiu, Shijo Nagao and Katsuaki Suganuma, J. Mater. Chem. C, **4** (2016), 8802–8809.

[A-6] “Improvement of Kesterite Solar Cell Performance by Solution Synthesized MoO_3 Interfacial Layer”

Samaneh Ranjbar, Guy Brammertz, Bart Vermang, Afshin Hadipour, **Shuren Cong**, Katsuaki Suganuma, Thomas Schnabel, Marc Meuris, A. F. da Cunha, and Jef Poortmans, Phys. Status Solidi A, (2016) DOI: 10.1002/pssa.201600534, *In press.*

[B] Proceeding and presentations

[B-1] “Enhancement of reaction area of molybdenum trioxide nanorods via sol-gel drived method and its gas sensing property”

Shuren Cong, Tohru Sugahara, Jinting Jiu, Yukiko Hirose, Shijo Nagao, and Katsuaki Suganuma

2015 EMN Qingdao Meeting, Qingdao, China 2015/6/14-17 (Oral)

[B-2] “Improved Gas Sensing Properties to VOC Vapour via Controlled Reaction Area of α-MoO_3 Nanorods with One Step Sol-Gel Route”

Shuren Cong, Tohru Sugahara, Jinting Jiu, Yukiko Hirose, Shijo Nagao, and Katsuaki Suganuma

2015 MRS Fall Meeting & Exhibit, Boston, USA 2015/11/29-12/4 (Poster)

[B-3] “Enhancement of Efficiency of the Organic Solar Cell by Applying a Simple Solution-Processed MoO_x Buffer Layer”

Shuren Cong, Afshin Hadipour, Tohru Sugahara, Jinting Jiu, Yukiko Hirose, Karakawa Makoto, Shijo Nagao, Katsuaki Suganuma, and Tom Aernouts

E-MRS 2016 Spring Meeting, Lille, France 2016/5/2-6 (Poster)

[B-4] “Improvement of CZTs Solar Cell Performance by Industrially Viable MoO_3/Mo Rear Contact”

Samaneh Ranjbar, Guy Brammertz, Bart Vermang, Afshin Hadipour, **Shuren Cong**, Marc Meuris, A. F. da Cunha, and Jef Poortmans.

EU PCSEC 2016 Conference, 32nd European PV Solar Energy Conference and Exhibition, Munich, Germany 2016/6/20-24 (Poster)

[B-5] “Improvement of V_{oc} in kesterite solar cells by introducing appropriate metal oxide layers at rear interface and p-n junction”

Samaneh Ranjbar, Guy Brammertz, Bart Vermang, Afshin Hadipour, **Shuren Cong**, Katsuaki Suganuma, Thomas Schnabel, Maria Batuk, Joke Hadermann, Siddhartha Garud , Marc Meuris, A. F. da Cunha, and Jef Poortmans

The 7th European Kesterite Workshop, Leuven, Belgium 2016/11/17-18 (Poster)

[B-6] “Growth and characterization of molybdenum oxide nanorods by one-step sol-gel spin coating method”

Shuren Cong, Tohru Sugahara, Jinting Jiu, Yukiko Hirose, Shijo Nagao, katsuaki Suganuma

The 75th JSAP Autumn Meeting, Hokkaido University, Japan 2014/9/17-20 (Oral)

[B-7] “Synthesis of molybdenum trioxide nanorods arrays via one-step sol-gel spin coating method”

Shuren Cong, Tohru Sugahara, Jinting Jiu, Yukiko Hirose, Shijo Nagao, katsuaki Suganuma

The 29th Fall Meeting of The Ceramic Society of Japan, Okayama University, Japan 2015/3/18-20 (Oral)

[B-8] “ゾル・ゲル法によるMoO_3ナノロッドガスセンサ素子の創成”

Tohru Sugahara, **Shuren Cong**, katsuaki Suganuma

The 63th JSAP spring Meeting, Tokyo Institute of Technology, Japan 2016/3/19-22 (Oral)

[C] News

[C-1] “呼気センサの製造時間を大幅に短縮,呼気から健康診断や重大疾患の早期発見に期待” (ISIR, Osaka Univ.)

http://resou.osaka-u.ac.jp/ja/research/2016/20160715_2

http://www.sanken.osaka-u.ac.jp/c_top_hot_topics/topics_20160706/

Acknowledgements

The author would like to express my appreciation to those who contributed to this dissertation.

Firstly, I would like to express my sincerely gratitude to Prof. Katsuaki Suganuma at the Institute of Scientific and Industrial Research (ISIR), Osaka University for his steady advices, encouragement, support, and stimulating discussions. His passion and insight towards research has been of great value for my future as a researcher. I am deeply grateful to him for providing me the opportunity to learn here.

I would like to thank Prof. Tohru Sekino at ISIR and Assoc. Prof. Shijo Nagao at ISIR, for being my committee members and for their invaluable advices and encouraging comments during preparation on this thesis.

I am deeply grateful to thank Dr. Tohru Sugahara for his great advices, kind stimulus and vital discussions on the scientific issues. From him I mastered the mode of scientific thinking.

I would like to thank Prof. Tetsuro Muramatsu, Assoc. Prof. Masaya Nogi and Dr. Hirotaka Koga for their insightful comments. I would like to thank Dr. Jinting Jiu for her intelligent advices and kind supports not only in study but also in my daily life. I also would like to thank Dr. Hao Zhang, Dr. Caifu Li, Dr. Chuantong Chen, Wanli Li, Zhenghong Wang for their valuable comments.

Special thanks to Dr. Afshin Hadipour at Interuniversity Microelectronics Center (IMEC), who trained me to fabricate my first organic solar cell device. His enthusiasm and cautious attitude in research affect me deeply.

I warmly thank my colleagues Shunsuke Koga, Hao Zhang, Yue Gao, Yusuke Goya, Yoshikawa, Linying Li, Dawei Hu, Chun Pei, Taikun Fan for friendly help. I would like to thank TsukasaTakahashi, Kagami, Yoshiko Harada, Izumi, Keiko Suzuki, Midori Fuji, Satomi Yamawaki, and Asana Yoshiya for kind support.

Finally, I would like to express my gratitude to my family. I am a father with two children. They give me infinite happiness and courage for keeping on striving. When I see them I will forget all the agonies. Last but the most important, I deeply thank my wife. It is her that gives me two bright children. She is not only a good wife but also a best friend of me. She always give me the right suggestions either in daily life or in the research. This dissertation is dedicated to my family!